Gui-Juan Cheng

Mechanistic Studies on Transition Metal-Catalyzed C−H Activation Reactions Using Combined Mass Spectrometry and Theoretical Methods

Springer

Springer Theses

Recognizing Outstanding Ph.D. Research

Aims and Scope

The series "Springer Theses" brings together a selection of the very best Ph.D. theses from around the world and across the physical sciences. Nominated and endorsed by two recognized specialists, each published volume has been selected for its scientific excellence and the high impact of its contents for the pertinent field of research. For greater accessibility to non-specialists, the published versions include an extended introduction, as well as a foreword by the student's supervisor explaining the special relevance of the work for the field. As a whole, the series will provide a valuable resource both for newcomers to the research fields described, and for other scientists seeking detailed background information on special questions. Finally, it provides an accredited documentation of the valuable contributions made by today's younger generation of scientists.

Theses are accepted into the series by invited nomination only and must fulfill all of the following criteria

- They must be written in good English.
- The topic should fall within the confines of Chemistry, Physics, Earth Sciences, Engineering and related interdisciplinary fields such as Materials, Nanoscience, Chemical Engineering, Complex Systems and Biophysics.
- The work reported in the thesis must represent a significant scientific advance.
- If the thesis includes previously published material, permission to reproduce this must be gained from the respective copyright holder.
- They must have been examined and passed during the 12 months prior to nomination.
- Each thesis should include a foreword by the supervisor outlining the significance of its content.
- The theses should have a clearly defined structure including an introduction accessible to scientists not expert in that particular field.

Gui-Juan Cheng

Mechanistic Studies on Transition Metal-Catalyzed C–H Activation Reactions Using Combined Mass Spectrometry and Theoretical Methods

Author
Dr. Gui-Juan Cheng
Laboratory of Computational Chemistry
  and Drug Design and Laboratory
  of Chemical Genomics
Peking University Shenzhen Graduate
  School
Shenzhen
China

Supervisors
Prof. Yun-Dong Wu
Laboratory of Computational Chemistry
  and Drug Design and Laboratory
  of Chemical Genomics
Peking University Shenzhen Graduate
  School
Shenzhen
China

and

College of Chemistry and Molecular
  Engineering
Peking University
Beijing
China

Prof. Xinhao Zhang
Laboratory of Computational Chemistry
  and Drug Design and Laboratory
  of Chemical Genomics
Peking University Shenzhen Graduate
  School
Shenzhen
China

Supervisor's Foreword

With the incredible development of theoretical methods and computer hardware, computational chemistry has become a practical and essential tool in understanding reaction mechanism. When facing realistic questions raised from flask, communication between theory and experiment is critical. Applications of computational chemistry are also facilitated by aids of various experimental techniques providing mechanistic insights. In this thesis, Dr. Gui-Juan Cheng investigated reaction mechanism with computational chemistry and mass spectrometry. In particular, a novel approach combining ion-mobility mass spectrometry and theoretical calculations was introduced as an addition to the toolbox for mechanistic study.

This dissertation focuses on the topic of C–H activation. Selective functionalization of ubiquitous C–H bonds provides an efficient synthetic strategy and experienced a remarkable development in recent years. Dr. Gui-Juan Cheng conducted detailed and systematic studies on a series of prominent C–H activation reactions which are recognized as breakthroughs in this field. The critical issues including the active form of catalyst, the role of ligand and additives, the origins of regio- and enantio-selectivity were investigated.

Several new mechanisms have been established in this dissertation. Chapter 2 proposes an unprecedented dimeric $Pd_2(OAc)_4$ or $PdAg(OAc)_3$ as the possible active catalyst for C–H activation. It successfully accounts for the experimentally observed *meta*-selectivity, and expands our understanding of the active form of palladium catalyst. Chapters 3 and 4 reveal the role of mono-N-protected amino acid (MPAA) ligands in Pd-catalyzed C–H bond functionalization and uncover a novel C–H activation model which accounts for the improved reactivity and selectivity. Further work obtains experimental supports for the novel C–H activation mechanism and proposes a chirality-relay model which successfully predicts the enantioselectivities of a range of asymmetric C–H activation reactions. Chapter 5

involves a sp^3 C–H cross-dehydrogenative coupling reaction and provides details of mechanistic profiles. Overall, the studies of this dissertation provide deeper mechanistic understandings as well as novel C–H activation models and offers guidance for optimizing or designing ligands and reactions.

Shenzhen, China   Prof. Yun-Dong Wu
March 2017

Parts of this thesis have been published in the following journal articles:

1. Yang, Y.-F.[⊥]; **Cheng, G.-J.**[⊥]; Liu, P.; Leow, D.; Sun, T.-Y.; Chen, P.; Zhang, X.; Yu, J.-Q.; Wu, Y.-D.; Houk, K. N. Palladium-Catalyzed Meta-Selective C–H Bond Activation with a Nitrile-Containing Template: Computational Study on Mechanism and Origins of Selectivity. *J. Am. Chem. Soc.* **2014**, *136*, 344. ([⊥]: co-first author)

2. **Cheng, G.-J.**; Yang, Y.-F.; Liu, P.; Chen, P.; Sun, T.-Y.; Li, G.; Zhang, X.; Houk, K. N.; Yu, J.-Q.; Wu, Y.-D. Role of N-Acyl Amino Acid Ligands in Pd (II)-Catalyzed Remote C–H Activation of Tethered Arenes. *J. Am. Chem. Soc.* **2014**, *136*, 894.

3. **Cheng, G.-J.**; P.; Chen, P.; Sun, T.-Y.; Zhang, X.; Yu, J.-Q.; Wu, Y.-D. A Combined IM-MS/DFT Study on Pd(MPAA)-Catalyzed Enantioselective C−H Activation: Relay of Chirality through a Rigid Framework. *Chem. Eur. J.* **2015**, *21*, 11180.

4. **Cheng, G.-J.**; Song, L.-J.; Yang, Y.-F.; Zhang, X.; Wiest, O.; Wu, Y.-D. Computational Studies on the Mechanism of the Copper-Catalyzed sp^3-C–H Cross-Dehydrogenative Coupling Reaction. *ChemPlusChem* **2013**, *78*, 943.

List of Publications

1. Rummelt, S.; **Cheng, G.-J.**; Gupta, P.; Thiel, W.; Fürstner, A. Hydroxyl-Directed Ruthenium Catalyzed Alkene/Alkyne Coupling: Increased Scope, Stereochemical Implications and Mechanistic Rationale. *Angew. Chem. Int. Ed.* **2017**, *56*, 3599.

2. Xie, Y.; **Cheng, G.-J.**; Lee, S.; Kaib, P.; Thiel, W.; List, B. Catalytic Asymmetric Vinylogous Prins Cyclization: A Highly Diastereo- and Enantioselective Entry to Tetrahydrofurans. *J. Am. Chem. Soc.* **2016**, *138*, 14538.

3. Zhong, X.-M. ⊥; **Cheng, G.-J.** ⊥; P.; Chen, P.; Zhang, X.; Yu, Wu, Y.-D. Mechanistic Study on Pd/Mono-N-protected Amino Acid Catalyzed Vinyl–Vinyl Coupling Reactions: Reactivity and E/Z Selectivity. *Org. Lett.* **2016**, *18*, 5240. (⊥:co-first author)

4. **Cheng, G.-J.**; P.; Chen, P.; Sun, T.-Y.; Zhang, X.; Yu, J.-Q.; Wu, Y.-D. A Combined IM-MS/DFT Study on Pd(MPAA)-Catalyzed Enantioselective C−H Activation: Relay of Chirality through a Rigid Framework. *Chem. Eur. J.* **2015**, *21*, 11180.

5. **Cheng, G.-J.**; Zhang, X.; Chung, L. W.; Xu, L.; Wu, Y.-D. Computational Organic Chemistry: Bridging Theory and Experiment by Mechanistic Understanding of Chemical Reactions. *J. Am. Chem. Soc.* **2015**, *137*, 1706.

6. Zhou, F. ⊥; **Cheng, G.-J.** ⊥; Yang, W. ⊥; Long, Y.; Zhang, S.; Wu, Y.-D.; Zhang, X.; Cai, Q. Enantioselective Formation of Cyano-Bearing All-Carbon Quaternary Stereocenters: Desymmetrization by Copper-Catalyzed N-Arylation. *Angew. Chem. Int. Ed.* **2014**, *53*, 9555. (⊥: co-first author)

7. **Cheng, G.-J.**; Yang, Y.-F.; Liu, P.; Chen, P.; Sun, T.-Y.; Li, G.; Zhang, X.; Houk, K. N.; Yu, J.-Q.; Wu, Y.-D. Role of N-Acyl Amino Acid Ligands in Pd (II)-Catalyzed Remote C–H Activation of Tethered Arenes. *J. Am. Chem. Soc.* **2014**, *136*, 894.

8. Yang, Y.-F.[⊥]; **Cheng, G.-J.**[⊥]; Liu, P.; Leow, D.; Sun, T.-Y.; Chen, P.; Zhang, X.; Yu, J.-Q.; Wu, Y.-D.; Houk, K. N. Palladium-Catalyzed Meta-Selective C–H Bond Activation with a Nitrile-Containing Template: Computational Study on Mechanism and Origins of Selectivity. *J. Am. Chem. Soc.* **2014**, *136*, 344. ([⊥]: co-first author)

9. **Cheng, G.-J**.; Song, L.-J.; Yang, Y.-F.; Zhang, X.; Wiest, O.; Wu, Y.-D. Computational Studies on the Mechanism of the Copper-Catalyzed sp^3-C–H Cross-Dehydrogenative Coupling Reaction. *ChemPlusChem* **2013**, *78*, 943.

10. Zhu, L.; Zhou, C.; Yang, W.; He, S.; **Cheng, G.-J.**; Zhang, X.; Lee, C.-S. Formal Syntheses of (±)-Platensimycin and (±)-Platencin via a Dual-Mode Lewis Acid Induced Cascade Cyclization Approach. *J. Org. Chem.* **2013**, *78*, 7912.

11. Zhao, K.; **Cheng, G.-J.**; Yang, H.; Shang, H.; Zhang, X.; Wu, Y.-D.; Tang, Y. Total Synthesis of Incarvilleatone and Incarviditone: Insight into Their Biosynthetic Pathways and Structure Determination. *Org. Lett.* **2012**, *14*, 4878.

12. Yang, Y.-F.; **Cheng, G.-J**.; Zhu, J.; Zhang, X.; Inoue, S.; Wu, Y.-D. Silicon-Containing Formal 4pi-Electron Four-Membered Ring Systems: Antiaromatic, Aromatic, or Not? *Chem. Eur. J.* **2012**, 18, 7516.

Acknowledgements

The work in this dissertation were conducted under the supervisions of Prof. Yun-Dong Wu and Prof. Xinhao Zhang at Peking University Shenzhen Graduate School from September 2010 to July 2015. I would like to express my great gratitude to all the people who have supported me and made this thesis possible.

First of all, I would like to express my most sincere gratitude to my supervisor, Prof. Yun-Dong Wu, for his guidance, encouragement and supports. I have been extremely lucky to have such a wonderful supervisor. His immense knowledge and insightful views in chemistry, as well as rigorous academic attitude affected me deeply. Prof. Wu often shares scientific research methodology, logical thinking and critical thinking with us which benefit me a lot. His life philosophy about keeping balance between life and work provides valuable instructions for my future life.

Furthermore, I am very grateful to Prof. Xinhao Zhang for introducing me to the exciting research field and for his numerous help and advice on both research and life. He always reminded me to enjoy science and enjoy the "treasure hunt" process of scientific research which gave me great encouragement when I feel depressed about research.

Moreover, I would like to thank Prof. Olaf Wiest for providing helpful suggestions and instructions on scientific writing and publishing. I am further thankful to Prof. Lungwa, Chuang, Prof. Zhiqiang, Ye and Dr. Fan Jiang for their help. Thanks also go to all my collaborators: Prof. Jin-Quan Yu, Prof. K.N. Houk, Prof. Yefeng Tang, Prof. Qian Cai and others who are not mentioned by name.

I am very thankful to Dr. Yun-Fang Yang, Dr. Li-Juan Song, Pin Chen and Tian-Yu Sun who made contributions to the work presented in this thesis. Thanks also to Ms. Chao Deng who makes our life easier and more comfortable. In addition, I would like to thank all former and current group members in the big "family". All the joyful days we spent together and all the fun moments we shared made my Ph.D. life more colorful and memorable.

Finally, I would like to express my utmost gratitude to my parents, my sisters and my husband for their endless love, care, support, and understanding. I am incredibly fortunate to have such a loving family.

This book is dedicated to my family and Prof. Yun-Dong Wu on the occasion of his 60th birthday.

Contents

Abbreviations

Ar	Any aromatic group
CCS	Collision cross section
CDC	Cross-dehydrogenative coupling
CID	Collision induced dissociation
CMD	Concerted metallation and deprotonation
DFT	Density Functional Theory
DG	Directing group
e.e.	Enantiomeric excess
EHSS	Exact hard sphere scattering
ESI	Electrospray ionization
IM-MS	Ion mobility mass spectrometry
MECP	Minimum energy crossing point
MPAA	Mono-N-protected amino acid
MS	Mass spectrometry
PA	Projection approximation
PES	Potential Energy Surface
SET	Single electron transfer
TM	Trajectory method
TS	Transition state
TWIMS	Traveling wave ion mobility spectrometry
S_EAr	Electrophilic aromatic substitution
*t*Bu	*Tert*-butyl
*i*Pr	Isopropyl
o	*Ortho*
m	*Meta*
p	*Para*
t_D	Drift time

Chapter 1
General Introduction

Abstract This chapter provides a general introduction to the main topics of the present thesis. In the first part of this chapter, the advantages and challenges of direct C–H activation, recent progresses in *meta*–selective C–H activation as well as asymmetric C–H activation and functionalization will be briefly reviewed. In the second and third parts of this chapter, introductions to mass spectrometry and computational chemistry as well as their applications in mechanistic studies will be presented.

1.1 Introduction to C–H Activation

1.1.1 Advantages and Challenges of Direct C–H Activation

Using environmentally benign reagents, improving synthetic efficiency and reducing side products are important goals for modern synthetic organic chemistry [1–3]. Traditional organic synthesis methods highly rely on the transformation of functional groups. For example, the transition metal-catalyzed cross-coupling reactions (Suzuki coupling [4], Still coupling [5], Heck reaction [6, 7] and Negishi coupling [8]) provide important approaches for constructing C–C and C–X (X = heteroatom) bonds and are widely applied in academic research and industry. These coupling methods have greatly promoted the development of organic synthesis. The 2010 Nobel Prize was awarded to the three chemists: Richard F. Heck, Ei-ichi Negish, and Akira Suzuki for their outstanding contributions in Pd-catalyzed cross-coupling reactions [9]. However, these coupling reactions which are based on the transformation of functional groups use prefunctionalized substrates and generate a large amount of by-products (e.g., metal halides).

C–H bond is the most common chemical bond which exists ubiquitously in almost all organic compounds, ranging from simple hydrocarbon molecules to complex pharmaceutical molecules and polymer materials. C–H activation undoubtedly offers a powerful tool for the direct conversion of ubiquitous C–H bonds into diverse functional groups. It also provides an unprecedented disconnection strategy for constructing C–C and C–X bonds, thus providing new ideas for

the retrosynthetic analysis of complex target molecules. Compared to traditional methods based on functional groups transformations, the direct C–H activation approaches are more atom- and step-economical and environmentally friendly since no prefunctionalization step is required which will simplify the synthesis process and reduce by-products.

Reactivity Problem. However, C–H bonds are generally viewed as inert chemical bonds due to their high bond energy and low polarity. Transition metals were found to be able to promote the C–H bond cleavage. The generated metal–carbon bond is more reactive than C–H bond which can undergo further transformations under milder conditions. Various transition metals (e.g., Pd, Ni, Rh, Ru, Co, Cu, Fe) have been applied in C–H activation and functionalization. Transition metal-catalyzed C–H activation has revolutionized the synthetic field and found versatile applications in the synthesis of natural products, pharmaceutical molecules, and other organic compounds. In recent decades, the direct C–H activation has become one of the most active research fields and made much outstanding progress [10–17].

Selectivity Problem. Despite these advances, the control of selectivity remains a significant challenge for direct C–H activation. Because C–H bonds widely present in organic molecules, it is critical to differentiate C–H bonds and selectively activate the desired C–H bond. One of the approaches to control selectivity is based on the electronic effect. One example is the classic electronic aromatic substitution (S_EAr) reaction in which the electron-donating substituent directs the electrophile to the *ortho* and *para* position, while the electron-withdrawing substituent direct the electrophile to the *meta* position. But this method always generates multisubstituted products. On the other hand, this approach is limited to the electron-rich arenes since the electron-poor arenes usually lack reactivity.

Control Site-selectivity by Electronic Effect. Fagnou and coworkers have developed the intermolecular arylation reactions of electron-poor arenes (Eqs. 1.1 and 1.2) [18, 19]. Opposite to the selectivity observed in traditional S_EAr reactions, they found that the electron-donating group, methoxyl group, directs the reaction to occur at the *meta* position while the electron-withdrawing group leads to *ortho* product. Computational studies revealed that the reaction operates through proton transfer mechanism instead of the traditional S_EAr mechanism. Therefore, the reaction selectively activates the most acidic C–H bond.

$$(1.1)$$

$$(1.2)$$
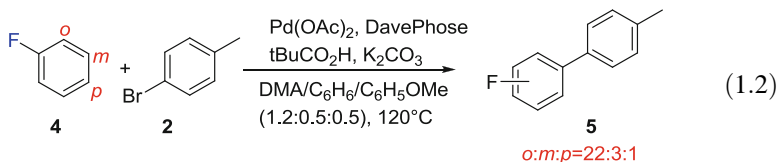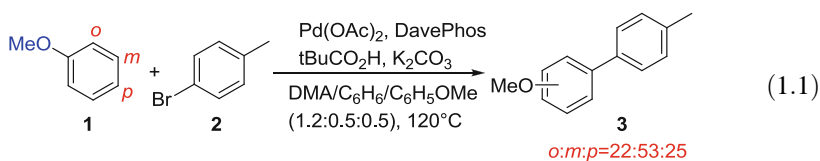
Control Site-selectivity by Steric Effect. Another strategy to control the selectivity of C–H activation reactions is differentiating C–H bonds by steric factors. For instance, the olefination reaction of N–Bn-protected indole (**6**) generates products **7** and **8** in a ratio of 2.1:1 because these two C–H bonds at the 2- or 3-position of **6** have similar reactivities (Eq. 1.3). When the electron-withdrawing groups such as Ac, Boc, or T_S groups are used as protecting group, the reactivity of the C–H bond at 2-position is significantly higher than the C–H bond at 3-position and the selectivity is increased to be 95:5. While the bulky group, 2,4,6-triisopropylsulfonyl (TIPS) group, drives the reaction selectivity to occur at 3-position (**7:8** < 5:95) because the large steric congestion at 2-position prevents the formation of product **7** [20] (Table 1.1).

$$(1.3)$$
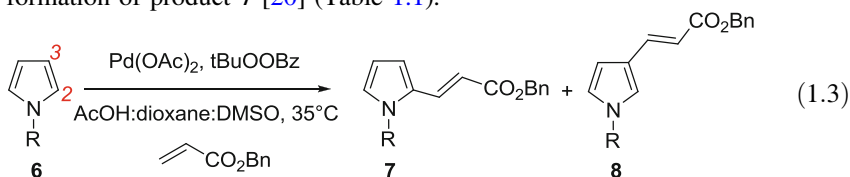
Table 1.1 Pd-catalyzed olefination reaction of N–protected indole (**6**)

R	Yield of **7**	Yield of **8**	Ratio **7:8**
Bn	48	23	2.1:1
Ac	65	–	>95:5
Boc	73	–	>95:5
Ts	70	–	>95:5
TIPS	–	78	<5:95

Control Site-selectivity by Directing Group. However, most organic molecules contain multiple C–H bonds with similar chemical properties or similar steric environments. It is difficult to control the selectivity and differentiate the C–H bonds by the subtle differences in electronic or steric factors. The chelation-assisted C–H activation in which a chelation group directs transition metal to the proximity of a C–H bond (usually *ortho* C–H bond) has been developed quickly. In 1963, Kleiman and Dubeck reported the first Ni-catalyzed selective activation of aromatic C–H bond [21]. They heated azobenzene and $NiCp_2$ at 135 °C for 4 h and obtained cyclometalated complex **10**. Here the azo group directs Ni to its proximity, activating the *ortho* C–H bond with high selectivity (Eq. 1.4). This is the first work which controls the selectivity of C–H activation by directing group.

$$(1.4)$$
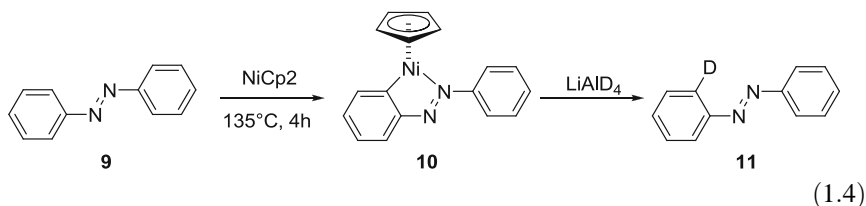
In recent decades, organic chemists have developed various directing groups for selective C–H activation, such as pyridine group [22–26], carboxylate group [27–29], hydroxyl group [30, 31], amide group [32–35], acetamido group [36–39], and other functional groups with nitrogen, oxygen or sulfur atom as coordination atom. These directing groups have been widely applied in selective C–H activation reactions, especially in $C(sp^2)$–H activations. In recent years, the bidentate directing groups, such as 8-aminoquinoline and picolinic acid auxiliaries [40–42], have been extensively developed and used in $C(sp^3)$–H activation and functionalization. According to the derivatization of the directing groups, they can be classified into three kinds of directing groups: (I) the directing group remains as part of the product **13** after the C–H activation and functionalization of the substrate, or the directing group undergoes cyclization reaction to form heterocyclic compound **14**. This kind of directing groups will stay in the structure of the final product which is difficult to eliminate or undergo various transformations, limiting the structural diversity of product; (II) the directing group is eliminated or further transferred to functionalized product **17** after the C–H activation and functionalization; (III) the C–H activation/functionalization as well as the elimination of directing group are realized in one-pot reaction, therefore, no extra reaction process is required to release the directing group (Fig. 1.1). But currently, only limited one-pot reactions with directing group **3** have been reported. Directing groups assisted C–H bond activation reactions have been amply reviewed elsewhere [13, 42–44], hence no more discussion will be presented here.

Although significant progresses have been made in directing group-assisted selective C–H bond activation, this method is generally limited to the *ortho-*

Fig. 1.1 Three classes of directing group used in transition metal-catalyzed C–H bond activation and functionalization

selective C–H bond activation. The *meta-* and *para*-selective C–H activation of arenes remain challenging. The following section will introduce recent breakthroughs for *meta*-selective C–H activation of arenes in detail.
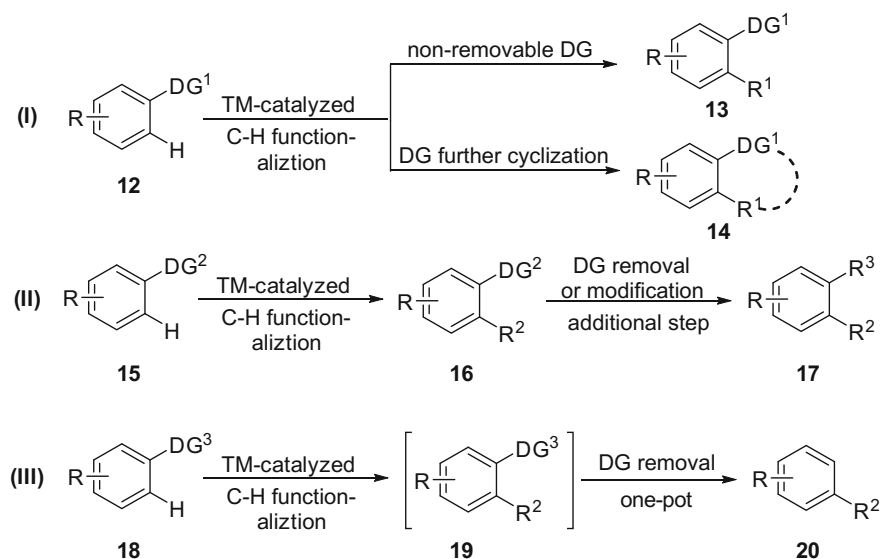
1.1.2 Meta-*C–H Activation of Arenes*

Compared to the extensively studied *ortho* C–H activation, the *meta*-C–H bond activation of arenes lags far behind. As introduced in Sect. 1.1, for traditional electrophilic aromatic substitution reactions with the electron-rich arenes, the electron-donating group usually directs *ortho* and *para* C–H bond activation, while the electro-withdrawing group which is *meta*-directing group decreases the reactivity. On the other hand, the widely adopted directing group strategy generally leads to *ortho* selectivity. Developing *meta*-selective C–H activation method has attracted much attention and made some significant breakthroughs in recent years which are summarized below.

Meta-**C–H Activation of Electron-poor Arenes**. In 2009, the Yu group reported the first Pd(OAc)$_2$-catalyzed *meta*-selective C–H bond activation/olefination of electron-poor arenes [45]. Generally, palladium-catalyzed C–H activation/olefination reactions of arenes (oxidative Heck reaction) are limited to electron-rich substrates. It is difficult for the electron-poor arenes to undergo oxidative heck reaction under the commonly applied reaction condition of Heck reaction which is mainly due to the weak binding affinity of electron-poor arenes which disfavors the substrate to coordinate with the Pd catalyst. Thus, the electron-poor arenes cannot stabilize Pd(0). Pd catalyst will quickly become palladium black and lose catalytic ability in the absence of other ligands. The Yu group screened various ligands for the C–H activation/ olefination reaction of 1,3-di-trifluoromethyl-benzene and found the most frequently used pyridine ligand leads to poor yield which is possibly because the electron-poor substrate cannot compete with pyridine to bind with Pd since the latter is a strong coordinating ligand. The ideal ligand should be able to coordinate with Pd efficiently to stablize Pd(0) and at the same time only occupy one binding site of Pd to leave available binding site for electron-poor substrate. Based on this idea, they designed 2,6-disubstituted pyridine derivative **25** which dramatically improves the reactivity and obtains a yield of 52% (Eq. 1.5).

The authors proposed that the bulky substituent of ligand **25** prevents the coordination of a second ligand **25** with Pd. Therefore, only one ligand **25** binds with Pd and leaves a binding site for the substrate. To verify this hypothesis, they synthesized complex **26** (Pd(OAc)$_2$(**25**)$_2$). The ^{1}H NMR experiment in solvent detected the dissociation of one molecule of ligand **25** to generate dimeric complex **28** which supports their hypothesis. In the meanwhile, they suppose that the *meta*-selectivity is originated from the steric effect of the ligand. The Zhang group conducted mechanistic study on this reaction [46]. Computational results indicate that the C–H activation step is the rate-determining step and regioselectivity determining step. The C–H activation occurs via concerted metalation and

Mechanistic study
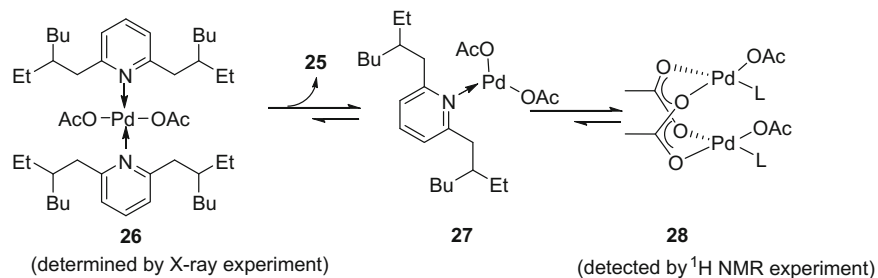
Fig. 1.2 Mechanistic study on Pd(OAc)$_2$-catalyzed *meta*-selective C–H bond activation/olefination reaction of electron-poor arenes

deprotonation (CMD) mechanism. The computational results also reveal that the *meta*-selectivity is primarily due to the steric effect and weak electronic effect. The large steric congest of the bulky substituent hinders the *ortho* C–H activation and weak electronic effect prevents the *para* C–H activation (Fig. 1.2).
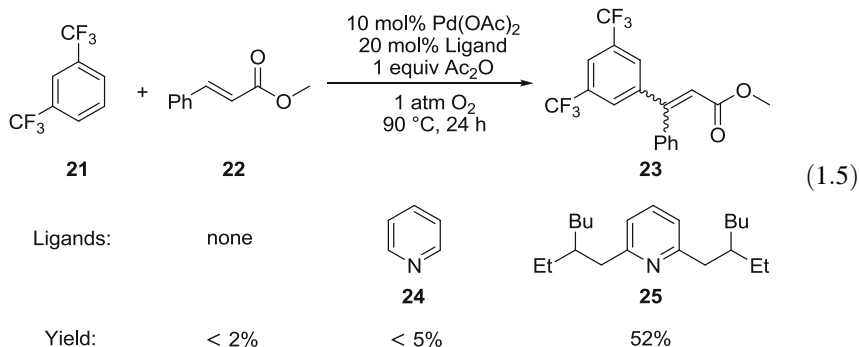
Cu-catalyzed *meta*-selective C–H Activation. In 2009, the Gaunt group published the first Cu(OTf)$_2$-catalyzed and amide directed *meta*-selective C–H activation/arylation reaction [47]. Meta-selective arylations of a variety range of anilide substrates were realized under the mild condition. While the previous similar arylation reaction of anilides catalyzed by Pd catalyst generates *ortho*-arylated products (Eq. 1.6) [48]. To understand the uncommon *meta*-selectivity, the authors proposed an "oxy-cupration" mechanism which is illustrated in Fig. 1.3. The diphenyliodonium triflate reagent, Ph$_2$IOTf, oxidizes Cu to a strong electrophilic species, Cu(III)–Ph, which attacks the *meta* position of acetanilide to form Cu–C bond and at the same time the carbonyl group undergoes nucleophilic attack at the *ortho* position of substrate, affording intermediate **32**. The aromaticity of substrate is destroyed during this anti-oxycupration process. In the following step, OTf$^-$ group abstracts the proton at *meta* position which recovers the aromaticity of the benzene ring. Finally, reductive elimination of complex **33** leads to the *meta*-arylated product **31**.
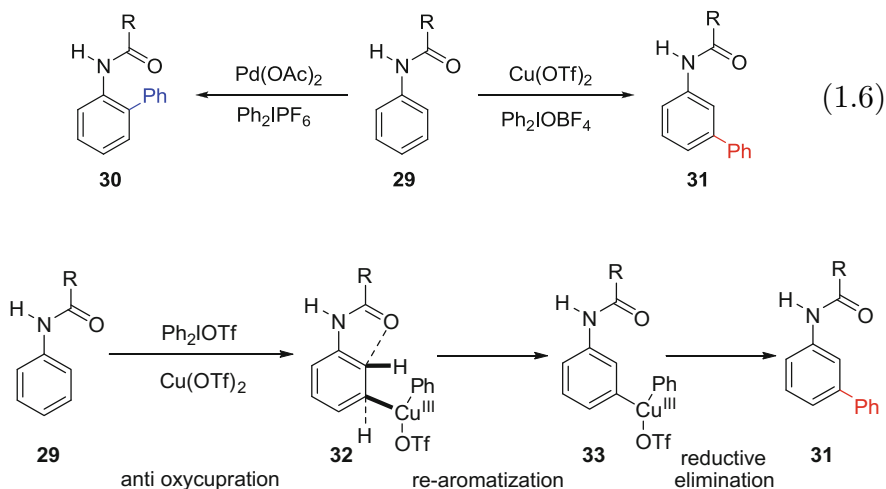
Fig. 1.3 Cu-catalyzed *meta*-C–H activation and arylation reaction of anilide and the oxy-cupration mechanism proposed by Gaunt and coworkers

Li, Wu and coworkers conducted experimental and theoretical studies on this reaction [49]. Computational results suggest that the activation barrier for the electrophilic attack process by Cu(III)–Ph is as high as 50.7 kcal/mol which demonstrates that "oxy-cupration" mechanism proposed by Gaunt is unreasonable. Instead, they proposed a new "Heck-like" mechanism for the *meta*-C–H activation. As shown in Fig. 1.4, the carbonyl group coordinated Cu(III) species attacks the anilide ring via a "Heck-like" four-membered ring transition state **36** and leads to *meta*-C–H activated and functionalized product **31**. While the concerted metalation and deprotonation (CMD) pathway affords *ortho* product **30**. In addition, they calculated the activation barriers for *meta*- and *ortho*-C–H bond activations for a number of anilides with different substituents. In most cases, the "Heck-like" transition state has a lower barrier than CMD transition state, therefore the formation of *meta*-product is more favorable which is consistent with experimental observation. Here, the high oxidation state Cu(III) complex abstracts electron from the substrate which dramatically increases the electrophilicity of anilide, facilitating the "Heck-like" pathway.

Metalation Induced *meta*-selective C–H Activation. In 2011, the Frost group reported the [Ru(*p*-cymene)Cl₂]₂-catalyzed and pyridine directed *meta*-selective sulfonation reaction (Eq. 1.7) [50]. To understand the mechanism, they synthesized the cyclometalated intermediate **39**. The reaction of both stoichiometric and catalytic amount of complex **39** with TsCl afforded the *meta*-sulfonated product. KIE (kinetic isotope effect) experiment indicates the C–H bond activation possibly is the rate-determining step ($k_H/k_D = 3.0$). Additionally, Frost and coworkers found that no *meta*-sulfonated product obtained when one of the *meta* positions of pyridine is substituted by a methyl group. Based on these observations, they proposed that the
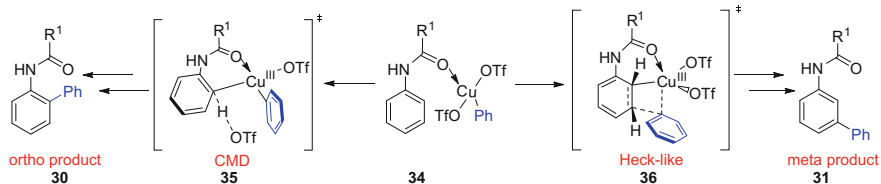
Fig. 1.4 Proposed mechanisms for Cu-catalyzed *meta-* and *ortho-*C–H bond activation and functionalization in ref. [49]

reaction proceeds via a five-membered cyclometalated complex **39**. In complex **39**, the newly formed Ru–C$_{aryl}$ σ–bond introduces a strong *para*-directing effect which directs the following electrophilic aromatic substitution to take place at the *para* position (i.e., *meta* to pyridine group). For the substrate where one of the *meta*-positions is substituted by methyl group, the *para* position of Ru–C$_{aryl}$ σ–bond will be blocked by methyl group because the cyclometalation likely proceeds via the least hindered C–H bond which leads to a complex where methyl is *para* to Ru–C$_{aryl}$ σ–bond and thus blocks the sulfonation reaction.

(1.7)
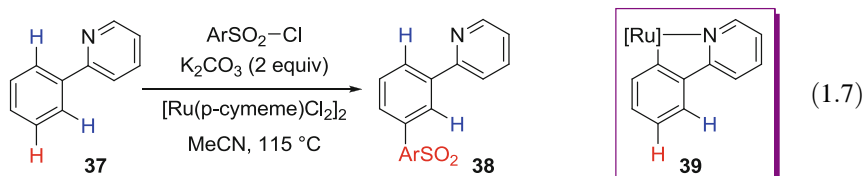
The Fu group performed mechanistic studies on this reaction [51]. They concluded that the reaction mainly involves four steps: *ortho* C–H activation, electrophilic aromatic substitution, reductive elimination, and catalyst regeneration. Among these four steps, the C–H activation is the rate-determining step and the electrophilic aromatic substitution step is the regioselectivity determining step. NBO charge analysis illustrates that the formation of Ru–C$_{aryl}$ σ–bond changes the electron density distribution at the benzene ring. As shown in Fig. 1.5, the Ru–C5 bond increases the electron density of its *ortho* and *para* carbon atoms, i.e., C4 and C2. Therefore, C4 and C2 atoms are more nucleophilic. Because of the steric congestion at *ortho* position, the sulfonation reaction mainly occurs at *para* position which is *meta* to the pyridine group.
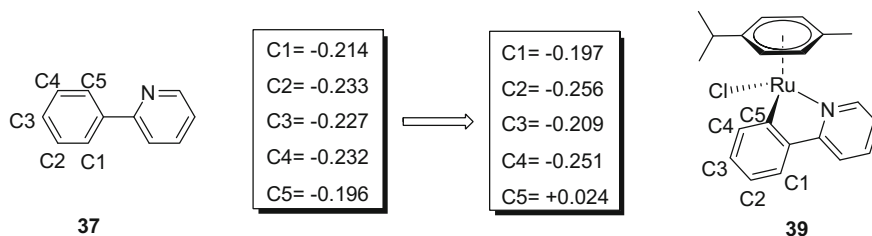
Fig. 1.5 NBO charge analysis of substrate **37** and cyclometalated ruthenium complex **39**

   In 2013, the Ackermann group published a Ru-catalyzed and pyridine directed *meta*-alkylation reaction (Eq. 1.8) using a similar strategy [52]. Different from the sulfonation reaction reported by the Frost group, this alkylation reaction is applicable across *ortho*, *meta*, or *para* substituted arenes [53]. The deuterium labeling experiment suggests that the *meta*-C–H bond cleavage is kinetically not relevant. In addition, the intermolecular competition experiments between primary and secondary alkyl halides revealed that the primary alkyl halide prefers to afford *meta*-alkylated product, while the latter one favors *ortho*-alkylation reaction (Eq. 1.9). The detailed mechanism remains unclear currently.

$$(1.8)$$

$$(1.9)$$
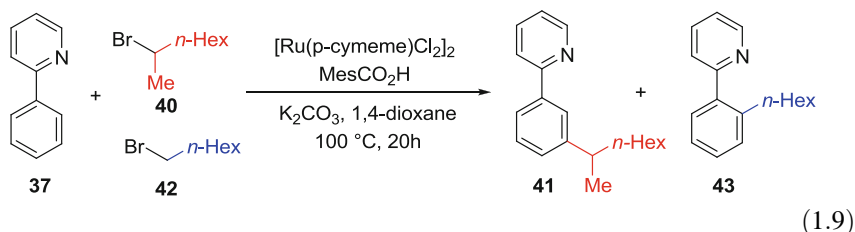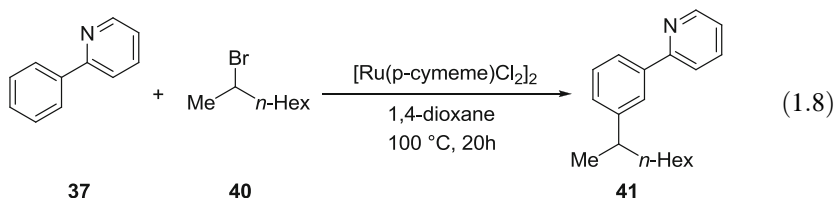
   After the pioneer works from these two groups, the *ortho*-metalation strategy has been extended to other *meta*-selective C–H activation and functionalization reactions, such as mono- and difluoromethylations of arenes and alkylation reactions [54–56].

   Remote C–H bond Activation Using Template Strategy. In 2012, the Yu group reported a Pd-catalyzed *meta*-selective C–H activation and olefination reaction with an ingeniously designed template [57]. The end-on nitrile group of template directs Pd catalyst to the proximity of *meta*-C–H bond of the substrate which is 10 or 11 chemical bonds away from the nitrile group. Different from conventional chelation-assisted C–H activation reactions which proceed via conformationally rigid five- or six-membered ring pre-transition state and afford *ortho*-functionalized products, this reaction takes place through a macrocyclic pre-transition state which is generally considered as unstable complex and obtains *meta*-olefinated product. This work represents a significant breakthrough in the research field of *meta*-C–H bond activation and opens new opportunities for remote C–H activation. However, the reaction mechanism and the origin of *meta*-selectivity were unclear. The mechanistic studies will be introduced in Chap. 2.

   Since the Yu group's first report, the template strategy has rapidly been applied to a series of *meta*- and *para*-selective C_{aryl}–H activation and functionalization [57–70]. Figure 1.6b lists the various substrate classes which were activated using the

template strategy reported in literature. These reactions are based on Pd catalyst. Recently, the Yu group extended the template strategy to Rh catalyst for *meta*-selective C–H olefination and they proposed a Rh(III)/Rh(I) catalytic cycle [71]. This diverse collection of examples of template strategy demonstrates its great potential in obtaining unusual selectivities for arene functionalization. A deeper understanding on the reaction mechanism undoubtedly will facilitate the development of this research field.
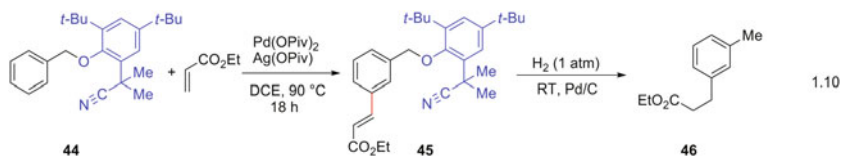
$$(1.10)$$
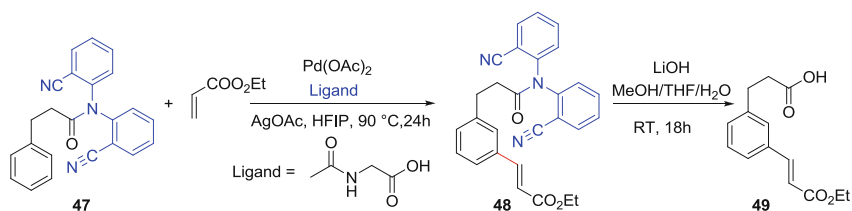
$$(1.11)$$
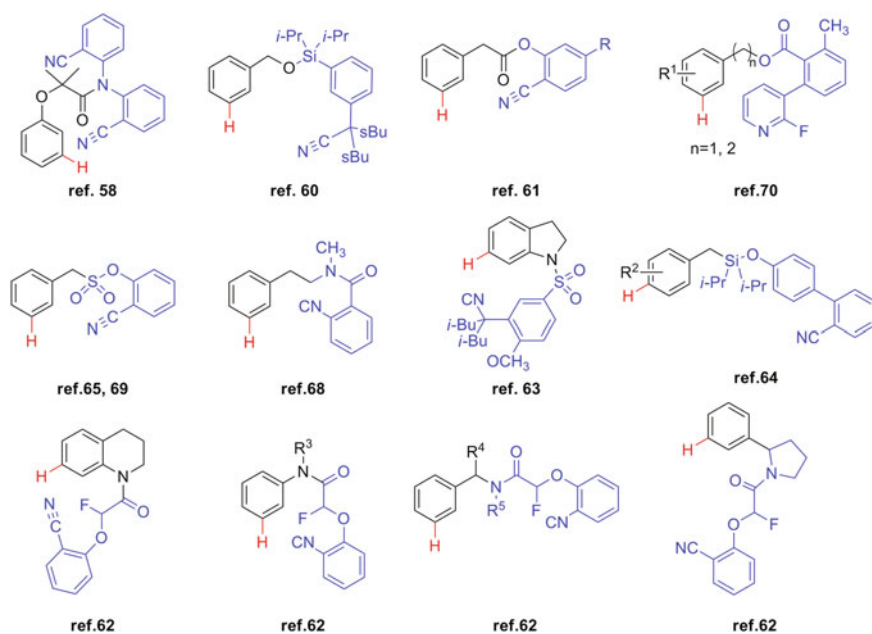
Fig. 1.6 Remote C$_{aryl}$–H bond activation employing end-on template

***Meta*-selective C–H Bond Activation Controlled by Steric Factors**. In 2014, the Hartwig group published a Rhodium-catalyzed highly regioselective C–H activation and silylation reaction of 1,2-substituted arenes [72]. In previous works, steric effect has been successfully applied to control the regioselectivities of Ir-catalyzed or Pd-catalyzed C–H activation and functionalization of monosubstituted (**50**), 1,3-disubstituted (**51**), and symmetric 1,2-disubstituted (**52**, $R^1 = R^2$) arenes. By comparison, it is a great challenge to control the regioselectivity of C–H activation of asymmetric 1,2-disubstituted arenes. The difficulties are associated with the differentiation of subtle difference of steric properties of groups (R^1 and R^2) which are distal to the C–H bonds at C4 and C5 positions. The Hartwig group developed the catalytic system **53** and successfully activates the C–H bond which is *para* to the largest substituent and *meta* to the smaller substituent with high regioselectivity. It is found that catalyst **53** is very sensitive to steric hindrance and is able to discriminate series of groups with different sizes to achieve excellent regioselectivity.
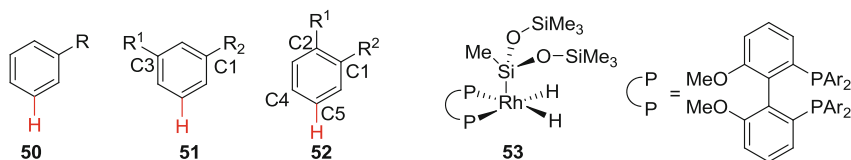
Transient Directing Group-mediated *meta*-selective C–H Activation. Phenols are ubiquitous motif in natural product and pharmaceutical molecules, as well as versatile building blocks in organic synthesis. The direct *ortho*- and *para*-functionalization of phenols has been extensively explored, while the *meta*-C–H activation and functionalization generally requires multiple reaction steps. In 2014, the Larrosa group reported a one-pot synthesis of *meta*-selective arylation of phenols (Eq. 1.12) [73]. They reacted **54** with KOH under 25 atm of CO_2 at 190 °C for 2 h, then added iodoarene, Pd catalyst, Ag_2CO_3, and AcOH, and further reacted at 130 °C for 16 h, obtaining the *meta*-arylation product **57**. This reaction can tolerate various substrates bearing different electron-donating and electron-withdrawing groups. In this approach, CO_2 acts as traceless directing group to induce the arylation reaction occurs at the *meta* position selectively.

$$(1.12)$$
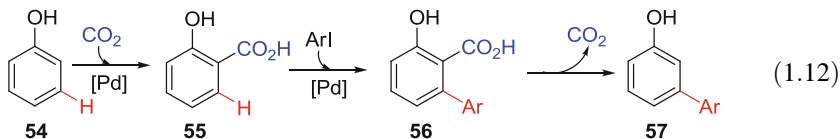
Recently, the Yu group reported a *meta*-C–H activation and functionalization of arenes using norbornene as a transient mediator which switches the *ortho*-selectivity to *meta*-selectivity (Eq. 1.13) [74]. In this approach, the arene bearing an *ortho*-directing group initially reacts with Pd catalyst to form cyclometalated complex **61**. Then norbornene inserts into Pd–C bond and directs Pd to activate the *meta*-C–H bond, affording complex **62**. The following coupling between aryl halide and complex **62** leads to intermediate **63**. Finally, protonation of complex **63** and dissociation of Pd generates the *meta*-arylated product **59** (Fig. 1.7). Differs from the conventionally reported chelation-assisted C–H functionalization reactions which generally get *ortho*-products, this approach overrides the *ortho*-directing effect of the original directing group (amide group) to achieve the more challenging *meta*-selectivity. But the greatest challenge of this approach is the potential competition reactions. For example, the intermediate **61** may couple with electrophile to form *ortho*-functionalized product, the intermediate **62** may undergo reductive elimination to afford benzocyclobutene product, and the intermediate **63** may further react with electrophile to generate the disubstituted product. Therefore, it is a great challenge to selectively achieve the desired *meta*-functionalized product among these various competition reactions. The tailor-made ligand **60** developed by the Yu group was found to have excellent performance in suppressing the side reactions and promoting the *meta*-C–H functionalization reaction. This work provides a novel and potentially general strategy for *meta*-C–H activation and functionalization. Soon after this seminal work, the strategy of using norbornene (or modified norbornene) as transient mediator have been quickly developed and applied to various *meta*-selective C–H arylation, alkylation, alkynylation and amination reactions [75–79]. The ligand is found to be crucial for these reactions to proceed.

$$(1.13)$$
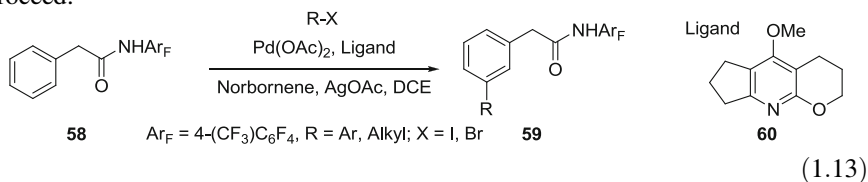
Secondary Interaction Directed *meta*-selective C–H Activation. In 2015, Kuninobu, Kanai and coworkers reported a novel concept of utilizing secondary interaction between ligand and substrate to control regioselectivity of C–H transformations [80]. They developed an Ir-catalyzed *meta*-selective C–H borylation reaction of arene derivatives using a bipyridine-derived ligand (red part in complex **66**). It is proposed that the hydrogen bonding interaction between the pendant urea moiety of ligand and the carbonyl group of the substrate brings the Ir catalyst to the proximity of *meta*-C–H bond (Fig. 1.8, **66**) and hence leading to *meta*-selectivity. The involvement of this secondary interaction is supported by ^{1}H NMR and control
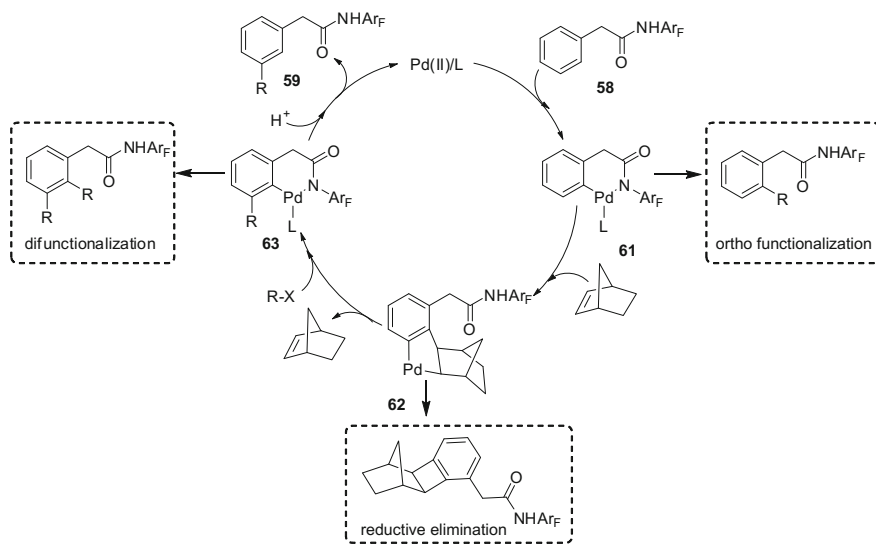
Fig. 1.7 Norbornene-mediated *meta*-C–H activation and proposed reaction process as well as the possible by-products

experiments. This strategy does not need installation and removal of directing groups at substrate and common functional groups can be used for catalyst directing. Thus, it offers an alternative and potentially versatile approach for regioselective C–H activation. Recently, the Phipps group reported an ion pair-directing strategy for regioselective C–H transformations [81].

$$(1.14)$$
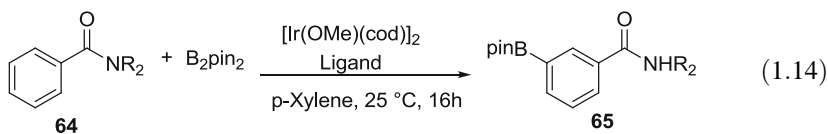
Fig. 1.8 *Meta*-selective C–H borylation mediated by the secondary interactions between ligand and substrate
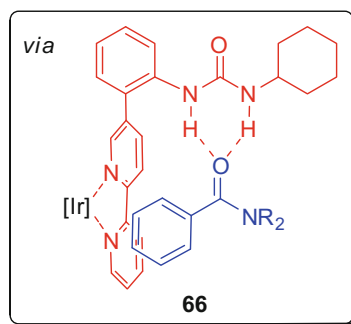
1.1.3 Asymmetric C–H Activation and Functionalization

Chirality lies in the heart of chemistry, pharmacology, and biology. The direct asymmetric C–H activation and functionalization provides a powerful and highly appealing method to construct chiral compounds since it directly uses the simple hydrocarbons as starting materials without prefunctionalization which improves the synthetic efficiency and reduces wastes. One of the great challenges in this field is how to discriminate the multiple C–H bonds with similar properties in one single molecule. In addition, most C–H bond activation reactions still proceed under harsh reaction conditions, e.g., high temperature, which influences the stability of the chiral intermediate and the efficiency of chirality relay. Asymmetric C–H activation and functionalization reactions have been rapidly developed in recent decades and received growing attentions.

Conceptually, transition metal-catalyzed asymmetric C–H activation and functionalization reactions can be divided into two main categories: (1) reactions in which the stereoselectivity is controlled by the C–H activation step and (2) reactions in which the chirality is induced at the functionalization step subsequent to a non-stereoselective C–H activation event. For the first kind of reaction, the new chiral center is constructed by prochiral C–H bond cleavage (e.g., asymmetric insertion of cabene, nitrene, and organometal into C–H bond, desymmetric C–H activation), and atroposelective C–H bond activation. The chirality generated in the C–H activation step is maintained in the subsequent functionalization step. For the second class of reaction, C–H bond is activated in a non-stereoselective way, then the generated metalated complexes are functionalized stereoselectively via selective insertion of alkene or alkyne into the C–M (M = transition metal) bond or trans-metalation or reductive elimination (e.g., asymmetric olefin insertion, asymmetric oxidative biaryl coupling, asymmetric cross-dehydrogenative coupling).

There have been many reviews and books introducing this active field published in literature [82–85]. Thus only some selected asymmetric C–H activation and functionalization reactions are introduced here.

1.1.3.1 Asymmetric C–H Activation

It is an appealing approach to induce chirality in C–H activation step because the generated chiral [C–M]* complex can be converted to various chiral products via a variety of functionalization reactions, like C–C, C–N, C–O, or C–X bond formation reactions.

Atroposelective C–H Bond Activation. In 2000, The Murai group applied this strategy in the synthesis of atropoisomeric biaryl scaffolds [86]. They installed a substituent in the ortho position of achiral aryl pyridine substrate via a Rh-catalyzed

C–H activation and olefination reaction which prevents the rotation around C_{aryl}–C_{aryl} bond, introducing the axial chirality in this system. Though the enantio excess of this reaction is only 49%, this early work demonstrated the practicability of this strategy.

$$(1.15)$$
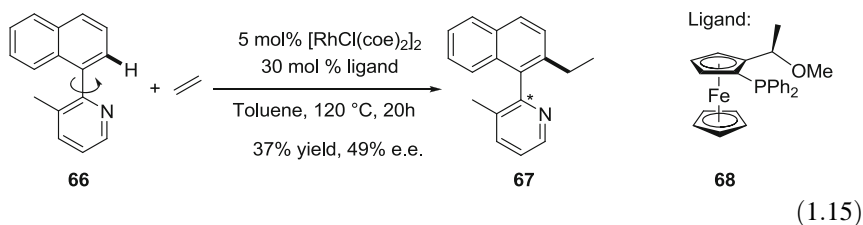
Desymmetric C–H Bond Activation. In 2008, the Yu group made significant progress in enatioselective C–H activation. They developed a highly enantiose-lective C–H activation and functionalization reaction via direct desymmetric C–H activation. As shown in Eq. 1.16, they realized the asymmetric C–H functional-ization of 2-biphenyl-methyl pyridine via Pd-catalyzed alkylation reaction employing a mono-N-protected amino acid (MPAA) as chiral ligand [87]. The reaction works for a broad of substrates with high enantioselectivities [82, 88–91]. The Pd/MPAA catalyst system has been applied to series of enantioselective C–H activation and functionalization via desymmetric C–H activation of achiral sub-strate or kinetic resolution of racemic substrate. The successful applications of MPAA in asymmetric C–H activation and functionalization reactions have demonstrated that MPAA is a promising chiral ligand, while the specific mecha-nism of how does MPAA control the enantioselectivity was unclear. Pd/MPAA-catalyzed asymmetric C–H activation and functionalization reactions as well as the mechanistic studies will be described in detail in Chap. 4.

$$(1.16)$$
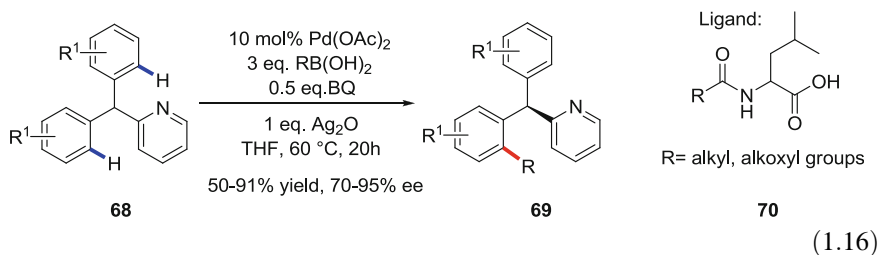
Besides the application in desymmetric C–H activation reactions, MPAA is also used in kinetic resolution. Recently, Yu and coworkers reported an efficient enantioselective C–H iodination reaction via kinetic resolution for the synthesis of chiral amines [92]. As shown in Eq. 1.17, when using L–Bz–Leu–OH as ligand, the *R* enantiomer of racemic benzylic amine undergoes the iodination reaction much faster than the *S* enantiomer (k_{fast}/k_{slow} up to 244), which leads to an excellent enantioselectivity (up to 99% *e.e.*). The recovered starting material can be further

iodinated by using D–Bz–Leu–OH as ligand. This reaction takes place at room temperature and employs simple MPAA as chiral ligand to realize the enantiose-lective C–H iodination of both enantiomers of the racemic substrate, obtaining enantiomerically pure chiral amines.

Pd/MPAA catalyst was applied to the enantioselective C–H arylation of cyclo-propylmethyamines. Both diastereomers **76** and **77** can be synthesized with high selectivity by using L- and D-MPAA ligands, respectively (Eq. 1.18) [93]. The enantioselective C–H cross-coupling of benzylamines and enantioselective olefination of α-hydroxy and α-phenylacetic acids were also achieved via kinetic resolution method using MPAA ligands [33, 94].

The desymmetric C–H activation strategy was also applied by the Cramer group to achieve the enantioselective C–H activation and cyclization reaction in 2009. This reaction is believed to undergo oxidative addition first to insert Pd into the C–OTf bond then selective C–H activation and reductive elimination to form a new five-membered ring [95]. In the proposed TS (**84**) for C–H activation, the ligand is expected to bind with Pd in a monodentate way in order to leave binding sites for substrate and acetate group. Thus they screened various bulky monodentate phosphorus ligands and identified **80** as the optimal ligand which leads to a high enantioselectivity of 97% *e.e.* This approach has been successfully employed to construct various 5-, 6-, and 7-membered ring structures [96–101].

(1.17)

74
96% yield
93% ee

75
98% yield
93% ee

76
80% yield
45% ee

77

proposed TS
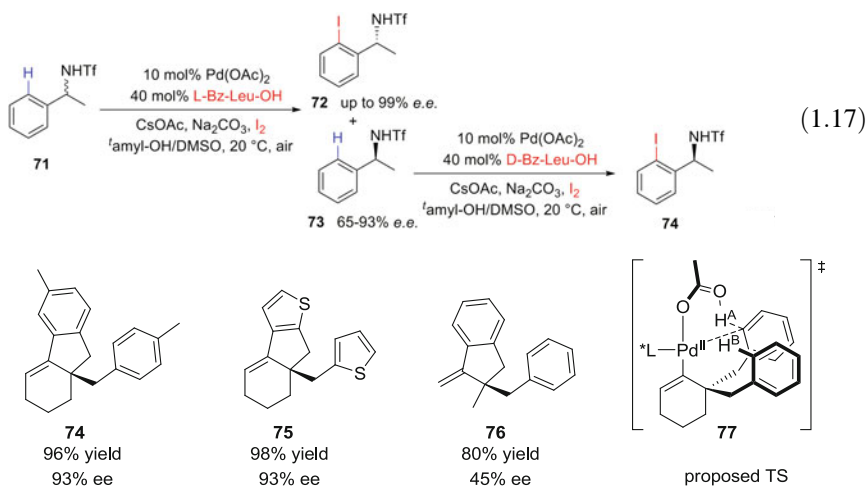
ligand	major diastereomer	yield	dr (major:minor)
Boc-Gly-OH	**76**	11%	2:1
Boc-L-Val-OH	**76**	35%	> 20:1
Boc-D-Val-OH	**77**	28%	> 20:1

(1.18)
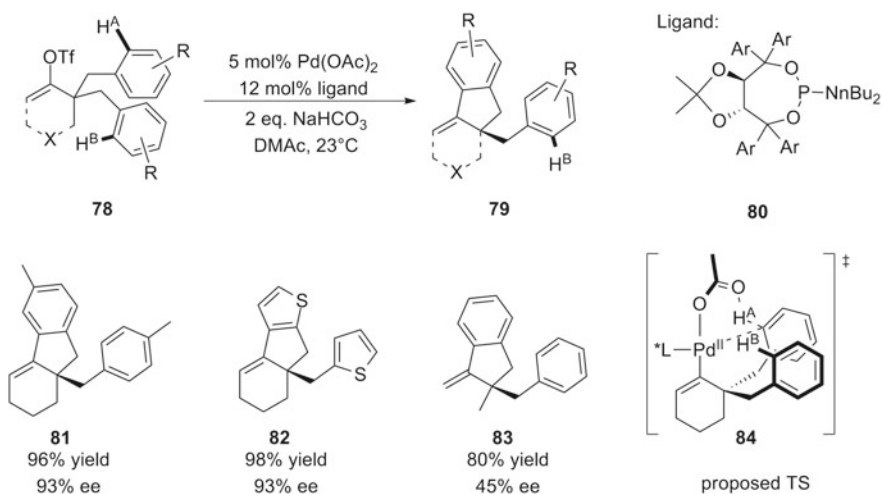
(1.19)

1.1.3.2   C–H Activation Followed by Asymmetric Functionalization

Stereoselective Functionalization of Metalated Intermediate ([**C–M**]). The introduction of chirality in the functionalization step following the C–H bond activation is an important strategy for asymmetric C–H activation and

functionalization. The Hartwig group reported the Ir-catalyzed asymmetric hete-rocyclic arylation of norbornene (Eq. 1.20) [102]. In this reaction, the Ir/DTBM-Segphos catalyst system is effective in activating the C–H bond of var-ious heterocyclic compounds such as indole, thiophene, pyrrole, and furan. The chiral products were obtained in the stereoselective olefin insertion and reductive elimination step with high selectivity.
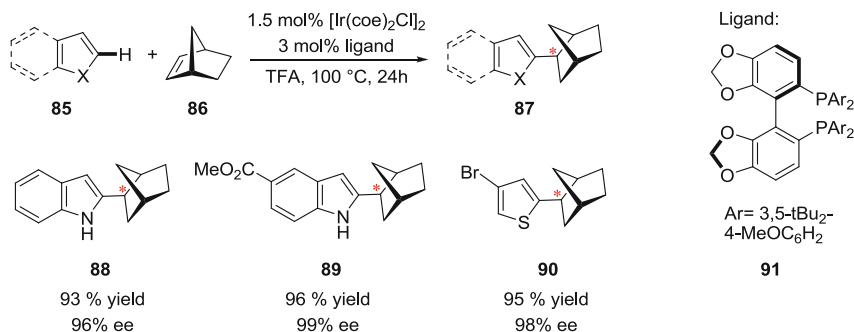
$$(1.20)$$

The Bergman and Ellamn group developed the Rh-catalyzed asymmetric intramolecular alkylation reaction (Eq. 1.21) [103]. This enantioselective cycliza-tion reaction of arylamine substrate proceeds via *ortho*-C–H activation followed by intramolecular double bond insertion and reductive elimination which affords the chiral product **93**. Ligand screening experiments suggested that the axially chiral ligand **94** was the optimal ligand which could lead to a stereoselectivity up to 96%. The stereoselectivity of the reaction is considered to be determined by the olefin insertion step.
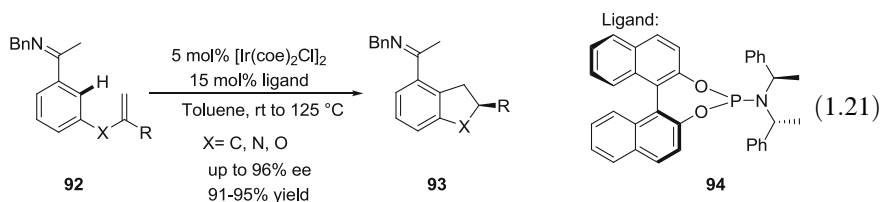
$$(1.21)$$

Asymmetric Oxidative Biaryl Coupling. The axially chiral biaryl compounds are important chiral ligands and their synthesis has attracted extensive attention. The construction of atropoisomeric biaryl scaffolds via asymmetric oxidative coupling provides an essential and most atom economical method to synthesize axially chiral biaryl compounds. For instance, the Brussee group [104, 105] and the Kocovsky group [106] have reported the synthesis of chiral BINOL by the asymmetric oxidative coupling of naphthol in 1983 and 1992, respectively. The Brussee group obtained a yield of 98% and high enantioselectivity of 96% with

CuCl$_2$ catalyst and ligand **97**. The Kocovsky group used CuCl$_2$ catalyst and ligand **98** to get 36% yield and an enantioselectivity of 96%.
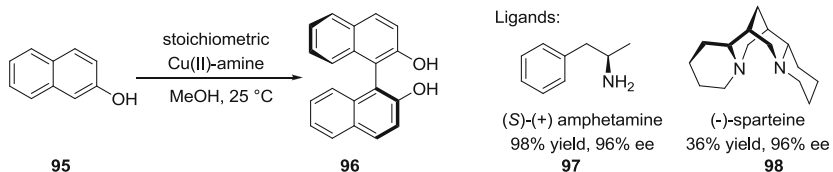
$$(1.22)$$

1.2 Introduction to Mass Spectrometry

Mass spectrometry (MS) is an analytical technique providing both qualitative and quantitative information via measuring the mass-to-charge ratio of ion. The basic working principle of the mass spectrometer is: the sample is ionized in the first place, then ions are separated based on their different movements in the electric field or magnetic field. Then these ions are detected and the ion signal as well as mass-to-charge ratio are recorded in form of mass spectrum. A mass spectrometer is mainly composed of an injection system, an ion source, a mass analyzer, a detector and a data processing system.

As early as 1886, the German physicist E. Goldstein observed the positively charged particles in the low-pressure discharge experiment for the first time, and then W. Wein found that the positively charged ion beam could deflect in the magnetic field or electric field and he established the parallel electromagnetic field for separating positively charged ion beam. In 1912, Thomson created the first mass spectrometer in the world and he is lauded as "father of modern mass spectrometry". In 1919, F. W. Aston investigated more than 50 nonradioactive elements using mass spectrometry and proved the loss of atomic mass and the existence of isotopes for the first time. He won the Nobel Prize in Chemistry in 1922 because of this important finding [107]. Since then, mass spectrometry has gradually become a popular analytical tool. Over the past century, a variety of new technologies of mass spectrometry keeps emerging one after another. Every leap in technical development of mass spectrometry brings breakthroughs in many research fields. Take the development of ionization technology as an example. The early mass spectrometry ionization technology mainly includes electron ionization (EI) and chemical ionization (CI). These ionization techniques are only applicable to the detection of volatile substances. In the early 1980s, the development of plasma desorption (PD) [108] and fast atomization (FAB) [109] technology led to the application of mass spectrometry to polypeptides and protein molecules below a molecular weight of 10,000 u gradually. In the late 1980s, electrospray ionization (ESI) [110] and matrix-assisted laser desorption ionization (MALDI) [111] were developed, and these two important soft ionization techniques greatly extend the detection range of

molecular weight and significantly promote the development of proteomics and metabolomics. J. B. Fenn and K. TanaKa obtained the 2002 Nobel Prize in Chemistry for the development of these two mass spectrometry methods for studying biological macromolecule. As one of the important tools for modern instrumental analysis, mass spectrometry has penetrated into various disciplines and has been widely used in various fields such as chemistry, chemical industry, environment, energy, medicine, criminal science and technology, life sciences, materials science.

1.2.1 Introduction to Electrospray Ionization Mass Spectrometry

The electrospray ionization (ESI) technology directly ionizes the species in solvent into gas-phase ions which could be detected by mass spectrometry. This kind of method is called electrospray ionization mass spectrometry (ESI-MS) [110]. ESI-MS has gradually become an important tool for mechanistic study of organic reaction, especially reactions involving organometallic compounds. The ESI technology provides a very simple way to transfer organometallic complex from the solution to gas phase, especially when the complex of interest exists as ions in solution [112]. ESI-MS has been extensively applied in the detection of transient ionic intermediates to provide clues for the reaction mechanism [113–115].

Using ESI-MS to study reaction mechanism has several advantages: (1) ESI is a soft ionization method which enables the transfer of the intact ionized complex from solution into the gas phase directly. An important and controversial issue regarding the ionization process is whether the structure of the detected ion in the gas phase is the same as in the solution? There are many work in literature which have proved that the ion structure detected by ESI-MS is consistent with the ion structure in solution phase observed by NMR or electrochemistry tools [112, 116, 117]; (2) with ESI-MS, a specific ion of interest could be chose based on mass-to-charge ratio and analyzed separately, thus avoiding the interference of solvent and other compounds in the solution; (3) the critical intermediates generated during the catalytic process are usually unstable and only exist transiently in solution. When transferring them (or their precursor complexes) into gas phase, these intermediates become relatively stable under the high vacuum condition in mass spectrometer and thus provides a promising approach to study their reactivities by directly colliding with reactants (i.e., ion–molecule reactions); (4) ESI-MS provides an important complementary technique for NMR since it can detect paramagnetic compounds; (5) ESI-MS is a highly sensitive analytical tool which can detect ionic intermediates in very low concentration. In conclusion, ESI-MS has the advantages of high sensitivity and fast analysis speed and it can offer structural information of intermediate, which renders ESI-MS to be an important and useful tool in mechanistic studies.

1.2.2   Introduction to Ion Mobility Mass Spectrometry

Mass spectrometry separates ions based on their mass-to-charge ratio, thus mass spectrometry cannot distinguish ions with same values of m/z. Ion mobility spectrometry (IMS), also known as ion mobility spectroscopy, is an analytical technique used to separate ions according to their mobility in the drift region formed by the electric field and the drift gas. The ions with different sizes and shapes have different mobility and could be separated by IMS. The IMS technique was first developed in the middle of the twentieth century and widely applied in gas analysis, detection of explosive complexes, drug testing and environmental monitoring, and other fields because of its good detection limit, real-time detection capabilities, and diversified analytical abilities. However, the research about IMS has been gradually reduced since the late 1970s because IMS cannot provide the mass of ions due to its low resolution. In the late 1980s, the development and application of soft ionization techniques such as ESI and MALDI enabled the intact compounds to enter the gas phase and greatly expanded the detection range of biological macromolecules. People began to realize the importance of identifying the structure of chemical compounds and bio-macromolecule. At this time, the special advantages of IMS in separating isomers and providing structural information started to attract attention. Since then, a variety of instruments coupling IMS and MS (IM-MS) have been developed.

Ion mobility mass spectrometry (IM-MS) is a new type of multidimensional separation mass spectrometry coupling ion mobility spectroscopy (IMS) with mass spectrometry. It not only provides the mass-to-charge ratio and intensity of detected ions, but also offers their drift time which can be converted to structural information. The combination of structural information revealed by IMS technology and the mass spectrometry data provides plenty of information which cannot be obtained by other mass spectrometry, therefore greatly enriches the application of mass spectrometry. In addition, the introduction of IMS enhances the separation abilities of MS since ions can be distinguished by their shape in IM-MS. It is especially useful to isolate the isomers of complexes with same m/z which are not able to be differentiated by conventional mass spectrometry.

IM-MS technology has been successfully applied to the structural studies of various macromolecular protein complexes [118]. The Robinson group has made a lot of outstanding work on the structural studies of protein complexes using combined ion mobility mass spectrometry and molecular dynamics simulations. They have studied the quaternary structure of the Tap protein complex [119], the conformational changes of membrane protein during its binding with lipids [120] and conformational changes in ATPase [121], etc. The IM-MS method has also been successfully used to study multimers. The Bowers group from the University of California, Santa Barbara, used ion mobility mass spectrometry and molecular dynamics simulations to study the structure of oligomers and oligomerization

mechanism of Aβ42 and Aβ40 which provides important information for possible toxic species and oligomerization pathways for amyloid [122–127]. IM-MS can be also used in large-scale proteomics and metabolomics when combined with ultra-high performance liquid chromatography. In addition to its application in macro-molecular studies, IM-MS is also a powerful tool for mechanistic study of organic reactions. Schröder and Roithová have conducted a series of mechanistic studies on organic reactions using ion mobility mass spectrometry [128–133], demonstrating the outstanding advantages of ion mobility mass spectrometry in distinguishing between different conformers and isomers.

1.2.2.1 The Basic Principle of Ion Mobility Mass Spectrometry (IM-MS)

The basic principle of IM-MS is that the ionized species enter into a drift cell filled with buffer gas and they collide with the buffer gas continually, ions with different sizes and shapes have different mobility and moves with different speeds, therefore they across the drift cell with different drift time and thus are separated. The drift time is related to the rotationally averaged collision cross section.

In the conventional drift tube with a uniform electrostatic field (E), the average drift velocity (V_d) of an ion in a drift gas is related to its mobility (K) and the electric field strength (E): $V_d = K \times E = L/t_D$, where L is the length of drift tube and t_D is the drift time. In practical applications, the ion mobility is usually converted to reduced ion mobility (K_0), that is, the mobility of ion at a temperature of 273 K and a pressure of 760 Torr: $K_0 = K \times (273/T) \times (P/760)$. T, P are the temperature of the drift tube and the pressure of the drift gas. K_0 reflects the characters of the ion itself, closely related to its size and shape. The size of an ion can be evaluated by the collision cross section, Ω. According to the Mason-Schamp equation, K has the following relationship with the collision cross section:

$$K = \left(\frac{3q}{16N}\right)\left(\frac{2\pi}{kT}\right)^{1/2}\left(\frac{m+M}{mM}\right)^{1/2}\left(\frac{1}{\Omega}\right).$$

By combining the above equations, then the correlations between collision cross section and drift time can be determined by the following equation:

$$\Omega = \frac{(18\pi)^{1/2}}{16}\frac{ze}{k_b T^{1/2}}\left(\frac{m+M}{mM}\right)^{1/2}\frac{t_D E}{L}\frac{760}{P}\frac{T}{273}\frac{1}{N}.$$

where z is the ion charge state, e is the elementary charge, k_b is Bolzmann constant, and N is the gas number density.

1.2.2.2   Introduction to the Instruments of IM-MS

Following the progress in ion mobility spectrometry and its successful coupling with mass spectrometry, a large amount of IM-MS instruments have been developed. Currently, there are mainly three types of ion mobility instrumentation which have been successfully coupled with mass spectrometers: drift-time ion mobility spectrometry (DTIMS), field-asymmetric waveform ion mobility spectrometry (FAIMS) and traveling wave ion mobility spectrometry (TWIMS) [134, 135].

DTIMS [136] is the simplest configuration of IM-MS instrumentation utilizing traditional 'drift-time' ion mobility spectrometry. As shown in Fig. 1.9a, the sample is ionized and introduced into the drift tube. The ions drift through the drift tube due to the electrostatic field, whilst collisions with buffer gas slow the ions' progress. Ions are thus separated based on their different motilities. DTMS is the only form of IM-MS in which the collision cross section of ions can be directly determined from drift time using Mason-Schamp equation. However, in DTIMS the ions are quickly slowed down due to the continual collision with drift gas, dramatically decreasing the duty cycle and leading to low analytical sensitivity. Many improvements have been made to achieve adequate separation. The basic working principle of FAIMS [137, 138] is depicted in Fig. 1.9b. In FAIMS, ions move across between a pair of electrodes. The lower electrode is maintained at ground potential while the upper electrode has an asymmetric waveform applied to it. Ions waves forward under the asymmetric electric field and the drift gas. Ions are separated due to the application of a high-frequency periodic asymmetric waveform, rather than DC voltage used in DTMS. FAIMS has a high analytical resolution, but the relationship between the measured drift time and its collision cross section is not as straight forward as that
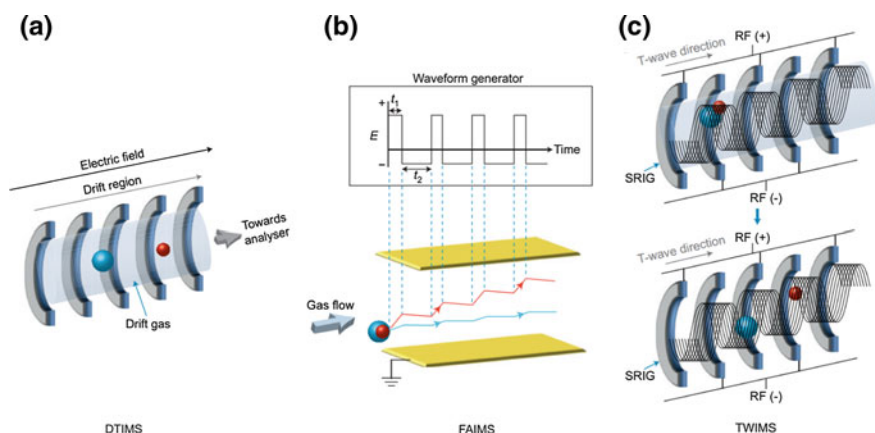
Fig. 1.9   The three conventional types of ion mobility instrumentation: **a** drift-time ion mobility spectrometry (DTIMS); **b** field-asymmetric waveform ion mobility spectrometry (FAIMS), and **c** traveling wave ion mobility spectrometry (TWIMS). Reprinted by permission from Macmillan Publishers Ltd: ref. [135], copyright 2014

found in the DTMS. Thus, FAIMS is mainly applied as a separation tool. TWIMS is a novel method to separate ions utilizing a traveling voltage wave. As shown in Fig. 1.9c, TWIMS [139] uses stacked ring ion guide. Two types of electric fields are applied in TWIMS: an RF field is applied to consecutive electrodes in the stacked ring ion guide, providing a potential well which keeps ions radially confined within the device; on the other hand, a series of transient DC voltages superimpose on top of the RF voltage to form a traveling wave which drives ions through the drift region. The generated traveling wave significantly improves the transmission efficiency of ions and thus leads to excellent separation power. In addition, the reverse RF voltage on the adjacent electrode confines ions in the ion guide, which can significantly reduce the ion loss, leading to good sensitivity and high analytic speed. But the drift time measured with TWIMS cannot be directly related to the collision cross section. In this case the conversion of drift time to collision cross section need calibration which will be discussed in detail in next section.

In 2006, Waters introduced the first commercial travelling wave mass spectrometry [140], i.e., SYNAPT. Figure 1.10 shows a schematic of SYNAPT [141, 142]. It is mainly composed of an ion source, a quadrupole mass analyzer, a traveling wave ion mobility analyzer, and an orthogonal acceleration TOF mass analyzers. The traveling wave ion mobility analyzer comprises three ion guides. The mobility separator is the central guide of three and is responsible for separating ions. There are two ion guides with similar structure but shorter length than the mobility separator: trap traveling wave ion guide (trap TWIG) and transfer traveling wave ion guide (transfer TWIG). The former guide collects and stores ions prior to injection into the separator and the latter one transfers the ions to the TOF. A special advantage of SYNAPT is that collision induce dissociation can be performed both
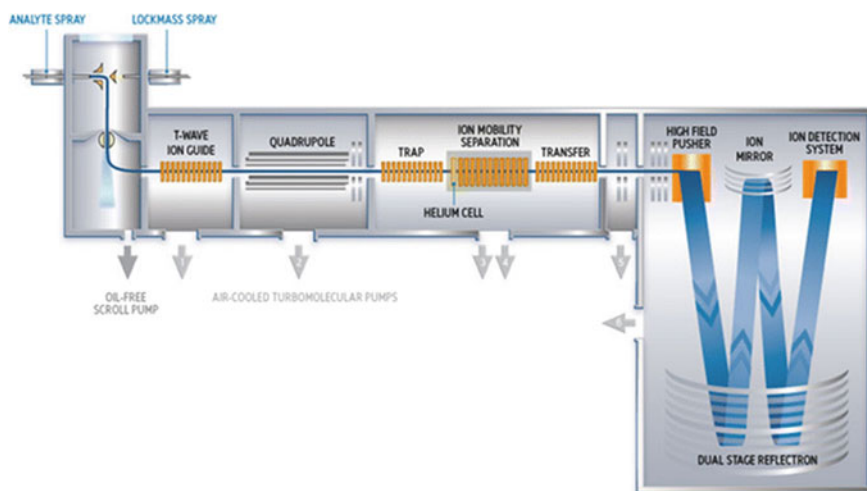
Fig. 1.10 Schematic of the SYNAPT G2-s HDMS mass spectrometer. Reprinted from ref. [142], with kind permission from Springer Science + Business Media

in the trap and transfer TWIG, i.e., before and after ions enter the mobility cell, therefore enables multiple dissociation patterns. The movement of ions in the mobility cell of TWIMS is complicated and the ions drift velocity depends upon many variables, including the height and velocity of the voltage 'wave' applied to propel ions, the drift gas, and the structure of ions.

The soft ionization technique, such as ESI and MALDI, generally produces molecular ion. The collision induced dissociation (CID) experiments are usually performed to get more structural information of the molecular ion. For SYNAPT, the trap and transfer traveling wave regions can be used independently or together as collision cells, with or without ion mobility separations. Multiple options for CID allow a unique and diverse range of experimental possibilities for improved and more complete structural characterization. Figure 1.11 depicts three possible types of CID experiments with ion mobility separation (i.e., HDMS mode). In Fig. 1.11a, the selected ion is dissociated upon the CID in trap cell, then the generated daughter ions are separated in the mobility cell and they arrive at the detector consecutively. Figure 1.11b shows a schematic of IMS-CID, in which ions with same m/z selected by quadrupole are separated in the ion mobility separator and they are dissociated into fragments upon CID performed in the transfer cell. The generated fragments

Fig. 1.11 A schematic diagram of CID experiments with ion mobility separation using SYNAPT

have the same drift time with their parent ions, thus providing structural information for the parent ions separately. This approach is especially useful to study isomers, complexes with different conformers and multimers of the same m/z. Multi-stage CID can also be realized with SYNAPT. As shown in Fig. 1.11c, the fragments generated from the first CID in trap cell were separated in the mobility separator and further fragmented upon the second CID in transfer cell. A particular advantage of introducing IMS to multi-stage CID is that the orthogonal separation afforded by IM separation significantly increases the number of detectable and identifiable components in complex mixtures by distinguishing ions of the same m/z.

1.2.2.3   Determination of Experimental and Theoretical CCS Values

Different from DTIMS in which the measured drift time is linearly related to the collision cross section area, in T-wave IMS system, the measured arrival time distribution cannot be directly converted to CCS by Mason-Schamp equation and CCS data is obtained by a calibration approach. In a nutshell, a calibration curve is established by measuring the drift time of ions with known CCS values (measured from conventional IM experiments) to obtain the correlation between the drift time and CCS, then the CCS value of unknown sample is determined by this correlation function. A general calibration process is described below:

1. Measure the drift time (t_D) of the ions of calibrant under exactly the same instrument conditions optimized for sample.
2. Calculate corrected drift time $t'_D = t_D - c\sqrt{(m/z)}/1000$, where c is the correction factor of the instrument.
3. Calculate the normalized cross section (Ω') using the published cross section data (Ω), reduced mass (μ) and charge state (z): $\Omega' = (\Omega \times \sqrt{\mu})/z$, where $\mu = M_{ion} \times m_{gas}/(M_{ion} + m_{gas})$.
4. Plot t'_D versus Ω' and fit a linear trendline of the form y = ax + b or power trendline of the form y = Ax^b to the data. The choice of trendline depends on the range of the calibration.
5. Convert corrected drift time t'_D of the sample to collision cross section using the following equations:
   For values obtained from a linear fit: T-wave CCS = $((at'_D + b)z)/\sqrt{\mu}$
   For values obtained from a power fit: T-wave CCS = $(t'_D)^b Az/\sqrt{\mu}$.

Several algorithms have been developed to calculate the theoretical CCS. Commonly used algorithms include projection approximation (PA) [143], exact hard sphere scattering (EHSS) [144] and trajectory method (TM) [145]. The PA method calculates the orientationally averaged geometric cross section by averaging

the geometric cross section over all possible collision geometries. PA method ignores the interaction between ions and drift gas, thus it generally underestimates the CCS and it is accurate only for small polyatomic ions (<1500 Da) with totally convex surfaces. The EHSS method calculates the orientationally averaged hard-sphere CCS by determining the scattering angles between the incoming buffer gas atom trajectory and the departing buffer gas atom trajectory. It takes into account multiple scattering but neglects the long-range interactions, therefore overestimating CCS values. The TM method calculates the scattering angle via a more realistic potential that accounts for the long-range interactions and multiple collisions between the drift gas and the polyatomic ion. Among these three methods, TM method is regarded as the most reliable and accurate method to estimate the theoretical CCS value, but this method is most time-consuming. The Bowers group from the University of California, Santa Barbara developed the Sigma program [146] which uses the PA method. Recently, this group developed projection superposition approximation method (PSA) [147] which is based on the PA concept but improved for calculating larger molecules. The Jarrold group from the University of Indiana developed the MOBCAL software [148] which incorporates the three algorithms introduced above. Currently MOBCAL is the most widely applied software for calculating theoretical CCS values.

Analysis of ion mobility experiment is usually combined with computational modeling approaches to assist interpreting the experimental data. The possible structures of the target molecule are generated from computational modeling (with DFT or MD method). Theoretical CCS values of energy-minimized structures can be obtained by submitting their corresponding coordinates to the program introduced above. Then these theoretical CCS values are compared with the experimental CCS values to aid in the structural assignment, providing detailed structural information at the atomic level.

1.2.3 Applications of ESI-MS and IM-MS in Mechanistic Studies

ESI-MS provides an important tool for mechanistic studies on organic reactions, especially reactions involving organometallic complexes. As discussed in Sect. 1.2.1, due to the many advantages of ESI-MS in mechanistic studies, it has been extensively used in detecting the transient ionic intermediates, providing clues for mechanistic study or providing supports for proposed mechanism [113–115]. Mechanistic studies by ESI-MS have been reported for a broad range of organic reactions, such as Bayes-Hiller reaction, C–H bond or N–H bond activation reaction, Diels–Alder reaction, Crubbs olefin metathesis reaction, Heck reaction, methylation reaction, Suzuki reaction, Stille reaction, Wittig reaction, and many

other reactions. Two recent examples are presented to illustrate the applications of ESI-MS in mechanistic studies.

As shown in Fig. 1.12, according to the results of deuterium labeling experiments, two possible pathways were proposed for the Rh-catalyzed coupling reaction between acetylene and carbonyl compounds [149]. In pathway I, acetylene undergoes oxidative dimerization to form a cationic rhodacyclopentadiene (**103**) and carbonyl inserts into **103** to afford intermediate **105**, then Brønsted acid-assisted hydrogenlysis through intermediates **106** and **107** generates the final product. The difference between pathway I and II lies in the sequence of the first two steps. In pathway II, the oxidative coupling between the acetylene and carbonyl occurs first to form intermediate **104**, then the second acetylene inserts into **104** to form intermediate **105**. ESI-MS experiments were carried out to understand the reaction takes place via which pathway. ESI-MS experiments detected intermediates **102**, **103**, **105** and **106**, while ions corresponding to intermediate **104** were not detected. In addition, the complex **105** was found to dissociate to an ion corresponding to intermediate **103** in the CID experiment, indicating a retrocarbonyl insertion process. Therefore, the ESI-MS experiment provides experimental supports for pathway I. Computational results suggest that the reaction barrier for the coupling reaction between acetylene and carbonyl compound is higher than that for the dimerization of acetylene by 7 kcal/mol, which is in agreement with the ESI-MS experiment. Computational studies provide more detailed information about the reaction mechanism: the hydrogenolysis step is the rate-determining step and Ph_3CCO_2H acts as Brønsted acid to assist the Rh–O bond cleavage and acts as ligand to promote the cleavage of H–H bond.

$$
\underset{\textbf{99}}{RO\overset{\displaystyle O}{\underset{\displaystyle O}{\|}}\!\!\overset{}{\diagup}\!\!CH_3} + \underset{\textbf{100}}{2\,HC\!\equiv\!CH} \xrightarrow[\substack{Ph_3CCO_2H \\ Na_2SO_4,\ D_2,\ DCE}]{[Rh(cod)_2]BARF} \underset{\textbf{101}}{RO\overset{\displaystyle O}{\|}\!\!\diagup\!\!\underset{HO\ \ CH_3}{}\diagdown\!\!\diagup\!\!D} \qquad (1.23)
$$
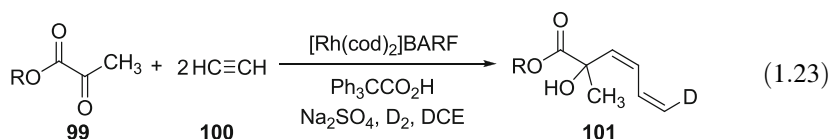
Figure 1.13 shows the Rh-catalyzed coupling of terminal alkynes with carboxylic acids and proposed mechanisms for this reaction [150]. The originally proposed mechanism involves the insertion of Rh into the O–H bond of benzoic acid (TS**111**). However, no ionic species involving Rh–H or benzoate were detected by MS. Instead, the ion corresponding to complex **112** was observed by MS and was also identified by X-ray and NMR experiments. The complex **112** affords product **110** in a further CID experiment. DFT calculations demonstrate that a protonation process via TS**112** is more favorable than the previously proposed TS**111**. The protonation process is followed by β-hydride elimination, leading to an allene complex which affords the final product **110**.
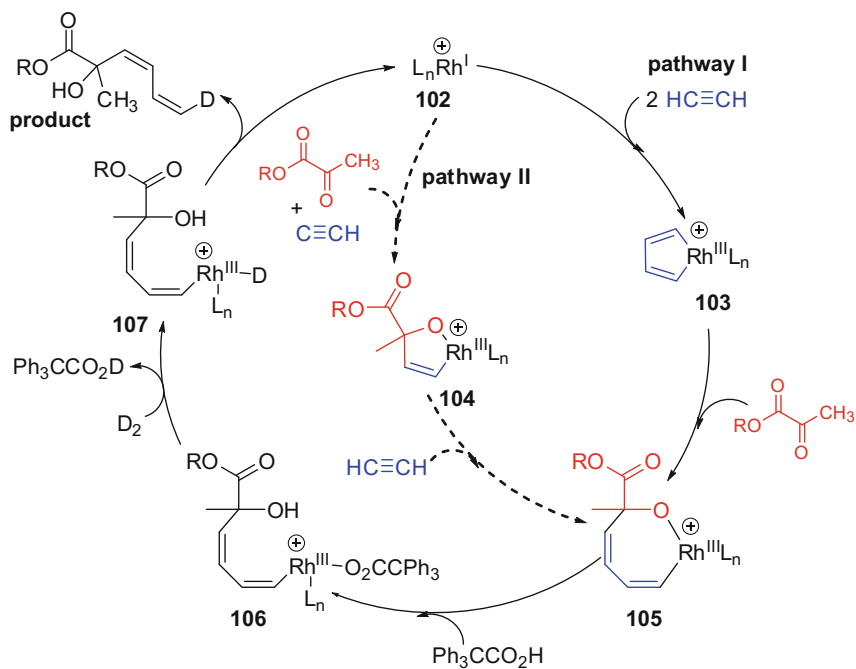
Fig. 1.12 Plausible reaction pathways I and II for the coupling reaction 1.23. Intermediates **102**, **103**, **105** and **106** were detected by ESI-MS experiments
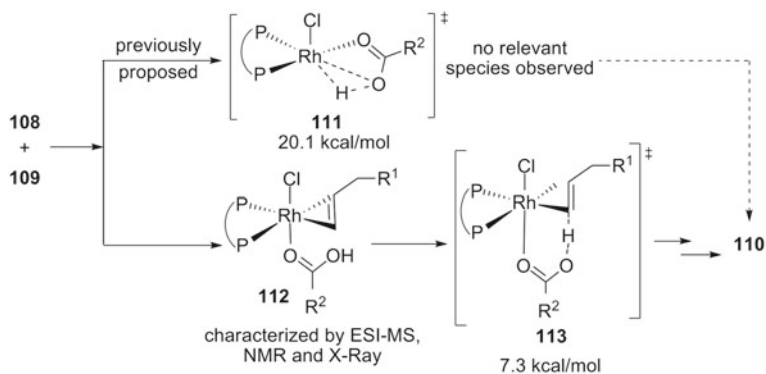
Fig. 1.13 Proposed mechanism for Rh-catalyzed coupling of terminal alkynes with carboxylic acids and related computational results

(a)

(b)

(c)
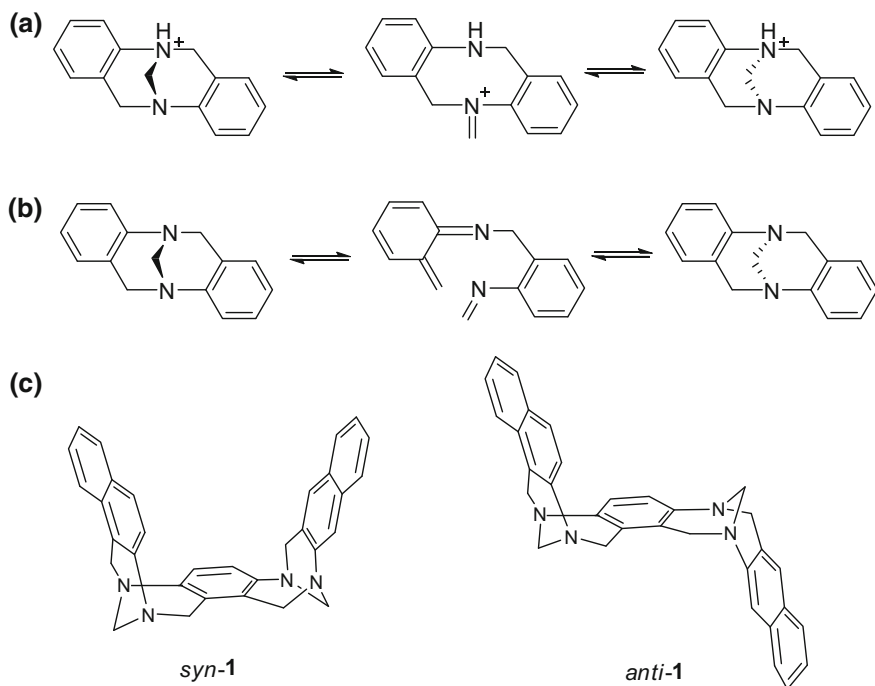
syn-**1**   *anti*-**1**

Fig. 1.14 Proposed mechanisms for the pseudoepimerization of Tröger base: **a** proton-catalyzed ring opening mechanism and **b** retro-Diels–Alder mechanism; **c** Bis-Tröger bases *syn*-**1** and *anti*-**1** studied in ref. [128]

$$\text{(1.24)}$$
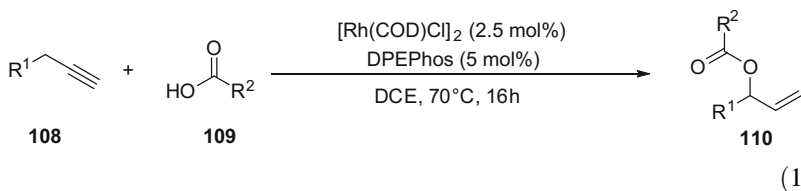
Combining the IMS and MS techniques, IM-MS not only provides the mass-to-charge ration but also offers structural and conformational information of ions. On the other hand, the additional dimension of separation introduced by IMS significantly improves the separation power of MS. IM-MS has a particular advantage over the conventional MS in distinguishing isomers or complexes with same mass-to-charge ratio. IM-MS has been widely applied in structural analysis of macromolecules. It also has been used in mechanistic studies of organic reactions recently. The Schröder and Roithová group conducted mechanistic studies on a series of organic reactions using IM-MS [128, 133, 151–153] which demonstrated
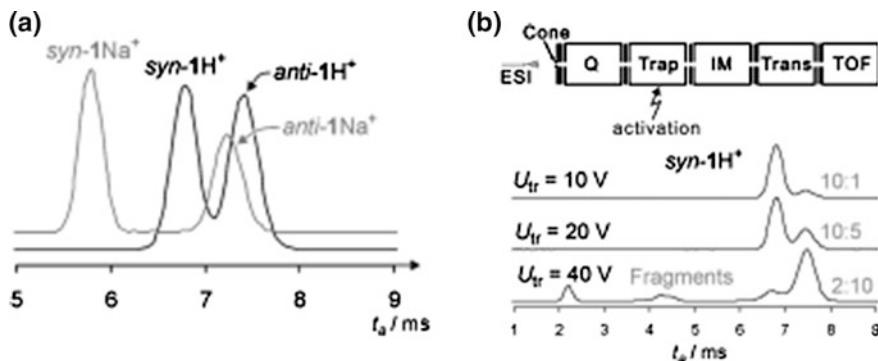
Fig. 1.15 a Separation of *syn*-**1** and *anti*-**1** complexes using IM-MS and **b** isomerization of *syn*-**1**H$^+$ to *anti*-**1**H$^+$ in CID experiment. Reproduced from ref. [128] by permission of John Wiley & Sons Ltd

its outstanding advantage in differentiating isomers and conformers. One example from their group is presented below.

Tröger base has wide applications in chemistry due to its chirality and rigid skeleton. Its chirality is resulted from the presence of two bridgehead stereogenic nitrogen atoms in its structure. As depicted in Fig. 1.14, the chirality of Tröger base can be inverted via pseudoepimerization. However, as a fundamental question in the chemistry of Tröger base, the mechanism of the pseudoepimerization remains unclear. It may occur via a proton-catalyzed ring opening mechanism (a) or a retro-Diels–Alder (RDA) pathway (b). To understand the mechanism, The Schröder group investigated the bis-Tröger base *syn*-**1** and *anti*-**1** (Fig. 1.14c) which are diastereoisomers with different shapes using IM-MS [128]. The mixture of these diastereoisomers was well differentiated by IM-MS with good resolution (Fig. 1.15a). More importantly, they observed the isomerization of the protonated complex *syn*-**1**H$^+$ to *anti*-**1**H$^+$ in a further CID experiment (Fig. 1.15b). However, no isomerization of the sodium adduct *syn*-**1**Na$^+$ was detected. This observation precludes the retro-Diels–Alder (RDA) pathway since both *syn*-**1**H$^+$ and *syn*-**1**Na$^+$ will be able to form anti-conformers via an RDA mechanism. Therefore IM-MS experiments indicate the importance of proton in pseudoepimerization and provide experimental supports for proton-catalyzed ring opening mechanism.

1.3 A Brief Introduction to Computational Chemistry

Computational chemistry is an interdisciplinary subject. It utilises the methods of theoretical chemistry which are efficiently incorporated in computational program to simulate or calculate the structures or properties of molecules, gases, liquids and solids, assisting in solving problems in chemistry, material, biochemistry, and other

fields. Computational chemistry directly deals with atoms and molecules, and provides information which is difficult to be obtained by experimental methods, offering explains and guidance for experiments. Computational chemistry has become an indispensable tool and been widely applied in various fields.

1.3.1 Quantum Mechanical Methods

By the late nineteenth century, the laws of physics were based on classical mechanics, while it was challenged by the phenomena of black body radiation and photoelectric effect. In 1900, Max Planck offered a proposal that the electromagnetic energy could be emitted only in a quantized form which successfully explained the black body radiation. Later Einstein introduced this quantization concept to the radiation field and successfully accounted for the photoelectric effect. In 1924, de Broglie pointed out that all the physical particles have wave–particle duality and their energies could be evaluated with $\varepsilon = h\nu$, which extended the quantization concept to all objects. In 1926, Schrödinger proposed that a physical system is described entirely by a wave function Ψ and deduced the famous Schrödinger equation [154], also known as the wave equation. The time-independent Schrödinger equation is $\hat{H}\Psi = E\Psi$, where $\hat{H}$ is the Hamilton operator which acts on the wave function and returns the system energy, E, as an eigenvalue. The typical form of Hamilton operator involves five contributions to the total energy of the system: the kinetic energy of the electrons, the kinetic energy of nuclei, the attraction of the electrons to the nuclei, and the interelectronic and internuclear repulsions. The general many-particle Hamiltonian describing a system of N electrons and M nuclei is:

$$\hat{H} = -\sum_{i=1}^{N} \frac{1}{2} \nabla_i^2 - \sum_{A=1}^{M} \frac{1}{2 M_A} \nabla_A^2 - \sum_{i=1}^{N} \sum_{A=1}^{M} \frac{Z_A}{r_{iA}} + \sum_{i=1}^{N} \sum_{j \geq i}^{N} \frac{1}{r_{ij}} + \sum_{A=1}^{M} \sum_{B \geq A}^{M} \frac{Z_A Z_B}{R_{AB}}$$

where all the physical quantities (mass, charge, distance) are in atomic units, i and j run over electrons, A and B run over nuclei, M_A and Z_A are mass and nuclear charge, respectively, R_{AB} is the distance between particles A and B, and ∇^2 is the Laplacian operator.

   Schrödinger equation is the fundament of quantum mechanics. Theoretically, if one has the molecular wave function of a molecule, one can obtain any desired information about this molecule by solving the Schrödinger equation. All methods based on quantum mechanics and used by solving the Schrödinger equation are called ab initio or the first principle methods. However, accurate wave functions for many-particle systems are extremely difficult to express and the computational complexity for solving the Schrödinger equation increases exponentially as the system increases. The accurate solution of Schrödinger equation is only limited to extremely simple molecules such as H_2.

Approximations are made to simplify and solve the Schrödinger equation of a complex system. One essential approximation is the Born–Oppenheimer approximation [154] which ignores the kinetic energy of nuclei since nuclei move orders of magnitude slower than the electron and considers the electrons move in a field of fixed nuclear potential. Applying this approximation, the Schrödinger equation is simplified as

$$\hat{H}_{\text{elec}}\,\Psi_{\text{elec}} = \left(-\sum_{i=1}^{N}\frac{1}{2}\nabla_i^2 - \sum_{i=1}^{N}\sum_{A=1}^{M}\frac{Z_A}{R_{iA}} + \sum_{i=1}^{N}\sum_{j\geq i}^{N}\frac{1}{r_{ij}}\right)\Psi_{\text{elec}} = E_{\text{elec}}\,\Psi_{\text{elec}}$$

.

The Born–Oppenheimer approximation is the central law of quantum chemistry and is the basis of almost all ab initio methods.

Hartree–Fock (HF) method [155] is a classic ab initio method and is based on 'mean field' approximation. For a system containing N electrons, its wave function is expressed as the combination of N wave functions of spin orbital for a single electron. Every single electron experiences a mean field formed by all of the other electrons ('mean field' approximation). With this approximation, the wave function of a multi-electron system can be expressed by the wave function of a single electron:

$$|\Psi_0\rangle = |\chi_1\,\chi_2\cdots\chi_a\,\chi_b\cdots\chi_N\rangle.$$

Therefore, the N-electron problem is reduced to N one-electron problem. The one-electron Hamiltonian can be rewritten as the Fock operator,

$$f(i) = h(i) + v^{\text{HF}}(i) = -\frac{1}{2}\nabla_i^2 - \sum_{A}\frac{Z_A}{r_{iA}} + \sum_{b}[J_b(i) - K_b(i)],$$

where $h(i)$ involves the terms only determined by electron i (and the fixed nuclei), $v^{\text{HF}}(i)$ includes the electron–electron interactions in an average potential. $J_b(i)$ and $K_b(i)$ are the coulomb and exchange operators respectively. With the Fock operator, the Hartree–Fock equation can be constructed as

$$f(i)\chi_a(i) = \varepsilon_a\chi_a(i).$$

To solve the Hartree–Fock equation, we first need to choose a set of spin orbital wave function χ_a which is usually extended to a linear combination of a series of basis functions (or basis set) ϕ_i, i.e., $\chi_a = \sum_i C_{ia}\phi_i$. Several types of basis functions including Slater type obitals (STOs), Gaussian type obitals (GTOs), and contract Gaussian type orbitals (CGTOs) have been developed. Generally, larger number of well chosen basis functions yields more accurate results, but it is more expensive and time-consuming. With an infinite basis set, the solution of the Hartree–Fock

equation will lead to the accuracy limit of this method, i.e., HF limit. However, performing this kind of calculation is almost never a practical possibility.

HF method always gets energies higher than the exact ground state energy since it only describes the coulomb repulsion and exchange interaction between electrons. The error between HF energy and the exact ground state energy is defined as correlation energy. Although the magnitude of correlation energy is only 1% of the total energy, it is comparable to the energy of a typical chemical reaction, leading to large errors in solving chemical problems. A series of post-HF methods, including configuration interaction (CI), many-body perturbation theory (MBPT), coupled cluster (CC), and so forth, have been developed in order to approach chemical accuracy. All these methods are based on HF and make corrections for the correlation energy. The introduction to these methods can be found elsewhere and will not be discussed here.

Although the post-HF methods afford more accurate results by involving correlation energy, they generally require more computation resource and are hard to be applied in large systems. Density functional theory [156], DFT, a totally different approach was developed to solve quantum mechanical problems. The fundament of DFT is Hohenberg-Kohn theorems developed by Hohenberg and Kohn in 1964 which proposes that for molecule in nondegenerate state its electron density ρ uniquely determines the Hamiltonian, and therefore its energy, wave function and other properties. The energy of a system is described by Kohn–Sham equation [157]:

$$E\left[\rho\left(\vec{r}\right)\right] = \sum_{i=1}^{N} \int \varphi_i\left(\vec{r}\right) \left(-\frac{\nabla^2}{2}\right) \varphi_i\left(\vec{r}\right) d\vec{r} + \frac{1}{2} \iint \frac{\rho\left(\vec{r}_1\right)\rho\left(\vec{r}_2\right)}{r_{12}} d\vec{r}_1 \, d\vec{r}_2$$
$$- \sum_{A=1}^{M} \int \frac{Z_A}{r_A} \rho\left(\vec{r}\right) d\vec{r} + E_{XC}[\rho(r)].$$

The energy E involves the kinetic energy of the electrons, interelectronic coulomb repulsion, the attraction of the electrons to the nuclei and exchange-correlation energy. In KS approach, the exchange-correlation potential is completely unknown. However, the exchange-correlation is of great importance for describing a system. Thus some approximations are made to describe the exchange-correlation interaction. Various DFT methods with different exchange-correlation potential have been developed, including local density approximation (LDA), generalized gradient approximation (GGA), hybrid functionals, and so forth. For example, the commonly used functional, B3LPY, is a hybrid functional which combines the Becke type GGA exchange functional [158], Hartree–Fock exchange functional and LYP type GGA correlation functional [159].

DFT takes the electronic correlation effect into account, leading to a higher accuracy than HF methods. For N-electrons system, wave function methods need to deal with 3N variables while DFT methods only need to handle N variables. Thus, the computational efficiency of DFT methods is much higher than HF and post-HF

method. The development of DFT dramatically propels the application of quantum chemistry and achieves tremendous success.

1.3.2   Other Computational Methods

Another class of computational methods is molecular mechanics (MM). Differs from the quantum mechanics, MM models molecular system based on classical mechanics and interactions are described by force field (FF). Popular force fields include CHARMM [160], Amber [161], OPLS [162], Gromos [163], and so on. Force field used in MM method is constructed with a series of parameters which are derived from experimental data. MM method is generally less accurate than the quantum mechanical methods, but its computational speed is much higher which allows the application of MM in macromolecular system. It has been broadly used in biochemistry, biophysics, and material science. The use of molecular mechanics in molecular dynamics enables it to model the dynamics and predict the trajectory of a molecular system.

Hybrid quantum mechanics/molecular mechanics (QM/MM) method [164–166] is a computational method which combines the strengths of QM and MM methods, i.e., the high computational accuracy of QM and high computational speed of MM method. For example, when modeling the enzyme-catalyzed reactions with QM/MM method, the active site of enzyme and substrates are treated with QM method to model the reaction process with high accuracy and the other parts of the system is described by MM to include the effects of environment with high computational efficiency. Extensive applications in complex systems have been reported with QM/MM method, especially in enzyme systems.

1.3.3   Applications of Computational Chemistry in Mechanistic Studies on Organic Reactions

Traditional methods, such as kinetic studies, isotope labeling, capturing and identifying intermediate and other experimental approaches, play an important role in understanding the reaction mechanism and propels the development of organic chemistry. Despite the versatile applications of these methods, they show some obvious deficiencies in regard to mechanistic studies, including (1) it is hard for traditional experimental approaches to provide a detailed reaction pathway for a multi-step reaction, (2) generally it is difficult to obtain the structural information of intermediates involved in catalytic cycle by experimental tools due to the high reactivity and transient property of intermediates, and (3) for the organic reactions with multiple plausible reaction pathways, traditional approaches cannot decide which reaction pathway is more favorable in energy.

By taking advantages of the incredible progress in speed and capacities of computers and the development of computational programs, computational chemistry has become a powerful and popular tool and has played an increasing role in mechanistic studies on organic reactions.

Computational chemistry has a unique advantage in providing detailed information at atomic level for organic reactions by calculating structures and energies of reactants, intermediates, transition states, and products, as well as potential energy surface of various possible reaction pathways. Combined with experiments, computational chemistry assists in understanding reaction mechanism which facilitates reaction optimization and new reaction or catalyst design.

Nowadays, computational chemistry has been frequently used in both computational and experimental groups. A growing number of publications in chemistry involve computations [167–172]. Our recently published perspective has demonstrated the successful applications of combined computational chemistry and experiments in establishing the mechanisms of chemical reactions [167]. Additionally, the forthcoming chapters will also showcase the applications of computational chemistry in mechanistic studies. Thus detailed introduction is skipped here and following part mainly provides some suggestions for conducting computational studies on the reaction mechanism.

(1) Build a reasonable model for the studied system. In order to reduce the computational cost, simplifications of the studied system are usually necessary, especially for large systems. While in the meanwhile, the simplified model must be able to represent the real system to ensure the accuracy. Thus, constructing an appropriate model is a critical step and a prerequisite for obtaining reliable computational results. Model construction depends on the characters of the reaction system. For example, for the system which is not sensitive to steric effects, the bulky groups can be replaced by smaller substituents to reduce the size. However, for the reaction in which the steric effect plays an important role (e.g., in some asymmetric reaction, the steric effect of ligand or substrate is critical to the stereoselectivity), the bulky substituents have to be included in the model. In organoctalysis, the intermolecular interactions between substrate and ligands (e.g., hydrogen bonding interactions) are usually essential, and thus groups involved in these critical interactions have to be included in the model.

(2) Select an appropriate and reliable computational method. Before performing computational studies, one should choose a reliable method and an appropriate basis set according to the chemical problem to be solved and evaluate the performance of the chosen method. DFT is a popular computational method used for studying organic reactions. Among them, B3LYP/6-31G(d) [173] has been used as a general computational method for a long time and applied in extensive computational works of organic reactions. However, several cases in which B3LYP fails utterly have been reported [174, 175]. In particular, B3LYP has rather poor performance in describing the medium to long-range dispersion which plays a pivotal role in many molecular systems and chemical reactions. Considerable efforts have been invested to solve this problem. One solution is to

incorporate the empirical dispersion correction into the existing functionals, e.g., DFT-D method developed by the Grimme group [176, 177]. Another solution is to develop novel functionals which is parameterized to include dispersion interactions, e.g., M06 suite of density functionals (M06, M06L, M06-2X, M06-HF …) developed by the Truhlar group [178–180]. Here is an example to illustrate the importance of selecting an appropriate method: when calculating the structure of triphenylphosphine ligand coordinated Pd complex, B3LYP method predicts the $Pd(PPh_3)_2$ complex is most stable and underestimates the binding energy by more than 30 kcal/mol. B3LYP-D and M06 method predict $Pd(PPh_3)_4$ is the most stable complex, which is in accord with experiment [181].

(3) Assess and interpret obtained computational results carefully. Computations only generate data, one should evaluate the results and consider whether the computational errors affect the conclusions or not. Generally, the comparisons between reaction pathways via the same mechanism (e.g., comparison between TSs of *R*- and *S*-conformers, comparisons between reactions of substrates bearing different substituents) are relatively reliable due to cancellation of errors. But one should be careful to compare different reaction mechanisms which may contain different numbers of molecules or have different charge states. In addition, combining the experimental observations and computational results to understand the reaction mechanism is extremely important since it provides essential information to support or disprove the proposed mechanism (s). At last, as the famous theoretical chemist, Charles Coulson, proposed "Give us insight, not numbers", we should not stay on the surface, but should explore the chemistry behind the data when analyzing the computational results.

References

1. Wender PA, Verma VA, Paxton TJ, Pillow TH (2008) Acc Chem Res 41:40
2. Trost BM (1995) Angew Chem Int Ed Engl 34:259
3. Trost BM (1991) Science 254:1471
4. Miyaura N, Suzuki A (1995) Chem Rev 95:2457
5. Milstein D, Stille JK (1978) J Am Chem Soc 100:3636
6. Heck RF (1979) Acc Chem Res 12:146
7. Dieck HA, Heck FR (1975) J Organomet Chem 93:259
8. King AO, Okukado N, Negishi E-I (1977) J Chem Soc, Chem Commun: 683
9. http://www.nobelprize.org/nobel_prizes/chemistry/laureates/2010/
10. Bergman RG (2007) Nature 446:391
11. Davies HML, Manning JR (2008) Nature 451:417
12. Chen X, Engle KM, Wang D-H, Yu J-Q (2009) Angew Chem Int Ed 48:5094
13. Daugulis O, Do H-Q, Shabashov D (2009) Acc Chem Res 42:1074
14. Lyons TW, Sanford MS (2010) Chem Rev 110:1147
15. Davies HML, Du Bois J, Yu J-Q (2011) Chem Soc Rev 40:1855
16. Yeung CS, Dong VM (2011) Chem Rev 111:1215
17. Kuhl N, Hopkinson MN, Wencel-Delord J, Glorius F (2012) Angew Chem Int Ed 51:10236
18. Lafrance M, Rowley CN, Woo TK, Fagnou K (2006) J Am Chem Soc 128:8754
19. Lafrance M, Fagnou K (2006) J Am Chem Soc 128:16496

20. Beck EM, Grimster NP, Hatley R, Gaunt MJ (2006) J Am Chem Soc 128:2528
21. Kleiman JP, Dubeck M (1963) J Am Chem Soc 85:1544
22. Wu X, Zhao Y, Ge H (2015) Chem Sci 6:5978
23. Zhang Q, Yin X-S, Chen K, Zhang S-Q, Shi B-F (2015) J Am Chem Soc 137:8219
24. Yang Y, Liu P (2015) ACS Catal. 5:2944
25. Stephens DE, Larionov OV (2015) Tetrahedron 71:8683
26. Colby DA, Tsai AS, Bergman RG, Ellman JA (2011) Acc Chem Res 45:814
27. DiPoto MC, Hughes RP, Wu J (2015) J Am Chem Soc 137:14861
28. Giri R, Yu J-Q (2008) J Am Chem Soc 130:14082
29. Giri R, Maugel N, Li J-J, Wang D-H, Breazzano SP, Saunders LB, Yu J-Q (2007) J Am
    Chem Soc 129:3510
30. Li S, Cai L, Ji H, Yang L, Li G (2016) Nat Commun 7
31. Lu Y, Wang D-H, Engle KM, Yu J-Q (2010) J Am Chem Soc 132:5916
32. Wasa M, Yu J-Q (2010) Tetrahedron 66:4811
33. Xiao K-J, Chu L, Yu J-Q (2016) Angew Chem Int Ed 55:2856
34. Funes-Ardoiz I, Maseras F (2016) Angew Chem Int Ed 55:2764
35. Keary Engle (2016) M. Pure Appl Chem 88:119
36. Shi Z, Li B, Wan X, Cheng J, Fang Z, Cao B, Qin C, Wang Y (2007) Angew Chem Int Ed
    46:5554
37. Yang S, Li B, Wan X, Shi Z (2007) J Am Chem Soc 129:6066
38. Giri R, Lam JK, Yu J-Q (2009) J Am Chem Soc 132:686
39. Boele MDK, van Strijdonck GPF, de Vries AHM, Kamer PCJ, de Vries JG, van
    Leeuwen PWNM (2002) J Am Chem Soc 124:1586
40. He G, Wang B, Nack WA, Chen G (2016) Acc Chem Res 49:635
41. Zaitsev VG, Shabashov D, Daugulis O (2005) J Am Chem Soc 127:13154
42. Rouquet G, Chatani N (2013) Angew Chem Int Ed 52:11726
43. Zhang F, Spring DR (2014) Chem Soc Rev 43:6906
44. Rousseau G, Breit B (2011) Angew Chem Int Ed 50:2450
45. Zhang Y-H, Shi B-F, Yu J-Q (2009) J Am Chem Soc 131:5072
46. Zhang S, Shi L, Ding Y (2011) J Am Chem Soc 133:20218
47. Phipps RJ, Gaunt MJ (2009) Science 323:1593
48. Daugulis O, Zaitsev VG (2005) Angew Chem Int Ed 44:4046
49. Chen B, Hou X-L, Li Y-X, Wu Y-D (2011) J Am Chem Soc 133:7668
50. Saidi O, Marafie J, Ledger AEW, Liu PM, Mahon MF, Kociok-Köhn G, Whittlesey MK,
    Frost CG (2011) J Am Chem Soc 133:19298
51. Liu DJ, Yu HZ, Fu Y (2013) Acta Chim Sin 71:1385
52. Hofmann N, Ackermann L (2013) J Am Chem Soc 135:5877
53. Juliá-Hernández F, Simonetti M, Larrosa I (2013) Angew Chem Int Ed 52:11458
54. Paterson AJ, St John-Campbell S, Mahon MF, Press NJ, Frost CG (2015) Chem Commun
    51:12807
55. Li Z-Y, Li L, Li Q-L, Jing K, Xu H, Wang G-W (2017) Chem Eur J 23:3285
56. Ruan Z, Zhang S-K, Zhu C, Ruth PN, Stalke D, Ackermann L (2017) Angew Chem Int Ed
    56:2045
57. Leow D, Li G, Mei T-S, Yu J-Q (2012) Nature 486:518
58. Dai H-X, Li G, Zhang X-G, Stepan AF, Yu J-Q (2013) J Am Chem Soc 135:7567
59. Lee S, Lee H, Tan KL (2013) J Am Chem Soc 135:18778
60. Wan L, Dastbaravardeh N, Li G, Yu J-Q (2013) J Am Chem Soc 135:18056
61. Bera M, Modak A, Patra T, Maji A, Maiti D (2014) Org Lett 16:5760
62. Tang R-Y, Li G, Yu J-Q (2014) Nature 507:215
63. Yang G, Lindovska P, Zhu D, Kim J, Wang P, Tang R-Y, Movassaghi M, Yu J-Q (2014) J
    Am Chem Soc 136:10807
64. Bag S, Patra T, Modak A, Deb A, Maity S, Dutta U, Dey A, Kancherla R, Maji A, Hazra A,
    Bera M, Maiti D (2015) J Am Chem Soc 137:11888
65. Bera M, Maji A, Sahoo SK, Maiti D (2015) Angew Chem Int Ed 54:8515

66. Deng Y, Yu J-Q (2015) Angew Chem Int Ed 54:888
67. Frost CG, Paterson AJ (2015) ACS Cent Sci 1:418
68. Li S, Ji H, Cai L, Li G (2015) Chem Sci 6:5595
69. Maji A, Bhaskararao B, Singha S, Sunoj RB, Maiti D (2016) Chem Sci 7:3147
70. Chu L, Shang M, Tanaka K, Chen Q, Pissarnitski N, Streckfuss E, Yu J-Q (2015) ACS Cent Sci 1:394
71. Xu H-J, Lu Y, Farmer ME, Wang H-W, Zhao D, Kang Y-S, Sun W-Y, Yu J-Q (2017) J Am Chem Soc 139:2200
72. Cheng C, Hartwig JF (2014) Science 343:853
73. Luo J, Preciado S, Larrosa I (2014) J Am Chem Soc 136:4109
74. Wang XC, Gong W, Fang LZ, Zhu RY, Li SH, Engle KM, Yu JQ (2015) Nature 519:334
75. Shen P-X, Wang X-C, Wang P, Zhu R-Y, Yu J-Q (2015) J Am Chem Soc 137:11574
76. Ye J, Lautens M (2015) Nat Chem 7:863
77. Wang P, Li G-C, Jain P, Farmer ME, He J, Shen P-X, Yu J-Q (2016) J Am Chem Soc 138:14092
78. Wang P, Farmer ME, Huo X, Jain P, Shen P-X, Ishoey M, Bradner JE, Wisniewski SR, Eastgate MD, Yu J-Q (2016) J Am Chem Soc 138:9269
79. Della Ca' N, Fontana M, Motti E, Catellani M (2016) Acc Chem Res 49:1389
80. Kuninobu Y, Ida H, Nishi M, Kanai M (2015) Nat Chem 7:712
81. Davis HJ, Mihai MT, Phipps RJ (2016) J Am Chem Soc 138:12759
82. Chu L, Wang X-C, Moore CE, Rheingold AL, Yu J-Q (2013) J Am Chem Soc 135:16344
83. Yang L, Huang H (2012) Catal Sci Technol 2:1099
84. Wencel-Delord J, Colobert F (2013) Chem Eur J 19:14010
85. Zheng C, You S-L (2014) RSC Adv 4:6173
86. Bera M, Sahoo SK, Maiti D (2016) ACS Catal 6:3575
87. Shi B-F, Maugel N, Zhang Y-H, Yu J-Q (2008) Angew Chem Int Ed 47:4882
88. Shi B-F, Zhang Y-H, Lam JK, Wang D-H, Yu J-Q (2009) J Am Chem Soc 132:460
89. Cheng X-F, Li Y, Su Y-M, Yin F, Wang J-Y, Sheng J, Vora HU, Wang X-S, Yu J-Q (2013) J Am Chem Soc 135:1236
90. Gao D-W, Shi Y-C, Gu Q, Zhao Z-L, You S-L (2012) J Am Chem Soc 135:86
91. Pi C, Li Y, Cui X, Zhang H, Han Y, Wu Y (2013) Chem. Sci. 4:2675
92. Chu L, Xiao K-J, Yu J-Q (2014) Science 346:451
93. Chan KSL, Fu H-Y, Yu J-Q (2015) J Am Chem Soc 137:2042
94. Xiao K-J, Chu L, Chen G, Yu J-Q (2016) J Am Chem Soc 138:7796
95. Albicker MR, Cramer N (2009) Angew Chem Int Ed 48:9139
96. Anas S, Cordi A, Kagan HB (2011) Chem Commun 47:11483
97. Nakanishi M, Katayev D, Besnard C, Kündig EP (2011) Angew Chem Int Ed 50:7438
98. Martin N, Pierre C, Davi M, Jazzar R, Baudoin O (2012) Chem Eur J 18:4480
99. Saget T, Cramer N (2013) Angew Chem Int Ed 52:7865
100. Saget T, Lemouzy SJ, Cramer N (2012) Angew Chem Int Ed 51:2238
101. Saget T, Cramer N (2012) Angew Chem Int Ed 51:12842
102. Sevov CS, Hartwig JF (2013) J Am Chem Soc 135:2116
103. Thalji RK, Ellman JA, Bergman RG (2004) J Am Chem Soc 126:7192
104. Brussee J, Jansen ACA (1983) Tetrahedron Lett 24:3261
105. Brussee J, Groenendijk JLG, te Koppele JM, Jansen ACA (1985) Tetrahedron 41:3313
106. Smrcina M, Lorenc M, Hanus V, Sedmera P, Kocovsky P (1992) J Org Chem 57:1917
107. https://www.nobelprize.org/nobel_prizes/chemistry/laureates/1922/
108. Sundqvist B, Macfarlane RD (1985) Mass Spectrom Rev 4: 421
109. Barber M, Bordoli RS, Elliott GJ, Sedgwick RD, Tyler AN, Green BN (1982) J Chem Soc, Chem Commun 936
110. Yamashita M, Fenn JB (1984) J Phys Chem 88:4451
111. Tanaka K, Waki H, Ido Y, Akita S, Yoshida Y, Yoshida T, Matsuo T (1988) Rapid Commun Mass Spectrom 2:151
112. Colton R, D'Agostino A, Traeger JC (1995) Mass Spectrom Rev 14:79

113. Nachtigall FM, Eberlin MN (2010) Reactive intermediates. Wiley-VCH Verlag GmbH & Co. KGaA, p 63
114. Qian R, Zhou J, Yao S, Wang H, Guo Y (2010) Reactive intermediates. Wiley-VCH Verlag GmbH & Co. KGaA, p 113
115. Santos LS (2010) Reactive intermediates. Wiley-VCH Verlag GmbH & Co. KGaA, p 133
116. Schröder D (2012) Acc Chem Res 45:1521
117. Cheng ZL, Siu KWM, Guevremont R, Berman SS (1992) J Am Soc Mass Spectrom 3:281
118. Jurneczko E, Barran PE (2011) Analyst 136:20
119. Ruotolo BT, Giles K, Campuzano I, Sandercock AM, Bateman RH, Robinson CV (2005) Science 310:1658
120. Laganowsky A, Reading E, Allison TM, Ulmschneider MB, Degiacomi MT, Baldwin AJ, Robinson CV (2014) Nature 510:172
121. Zhou M, Politis A, Davies R, Liko I, Wu K-J, Stewart AG, Stock D, Robinson CV (2014) Nat Chem 6:208
122. Wu C, Murray MM, Bernstein SL, Condron MM, Bitan G, Shea JE, Bowers MT (2009) J Mol Biol 387:492
123. Teplow DB, Lazo ND, Bitan G, Bernstein S, Wyttenbach T, Bowers MT, Baumketner A, Shea J-E, Urbanc B, Cruz L, Borreguero J, Stanley HE (2006) Acc Chem Res 39:635
124. Bowers MT (2014) Int J Mass Spectrom 370:75
125. Bernstein SL, Wyttenbach T, Baumketner A, Shea J-E, Bitan G, Teplow DB, Bowers MT (2005) J Am Chem Soc 127:2075
126. Bernstein SL, Dupuis NF, Lazo ND, Wyttenbach T, Condron MM, Bitan G, Teplow DB, Shea J-E, Ruotolo BT, Robinson CV, Bowers MT (2009) Nat Chem 1:326
127. Baumketner A, Bernstein SL, Wyttenbach T, Bitan G, Teplow DB, Bowers MT, Shea J-E (2006) Protein Sci 15:420
128. Révész Á, Schröder D, Rokob TA, Havlík M, Dolenský B (2011) Angew Chem Int Ed 50:2401
129. Shaffer CJ, Schröder D, Gütz C, Lützen A (2012) Angew Chem Int Ed 51:8097
130. Ducháčková L, Roithová J, Milko P, Žabka J, Tsierkezos N, Schröder D (2010) Inorg Chem 50:771
131. Tsybizova A, Rulíšek L, Schröder D, Rokob TA (2012) J Phys Chem A 117:1171
132. Schröder D, Buděšínský M, Roithová J (2012) J Am Chem Soc 134:15897
133. Revesz A, Schröder D, Rokob TA, Havlik M, Dolensky B (2012) Phys Chem Chem Phys 14:6987
134. Harvey SR, MacPhee CE, Barran PE (2011) Methods 54:454
135. Lanucara F, Holman SW, Gray CJ, Eyers CE (2014) Nat Chem 6:281
136. Wyttenbach T, Kemper PR, Bowers MT (2001) Int J Mass Spectrom 212:13
137. Canterbury JD, Yi X, Hoopmann MR, MacCoss M (2008) J Anal Chem 80:6888
138. Purves RW, Guevremont R (1999) Anal Chem 71:2346
139. Giles K, Pringle SD, Worthington KR, Little D, Wildgoose JL, Bateman RH (2004) Rapid Commun Mass Spectrom 18:2401
140. http://www.waters.com/waters/home.htm
141. Pringle SD, Giles K, Wildgoose JL, Williams JP, Slade SE, Thalassinos K, Bateman RH, Bowers MT, Scrivens JH (2007) Int J Mass Spectrom 261:1
142. Ponthus J, Riches E (2013) Int. J. Ion Mobil. Spec. 16:95
143. Wyttenbach T, Helden GV, Batka Jr JJ, Carlat D, Bowers MT (1997) J Am Soc Mass Spectrom 8:275
144. Shvartsburg AA, Jarrold MF (1996) Chem Phys Lett 261:86
145. Shvartsburg AA, Schatz GC, Jarrold MF (1998) J Chem Phys 108:2416
146. https://labs.chem.ucsb.edu/bowers/michael/theory_analysis/cross-sections/index.shtml
147. Bleiholder C, Wyttenbach T, Bowers MT (2011) Int J Mass Spectrom 308:1
148. http://www.indiana.edu/~nano/software.html
149. Williams VM, Kong JR, Ko BJ, Mantri Y, Brodbelt JS, Baik M-H, Krische MJ (2009) J Am Chem Soc 131:16054

150. Gellrich U, Meißner A, Steffani A, Kähny M, Drexler H-J, Heller D, Plattner DA, Breit B (2013) J Am Chem Soc 136:1097
151. Ducháčková L, Roithová J, Milko P, Žabka J, Tsierkezos N, Schröder D (2011) Inorg Chem 50:771
152. Tsybizova A, Rulíšek L, Schröder D, Rokob TA (2013) J Phys Chem A 117:1171
153. Schröder D, Buděšínský M, Roithová J (2012) J Am Chem Soc 134:15897
154. Schrödinger E (1926) Phys Rev 28:1049
155. Roothaan CCJ (1951) Rev Mod Phys 23:69
156. Hohenberg P, Kohn W (1964) Phys Rev 136:B864
157. Kohn W, Sham LJ (1965) Phys Rev 140:A1133
158. Becke AD (1993) J Chem Phys 98:5648
159. Lee C, Yang W, Parr RG (1988) Phys Rev B 37:785
160. Brooks BR, Bruccoleri RE, Olafson BD, States DJ, Swaminathan S, Karplus M (1983) J Comput Chem 4:187
161. Cornell WD, Cieplak P, Bayly CI, Gould IR, Merz KM, Ferguson DM, Spellmeyer DC, Fox T, Caldwell JW, Kollman PA (1995) J Am Chem Soc 117:5179
162. Jorgensen WL, Tirado-Rives J (1988) J Am Chem Soc 110:1657
163. Schuler LD, Daura X, van Gunsteren WF (2001) J Comput Chem 22:1205
164. Warshel A, Levitt M (1976) J Mol Biol 103:227
165. Dapprich S, Komáromi I, Byun KS, Morokuma K, Frisch MJJ (1999) Mol Struc-Theochem 461–462:1
166. Senn HM, Thiel W (2007) Curr Opin Chem Biol 11:182
167. Cheng G-J, Zhang X, Chung LW, Xu L, Wu Y-D (2015) J Am Chem Soc 137:1706
168. Thiel W (2011) Angew Chem Int Ed 50:9216
169. Thiel W (2014) Angew Chem Int Ed 53:8605
170. Cheong PH-Y, Legault CY, Um JM, Çelebi-Ölçüm N, Houk KN (2011) Chem Rev 111:5042
171. Houk KN (2014) Chem Soc Rev 43:4905
172. Tsang ASK, Sanhueza IA, Schoenebeck F (2014) Chem –Eur J 20:16432
173. Ditchfield R, Hehre WJ, Pople JA (1971) J Chem Phys 54:724
174. Wheeler SE, Moran A, Pieniazek SN, Houk KN (2009) J Phys Chem A 113:10376
175. Schreiner PR (2007) Angew Chem Int Ed 46:4217
176. Schwabe T, Grimme S (2008) Acc Chem Res 41:569
177. Grimme S (2006) J Comput Chem 27:1787
178. Zhao Y, Schultz NE, Truhlar DG (2005) J Chem Phys 123:161103
179. Zhao Y, Schultz NE, Truhlar DG (2006) J Chem Theory Comput 2:364
180. Zhao Y, Truhlar D (2008) Theor Chem Acc 120:215
181. Ahlquist MSG, Norrby P-O (2011) Angew Chem Int Ed 50:11794

Chapter 2
Mechanistic Studies on Pd(OAc)$_2$-Catalyzed *Meta*-C–H Activation Reaction

Abstract This chapter describes a comprehensive computational study on the template-assisted and Pd(OAc)$_2$-catalyzed *meta*-selective C–H olefination reaction. The reaction mechanism, the active form of catalyst, the potential role of silver salt and the origin of *meta*-selectivity were investigated in this work. The computational results demonstrated that the conventionally proposed monomeric Pd(OAc)$_2$ model predicts *ortho*-selectivity, instead novel dimeric Pd$_2$(OAc)$_4$ and Pd–Ag(OAc)$_3$ models successfully reproduce the experimentally observed *meta*-selectivity.

2.1 Introduction

Transition metal-catalyzed C–H activation reactions have received great attention in recent years [1–12]. The strategy to use directing group to increase the reactivity and control regioselectivity have been extensively applied in C–H activation reactions [13–20]. While in most of the directing group-assisted C–H activation reactions, substrate usually binds with transition metal to form a five- or six-membered cyclic transition state and active *ortho*-C–H bond selectively. A breakthrough work from the Yu group reported an ingenious template strategy for *meta*-selective C–H activation of arenes (Scheme 2.1) in 2012 [21]. In this strategy, they used end-on nitrile template to direct Pd to reach and activate *meta*-C–H bond via a macrocyclic structure. With this method, they realized *meta*-C–H activation and olefination reactions of a broad range of arene substrates including toluene derivatives and phenylpropionic acid derivatives. This new method overrides the electronic and steric bias of substrates as well as the *ortho* directing effect of chelating group to activate the remote *meta*-C–H bond which is 10 or 11
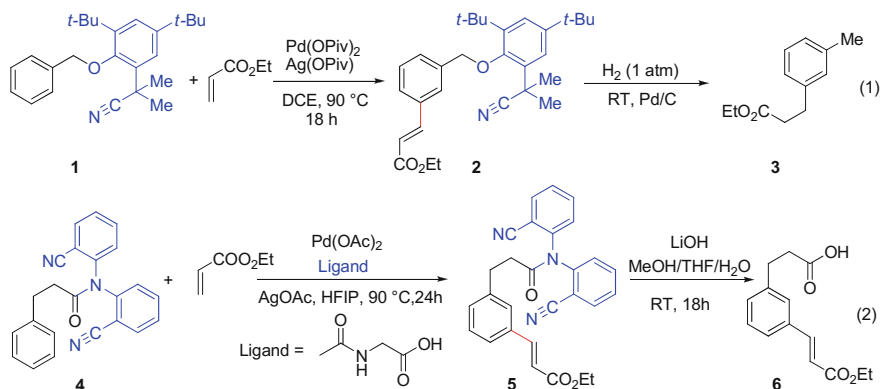

Scheme 2.1 The first reported work about Pd(II)-catalyzed *meta*-selective C$_{aryl}$–H bond activation using a removable end-on nitrile template

chemical bonds away from the directing group (nitrile group) with high selectivity. The template design concept in this work represents remarkable progress in the field of C–H activation and opens new opportunities for achieving unusual selecitivities in C–H activation of arenes.

Since the Yu group's seminal work, the template strategy has rapidly been applied to a series of Pd(II)-catalyzed C$_{aryl}$-H activation and functionalization to achieve *meta* and *para* selectivity [21–33]. These extensive successful examples demonstrate the enormous potential in synthetic application for this strategy. Understanding on reaction mechanism will facilitate the development of new reactions. However, its reaction mechanism and the origin of *meta*-selectivity were unclear. Therefore, we conducted mechanistic studies on reaction 1 and intended to address two critical issues: (1) what is the mechanism of reaction 1 and what is the active form of the catalyst? (2) What is the origin of *meta*-selectivity?

In regard to the active form of the catalyst, palladium catalyst can be effective in various forms [34] depending on the ligand, temperature, solvent and other reaction conditions. Despite the general mechanism of Pd-catalyzed C–H bond activation has been explored by experiments [35–40] and computations [41–47], it is still controversial about whether monomeric, dimeric or trimeric Pd is the active catalyst. In the oxazoline directed Pd-catalyzed sp^3 C–H activation and iodination reaction reported by the Yu group [48], they characterized the X-ray structure of the C–H activated trinuclear palladyacycle complex **7**. The Houk group investigated the mechanism of this reaction [49] and found that monomeric Pd complex is the active catalyst and this trimeric intermediate is formed via a monomeric Pd transition state (**8**).

Dimeric palladium complexes are quite common in literature [50, 51]. For example, the Ritter group [52] synthesized acetate group bridged Pd^{II}–Pd^{II} dimeric complex [(2-phenylpyridine)Pd(μ-OAc)]$_2$ (**9**). Other dimeric palladium complexes with succinic acid (**10**) or other carboxylic acids as linker have been reported [53].
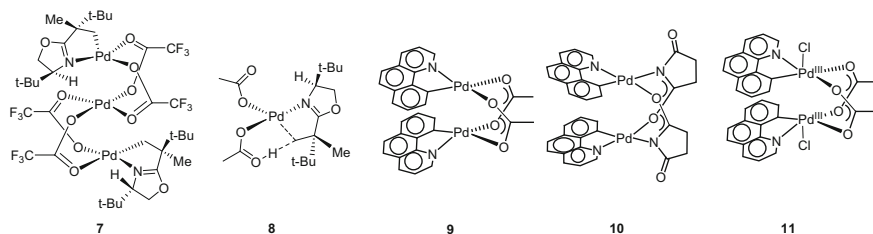
Scheme 2.2 Trimeric and dimeric palladium complexes (**7** and **9–11**) and monomeric TS**8** reported in literature

Many of these dimeric Pd complexes are critical intermediates in Pd^{II}/Pd^{IV} catalytic cycle. High-valent binuclear Pd^{III}–Pd^{III} complexes [54] have also been developed and applied as redox catalysts for C-X reductive elimination [55]. In a recently published work by the Hartwig group [56], the C–H arylation of pyridine N-oxide is assisted by a cyclopalladated dinuclear Pd complex in which C–H bond cleavage occurs at one Pd center while the functionalization step proceeds at the second Pd center. In the study on Pd-catalyzed C–H oxidative coupling of 1,3-dimethoxybenzene with benzo[h]quinolone by Sanford and Schoenebeck and co-workers [57], both monomeric and dimeric Pd mechanisms have been investigated. Their study showed that the predicted selectivity is equivalent for carbonate and acetate, no matter whether dimeric or monomeric Pd complexes are considered and the C–H bond activation of the substrate occurs at one Pd^{II} center in their dimeric model.

Monomeric Pd complex has been extensively considered as active form for palladium catalysts. Most of mechanistic studies of palladium acetate catalyzed reactions are based on monomeric palladium complex [41–43, 58–61].

We speculated that for remote C–H activation and functionalization, the active species may be affected by the template. Thus, in the present work, we investigated several possible mechanisms involving monomeric, dimeric and trimeric palladium as active catalyst (Scheme 2.2).

2.2 Computational Method

All DFT calculations were carried out using Gaussian 09 program [62]. Geometry optimization was performed with B3LYP [63–66] hybrid density functional theory. LANL2DZ + f (1.472) [67, 68] basis set with effective core potential (ECP) was used for Pd, LANL2DZ + f (1.611) basis set with ECP was used for Ag, and 6-31G (d) [69, 70] basis set was used for other atoms. Frequency calculation for optimized structures was conducted at the same level of theory to verify the stationary points to be real minima (no imaginary frequency) or transition state (one imaginary frequency) and to obtain thermodynamic energy corrections. Single point energies

were calculated at M06/SDD-6-311++G(d, p) [71–74] level and the solvent effect was evaluated by using SMD solvation model [75]. The relative energies with ZPE corrections and free energies (at 363.15 K) are in kcal/mol. 3D structures are displayed with CYLView [76].

2.3   Results and Discussion

We first calculated the possible states of palladium acetate, i.e., trimeric, dimeric, and monomeric forms of palladium acetate. Trimeric palladium acetate is the most stable complex which is in agreement with previous experimental study [49]. Dimeric palladium complexes **B** (with four acetate bridges) and **C** (with two acetate bridges) are less stable than trimeric palladium acetate **A** by 8.1 kcal/mol and 13.8 kcal/mol, respectively. Monomeric palladium acetate **D** is also less stable than **A** by 11.8 kcal/mol. Therefore, trimeric Pd$_3$(OAc)$_6$ was used as reference complex in the following studies (Fig. 2.1).

2.3.1   *Monomeric Pd(OAc)$_2$ Mechanism*

Monomeric Pd pathway was studied first since monomeric Pd(OAc)$_2$ was conventionally considered as active catalyst for palladium acetate catalyzed reactions in experimental and computational works. There are four commonly proposed mechanisms for transition metal-catalyzed C–H activation reactions: oxidative addition, electronic aromatic substitution (EAS), concerted metalation and deprotonation (CMD) [36, 41, 60, 77–79] and σ-bond metathesis. The computed activation energies of these four pathways [80] are summarized in Fig. 2.2. The oxidative addition and σ-bond metathesis pathways are highly unfavorable and their activation free energies are 69.5 and 54.1 kcal/mol, respectively. Trials for locating TS of EAS pathway were failed. The optimizations of TS for EAS pathway always

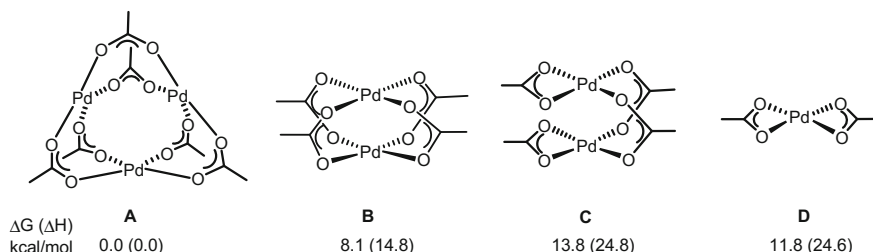|	**A**	**B**	**C**	**D**
ΔG (ΔH) kcal/mol	0.0 (0.0)	8.1 (14.8)	13.8 (24.8)	11.8 (24.6)

Fig. 2.1 Trimeric, dimeric and monomeric palladium acetates and their corresponding relative free energies (electronic energies)
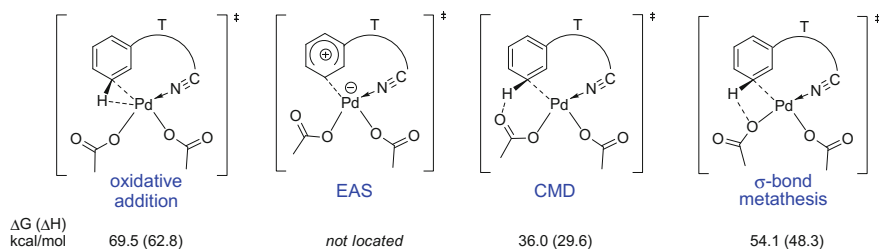
Fig. 2.2 Four conventionally proposed reaction mechanisms for transition metal-catalyzed C–H activation and computed activation free energies (electronic energies)

converged to the intermediate with arene coordinating with Pd which indicates EAS pathway is not favorable. CMD pathway has the lowest activation energy (36.0 kcal/mol) among the four mechanisms which is in accordance with the previous study on Pd(OAc)$_2$ catalyzed C–H activation reaction [49, 81]. Thus we only considered the CMD mechanism in the following sections.

The catalytic cycle of reaction 1 is depicted in Scheme 2.3. The monomeric Pd (OAc)$_2$ is generated from the dissociation of the trimeric Pd$_3$(OAc)$_6$ complex. The nitrile group of substrate coordinates with Pd to form an intermediate **Int0a** and the further binding of C–H bond of the substrate with Pd leads to **Int0**. In **Int0**, the
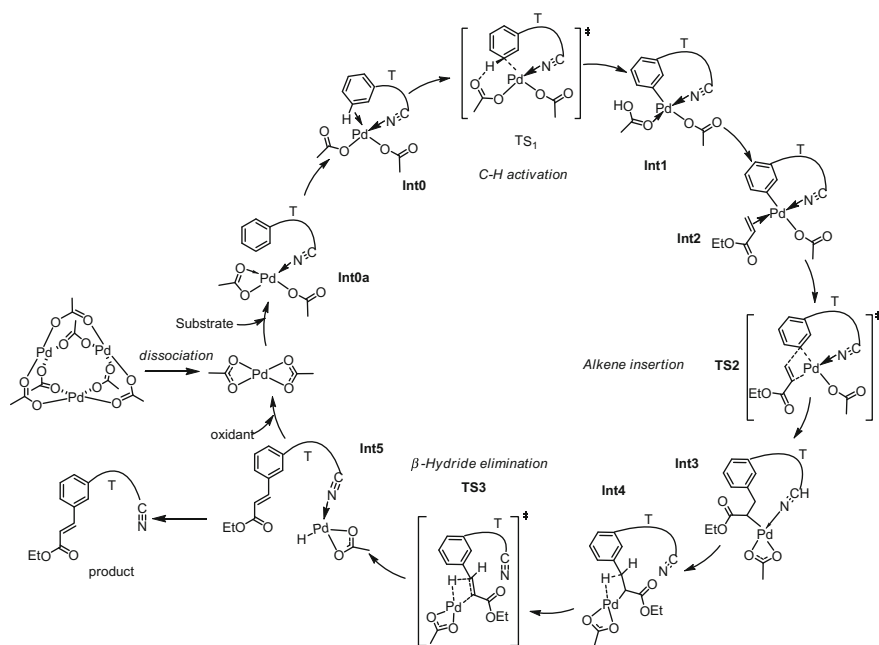
Scheme 2.3 Catalytic cycle of monomeric Pd(OAc)$_2$ mechanism. Reprinted with the permission from Ref. [93]. Copyright 2013 American Chemical Society

C–H bond is pre-activated via agostic interaction with Pd. After C–H bond acti-
vation step, a cyclopalladated complex **Int1** is formed. Olefin replaces acetic acetate
to coordinate with Pd forming complex **Int2**. Olefination insertion followed by
β-hydride elimination generates **Int5**. Then the product dissociates from Pd and
reductive elimination releases acetic acid. Finally the Ag^I oxidant oxidizes Pd^0 to
regenerate the Pd^{II} catalyst.

The reaction profile for monomeric Pd pathway is shown in Fig. 2.3. The forma-
tion of monomeric palladium complex **Int0a_a** from the binding of the substrate
towards trimeric Pd$_3$(OAc)$_6$ is endothermic by 17.0 kcal/mol. The formation of
Int0_a requires 4.0 kcal/mol free energy from **Int0a_a**. The C–H bond activation step
needs to overcome a barrier of 36.0 kcal/mol and generates cyclopalladated complex
Int1_a. The replacement of acetic acid by olefin is exothermic by 5.8 kcal/mol. The
olefin insertion step is a facile process with a barrier of 24.8 kcal/mol which leads to a
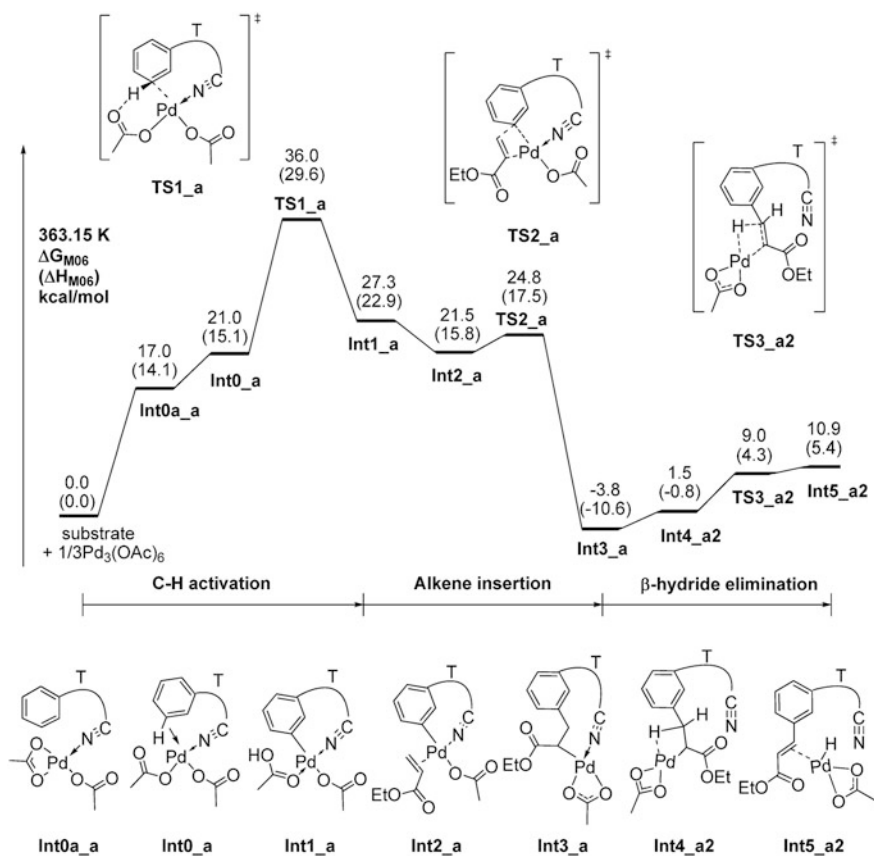

Fig. 2.3 Energy profile for the *meta* pathway in the monomeric Pd(OAc)$_2$ mechanism. Reprinted
with the permission from Ref. [93]. Copyright 2013 American Chemical Society

stable complex **Int3_a**. The following β-hydride elimination step is very favorable process with a low barrier of 12.8 kcal/mol. Therefore, the C–H activation step is the rate-determining step as well as regioselectivity-determining step.

To investigate the regioselectivity, the TSs for *meta*-, *ortho*-, and *para*-C–H activation were calculated since C–H activation step is the regioselectivity-determining step. We took into account the different coordination states of the nitrile group of the substrate. As presented in Fig. 2.4(b), both TSs with nitrile coordinating with Pd (**meta_TS1_a**, **ortho_TS1_a** and **para_TS1_a**) and TSs without nitrile group binding with Pd (**meta_TS1_a2**, **ortho_TS1_a2** and **para_TS1_a2**) were calculated. It is found that in the TSs in which the nitrile group does not bind with Pd the substrate adopts a similar conformation with the ground state of the substrate (Fig. 2.4a). The dihedral angles around the C-O bond of benzyl ether in all these structures are close to 180°. Computational results demonstrate that the TS for *ortho*-C–H bond activation is more favorable than the corresponding *meta*- and *para*-TS by 1.8 and 0.8 kcal/mol, respectively, suggesting that the monomeric pathway mainly leads to *ortho*- and *para*-C–H bond functionalized products in the absence of the nitrile directing group.

In the case of the nitrile group coordinating with Pd, the activation barriers for *meta*- and *para*-TS do not change much compared to the previously discussed case without nitrile group binding to Pd. But the activation barrier of *ortho*-TS decreases significantly when the nitrile group coordinates with Pd, indicating the template promotes *ortho*-C–H bond activation for monomeric mechanism. The **ortho_TS1_a** is 5.9 kcal/mol lower in activation free energy than **meta-TS1_a**.

To understand the *ortho*-selectivity for monomeric mechanism, a further distortion-interaction analysis [82] was conducted. As shown in Scheme 2.4, the activation barrier is decomposed by an unfavorable distortion energy which is due to the conformational changes of the substrate and catalyst from reactant state to transition state and a favorable interaction between the catalyst and substrate. The system is divided into catalyst part and substrate part and their distortion energies are evaluated by the energetic differences from the reactant state to TS. Computational results (Table 2.1) demonstrate that the energetic differences of *ortho*-, *meta*-, and *para*-TS are mainly attributed to the differences in distortion energy of the substrate part. The substrate in **ortho_TS1_a** is less distorted (the distortion energy is 36.7 kcal/mol) while the distortion energies of substrate part for **meta_TS1_a** and **para_TS1_a** are 44.1 and 43.2 kcal/mol which are much higher than that in **ortho_TS1_a**. Structural analysis indicates that the greater distortion in **meta_TS1_a** and **para_TS1_a** is mainly due to the torsion about the benzyl ether C–O bond, which places two bulky groups (aryl group and benzyl group) in gauche position in the *meta*- and *para*-TS ($\psi 3 = 78°$ and 64°, respectively), while the two bulky groups are in anti-position in the preferred *ortho*-TS. In addition, **meta_TS1_a** is destabilized by the torsion about $\psi 2$ which is enlarged from $-101°$ in reactant to $-118°$ in *meta*-TS as well as steric repulsion between the nitrogen atom of the nitrile group and the *ortho* carbon atom (N–C distance is 2.81 Å). **para_TS1_a** is also destabilized by steric repulsion between the ether oxygen and methyl group (O–C distance is 2.77 Å).
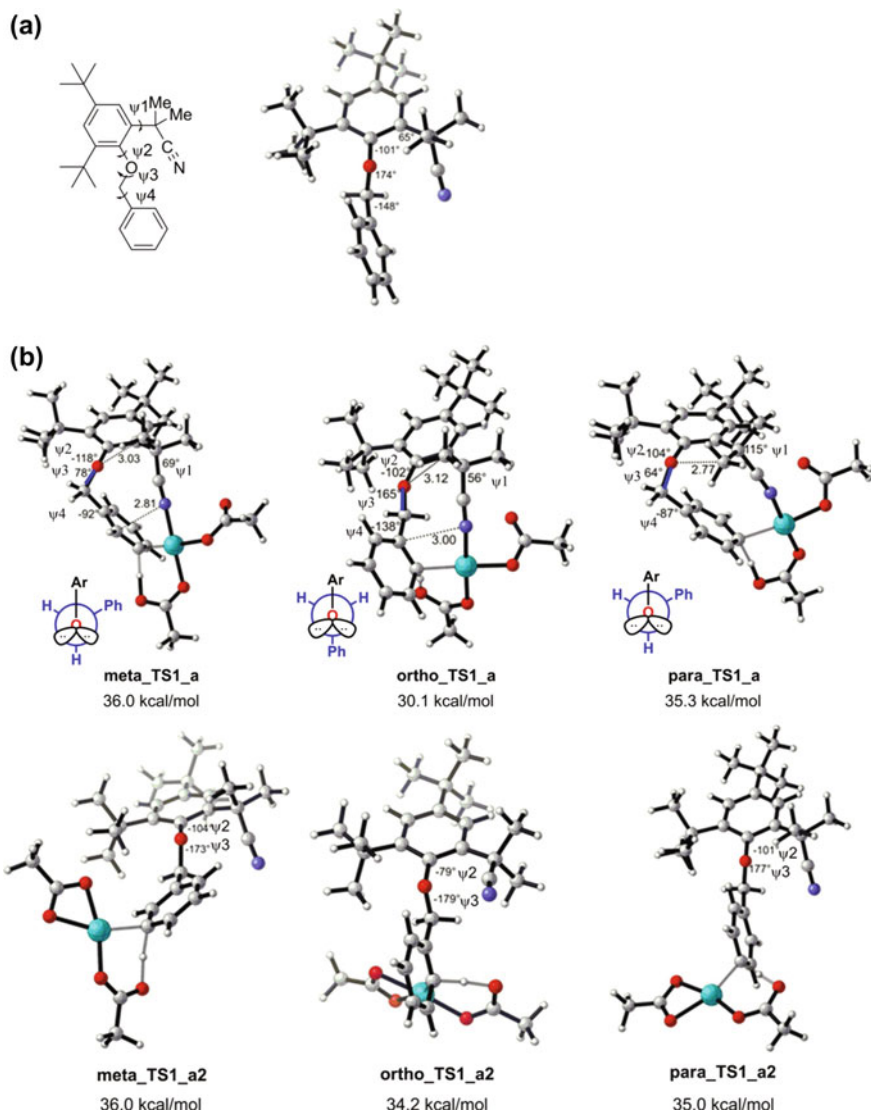
Fig. 2.4 **a** Lowest energy conformation of toluene derivative substrate with nitrile-containing template. **b** Optimized geometries of *meta*, *ortho*, and *para* C–H activation transition states of the monomeric Pd(OAc)$_2$ mechanism. In **TS1_a**, the nitrile group is coordinated to Pd; in **TS1_a2**, it is not. Gibbs activation free energies with solvation correction are given in kcal/mol. Reprinted with the permission from Ref. [93]. Copyright 2013 American Chemical Society

In summary, *ortho*-selectivity is predicted by monomeric Pd(OAc)$_2$ mechanism which contradicts with the experimentally observed *meta*-selectivity (*m*:*p*:*o* = 91:7:2).
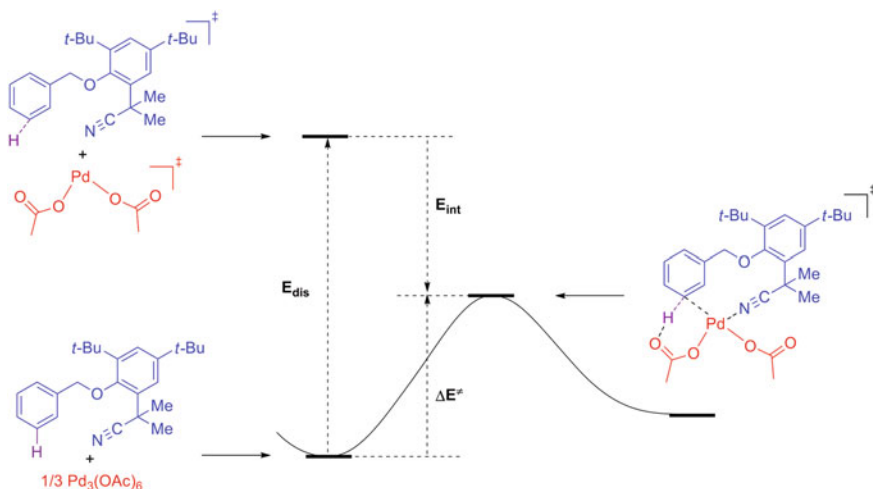
Scheme. 2.4 Schematic diagram for distortion-interaction analysis

Table 2.1 Distortion energy analysis of C–H activation TSs of monomeric models

Distortion energy (kcal/mol)	meta_TS1_a	ortho_TS1_a	para_TS1_a
E_{cat}	63.1	61.8	62.8
E_{sub}	44.1	36.7	43.2
E_{total}	107.2	98.5	106.0

2.3.2 Dimeric Pd₂(OAc)₄ Mechanism

The above computational results demonstrated that the traditional monomeric Pd
$(OAc)_2$ mechanism fails to explain the *meta*-selectivity of reaction 1 which impels
us to investigate new mechanistic scenarios. Compared to the widely studied
substrates in $Pd(OAc)_2$ catalyzed C–H bond activation reactions, substrate **1** fea-
tures with a long linker which connects the remote directing group (nitrile group)
and the aryl ring. The long linker enables both the directing group and the aryl
group of the substrate to bind with two different Pd atoms in dimeric Pd catalyst to
form a larger macrocycle. We expect that the larger macrocycle in dimeric Pd
model may reduce the ring strain and distortion in *meta*-TS which destabilizes
meta-TS in monomeric Pd model. Therefore, the present work further investigated
the dimeric $Pd_2(OAc)_4$ mechanism.

It is worth noting that different from the dimeric palladium acetates reported in
literature which usually have two same Pd atoms (same coordination state and same
functions), the two Pd atoms have different roles in the dimeric Pd model proposed
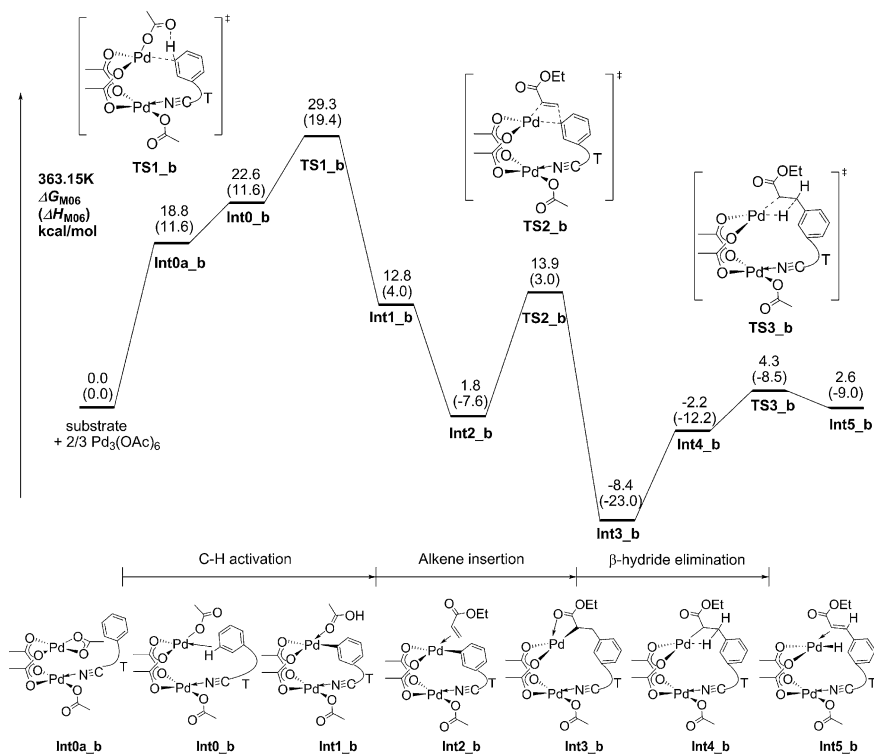
Fig. 2.5 Energy profile for the *meta* pathway in the dimeric Pd$_2$(OAc)$_6$ mechanism. Reprinted with the permission from Ref. [93]. Copyright 2013 American Chemical Society

in the present work. In the new dimeric Pd model one Pd coordinates with the nitrile group and another Pd coordinates with aryl group of the substrate and activates the C–H bond. Two Pd atoms are connected by two bidentate acetate groups. The computed energy profile for dimeric Pd mechanism is shown in Fig. 2.5. The C–H bond activation is also the rate-determining step and regioselectivity-determining step. The activation barrier of C–H activation for dimeric Pd model is 29.3 kcal/mol which is 6.7 kcal/mol lower than monomeric Pd model. The direct comparison of the activation energies of dimeric Pd mechanism and monomeric Pd mechanism requires a reliable computational method to precisely calculate the key interactions such as nonbonding interactions between Pd atoms, dispersion interactions in the macrocycle and the binding energy of ligand with Pd. The recently published benchmark studies have demonstrated that M06 provides reasonable accuracy to describe the ligand binding energy and dispersion energy [83–85]. We also tested the performance of M06 in calculating the dimerization energy of Pd dimer. The result with M06 method is in reasonable agreement with higher-level calculations (MP2 and CCSD(T)), suggesting it is also applicable to describe the nonbonding Pd–Pd interactions in present study [86].

We focused on the TSs of C–H bond activation since it determines the regios-electivity. For dimeric catalyst model, there are many possible conformations for intramolecular TS because it is a macrocycle (n-membered ring, n = 14 (*ortho*), 15 (*meta*), 16 (*para*)). In order to search these conformations systematically, we examined the structure very carefully and identify four major factors which would lead to different conformations. As shown in Scheme 2.5, the first factor is the dihedral angles Ψ_1 and Ψ_2 which determines the relative position of nitrile group and the benzene ring of substrate (on the same side of the benzene ring of template or on different sides). The second factor is the dihedral angles Ψ_3 and Ψ_4 that determines which C–H bond of two *meta*-C–H bonds (or two *ortho*-C–H bonds) will be activated. The third factor is the rotation of the spectator acetate group (dihedral angles Ψ_5) which brings the carbonyl above or below the Pd coordination plane. The fourth factor is the relative position of two acetate groups (green and purple in Scheme 2.5) which may locate at different sides (Scheme 2.5(a)) or the same side (Scheme 2.5(b)) of dimeric Pd catalyst.

Four variables result in 16 (2^4) conformations for intramolecular *meta*-C–H and intramolecular *ortho*-C–H bonds activation, respectively. And eight conformations for intramolecular *para*-C–H bond activation were obtained since there is only one *para*-C–H which is not affected by the dihedral angles Ψ_3 and Ψ_4. There are likewise three conformations for intermolecular C–H activation in which the nitrile group does not coordinate to the Pd center. Thus we studied 43 conformations in total. Eight favorable conformations (within a free energy window of 2.5 kcal/mol from the lowest one) are shown in Fig. 2.6.

The lowest activation barriers for *meta*-, *ortho*-, and *para*-C–H bond activation are 29.3, 29.7, and 33.4 kcal/mol, respectively, all are significantly lower than the corresponding activation barriers for counterpart TSs of monomeric Pd model. The TS for intramolecular *meta*-C–H bond activation has the lowest activation
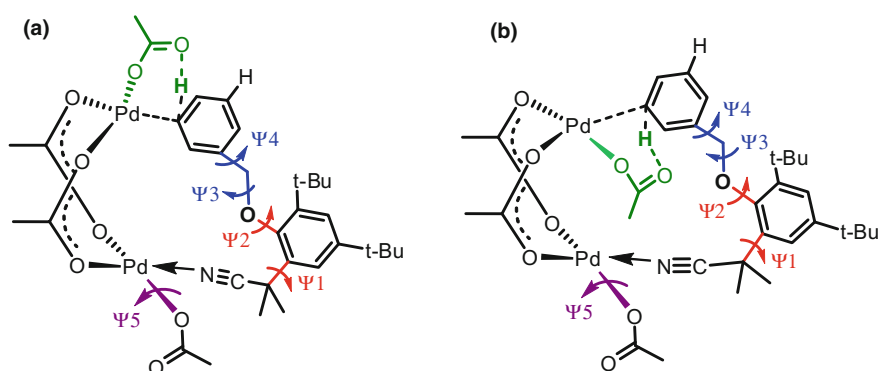
Scheme. 2.5 Conformations of *meta*-C–H bond activation transition state involving dimeric Pd catalyst. **a** Two acetate groups (*green* and *purple*) are on different sides. **b** Two acetate groups are positioned on the same side. Reprinted with the permission from Ref. [93]. Copyright 2013 American Chemical Society
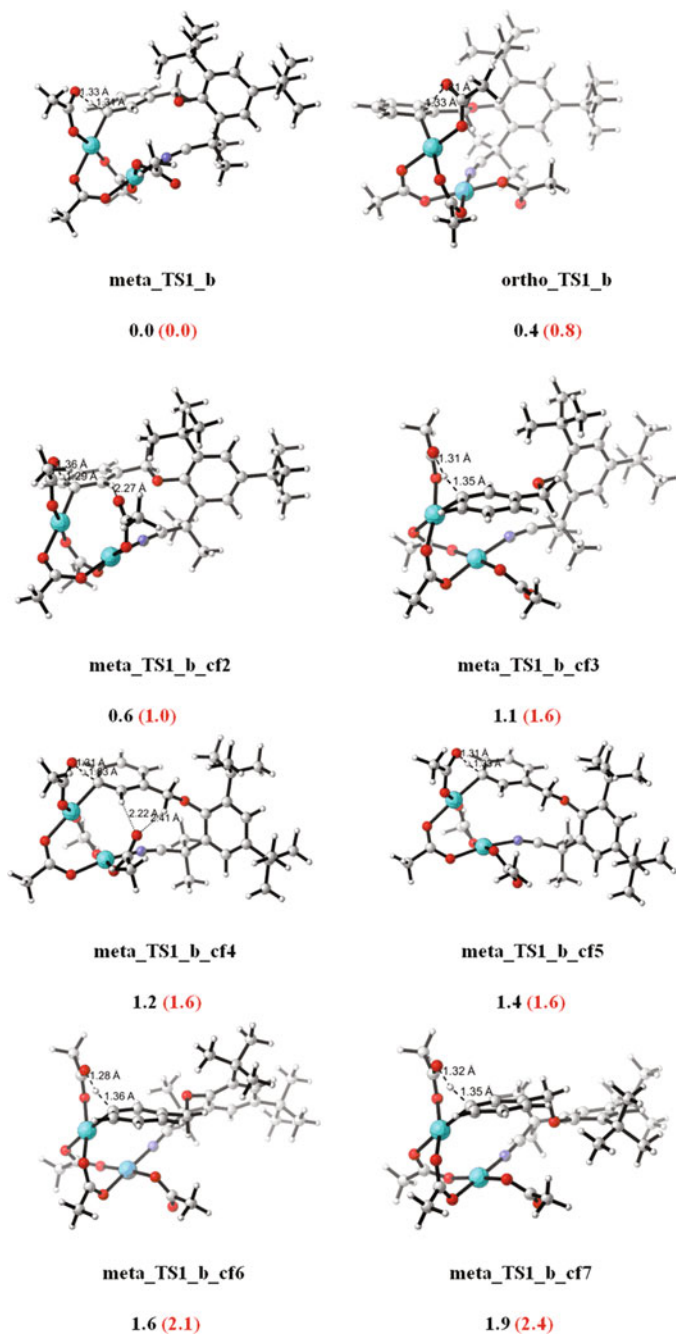
Fig. 2.6 The favored conformations of TS (within a free energy difference of 2.0 (2.5) kcal/mol) and their relative free energies (in kcal/mol, values in black were calculated at 298.15 K and values in red parentheses were calculated at 363.15 K)

energy. It is worth noting that among these stable conformations, there are seven conformations contribute to the *meta*-C–H bond activation and only one conformation is responsible for *ortho*-C–H bond activation. According to Boltzmann distribution of these TS conformers, the ratio of *meta* and *ortho* product is estimated to be 83:17 at 363.15 K. In consideration of activation free energy and the number of stable conformations of TS, *meta*-C–H bond activation is found to be more favored than *ortho*-C–H bond activation for dimeric catalyst model. This result is in agreement with experimentally observed *meta*-selectivity.

We sought to explore the structural characters of these stable conformations and found in these stable conformations two benzene rings prefer to be mutually perpendicular and the conformations which are more close to the optimized structure of template 1 are more stable. We also found the distortion of the template 1 and the ring strain of cyclopalladated macrocycle are the key factors to influence the stability of TS.

In literature, the monomeric Pd catalyst model is frequently proposed while dimeric Pd catalyst model is less investigated. It is understandable since in most cases, the substrate is a relative small molecule and the C–H bond to be activated is always close to the directing group, thus the substrate prefers to bind with one Pd atom and the C–H bond is activated via a stable five- or six-membered cyclic TS. However, in substrate **1**, the *meta*-C–H bond is 11 chemical bonds away from the nitrile group which enables the substrate to bind with dimeric Pd to form macrocycle in which the ring strain and distortion of the substrate are released.

2.3.3 Dimeric Pd–Ag(OAc)$_3$ Mechanism

The oxidant screening experiment suggests that Ag(OPiv) is an optimal oxidant while other oxidants such as O$_2$ and Ag(OTf) resulted in complete loss of reactivity and selectivity. So Dr. Yang proposed the heterodimeric Pd-Ag(OAc)$_3$ catalyst model, in which the nitrile group binds to Ag and two carboxylic groups bridge Ag and Pd atoms. Pd still act as catalyst to activate the C–H bond. The crystal structure of dimeric Pd–Ag complex has been reported in literature in which Ag binds with three or four ligands. But there is no report about Pd–Ag acts as catalyst to activate C–H bond before our work published. The potential energy surface of dimeric Pd–Ag mechanism was shown in Fig. 2.7 and it indicates that the C–H bond activation step is still the rate-determining step and also the regioselectivity-determining step. The structures of the most favorable TSs are presented in Fig. 2.8. The activation barriers for dimeric Pd–Ag complex catalyzed *meta*-, *ortho*-, and *para*-C–H bond activation are 24.8, 27.8, and 28.3 kcal/mol, respectively. Therefore, dimeric Pd–Ag model also predicts *meta*-selectivity.
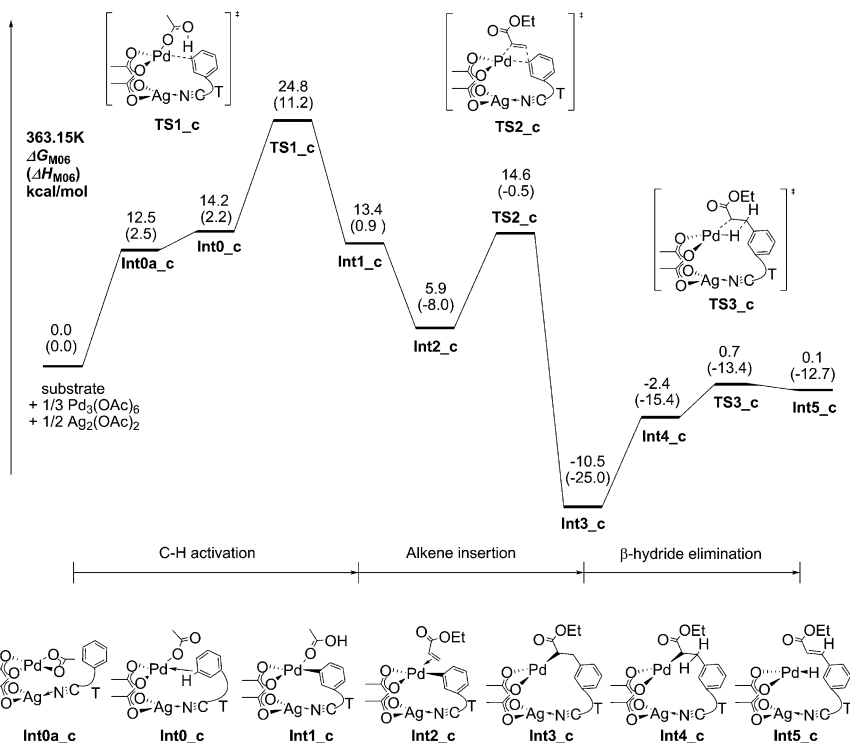
Fig. 2.7 Energy profile for *meta* pathway in heterodimeric Pd-Ag(OAc)₃ mechanism. Free energies (enthalpies) are with respect to Pd₃(OAc)₆ and Ag₂(OAc)₂. Reprinted with the permission from Ref. [93]. Copyright 2013 American Chemical Society

Fig. 2.8 C–H activation transition states and activation free energies for *meta*, *ortho*, and *para* pathways of Pd–Ag (TS1_c) dimeric mechanism. Reprinted with the permission from Ref. [93]. Copyright 2013 American Chemical Society

2.3.4 Trimeric Pd₃(OAc)₆ Mechanism

Since dimeric catalyst model successfully explains the *meta*-selectivity, we further investigated trimeric catalyst model to investigate whether trimeric Pd is also reactive in C–H activation. Similar to the dimeric case, trimeric Pd catalyst model has many possible conformations resulted from the macrocyclic TS structure. We tried different TS structures including C-conformation (**TS1_d** and **TS1_d2**) and S-conformation (**TS1_d3**) as well as the different coordinating status of nitrile group which are depicted in Fig. 2.9. However, they have much higher energy barriers (>37 kcal/mol) than momeric and dimeric TSs due to greater distortions of the trimeric catalyst which indicates this trimeric catalyst model is not reasonable.
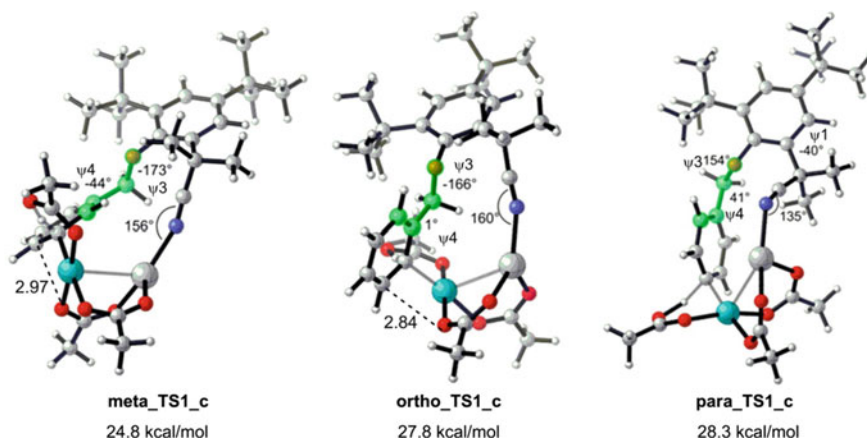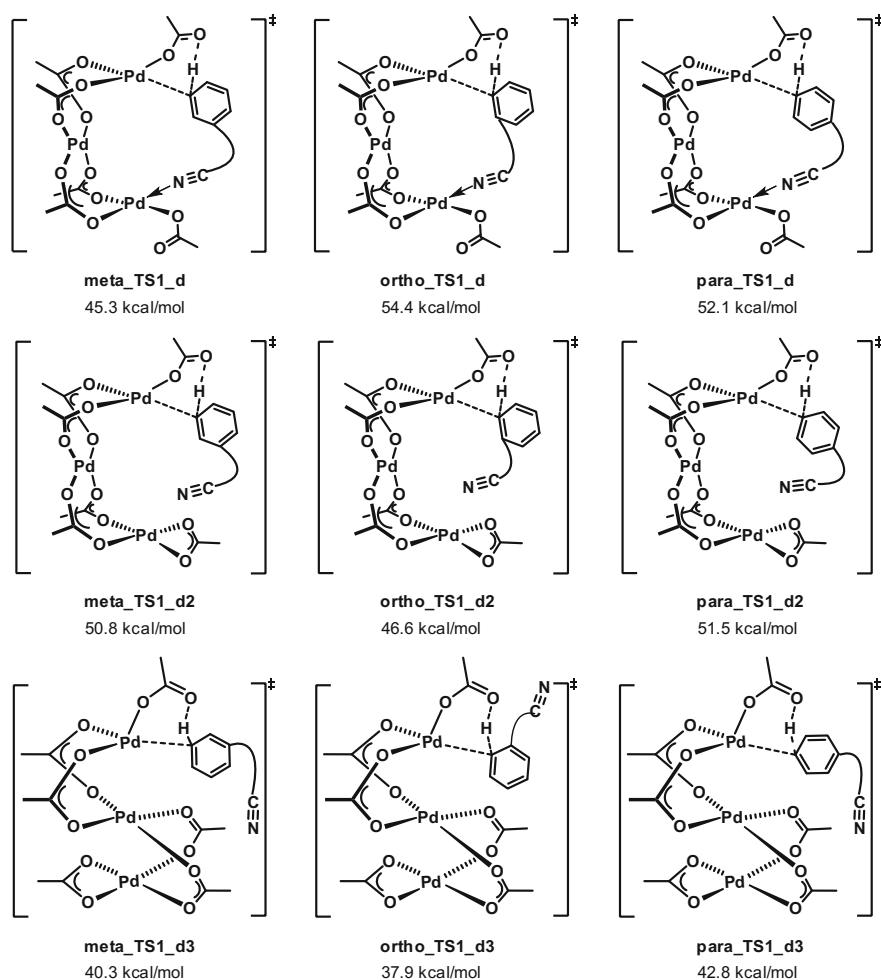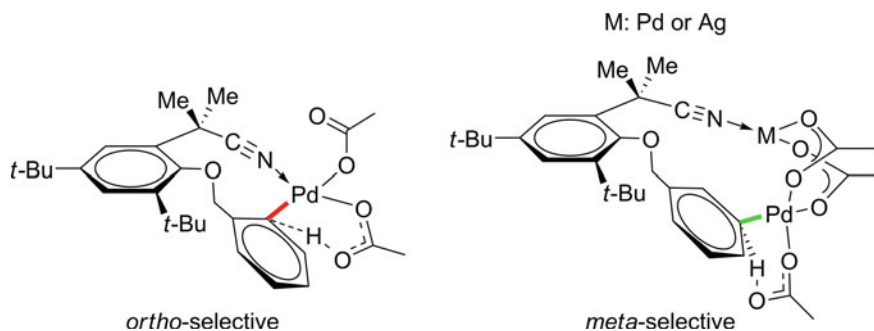

Fig. 2.9 C–H activation transition states and activation free energies for *meta*, *ortho*, and *para* pathways of trimeric Pd₃(OAc)₆ mechanism

Scheme. 2.6 Monomeric and dimeric C–H activation transition states. Reprinted with the permission from Ref. [93]. Copyright 2013 American Chemical Society

2.3.5   *Origin of* **Meta-***Selectivity in Dimeric Mechanism*

One can conclude from the above computational results that both monomeric and trimeric Pd mechanisms can be ruled out since the former leads to *ortho*-selectivity and the latter has high activation barriers. The dimeric Pd–Pd and Pd–Ag models are more favorable than trimeric and monomeric Pd models in terms of activation energies and they successfully predict the experimentally observed *meta*-selectivity. Therefore, a deeper analysis on the origin of *meta*-selectivity for dimeric mechanism was performed.

As discussed in Sect. 2.3.1, in monomeric Pd model, Pd prefers to activate the *ortho*-C–H bond. Forcing the Pd to reach the remote *meta*-C–H bond will cause larger ring strain and distortion in the monomeric TS. The distortion energy of the substrate part of *meta*- and *ortho*-TS are 44.1 and 36.7 kcal/mol, respectively (Table 2.1). While in dimeric TS, the nitrile group and the activated C–H bond are bound to different Pd atoms (or Pd and Ag atoms). This special binding mode extends the size of the macrocyclic TS and directs Pd to get close to *meta*-C–H bond without introducing ring strain and torsion strain (Scheme 2.6). The distortion energy of the substrate part of *meta*- and *ortho*-TS are 33.3 and 37.7 kcal/mol, respectively (Table 2.2), demonstrating that the dimeric model significantly releases the distortion in *meta*-TS. In addition, the *meta*-TS is more flexible than *ortho*-TS in dimeric model. More low-energy *meta*-TS conformers are located in the conformational search.

Table 2.2 Distortion energy analysis of C–H activation TSs of dimeric models

Distortion energy (kcal/mol)	meta_TS1_c	ortho_TS1_c	para_TS1_c
E_{cat}	35.2	36.3	36.3
E_{sub}	33.3	37.7	35.6
E_{total}	68.5	74.0	71.9

Because the TS geometries for dimeric Pd–Pd and Pd–Ag mechanism are similar, we did structural analysis for dimeric Pd–Ag model to understand the origin of *meta*-selectivity. The most stable conformations of *ortho*-, *meta*-, and *para*-TS for dimeric Pd–Ag model are shown in Fig. 2.7. **meta_TS1_c** has a lower activation barrier than **ortho_TS1_c** by 3 kcal/mol. In monomeric TS, *meta*- and *para*-TS are destabilized by the torsion strain of $\psi 3$ (two large groups forms gauche conformation about the benzyl ether bond). While this unfavorable torsion strain is diminished in dimeric TSs because the larger sized macrocyclic TS allows the anti arrangement about $\psi 3$ in all three regioisomeric transition states. On the other hand, **ortho_TS1_c** is destabilized by the steric repulsion between the activated benzyl ring and the ether oxygen atom ($\psi 4 = 1°$) as well as the repulsion between the activated benzyl group and the acetate group (C–O distance is 2.84 Å). In **meta_TS1_c,** these repulsions are avoided since $\psi 4 = -44°$ and the C–O distance is 2.9 Å. In addition, the C-N-Ag angle is about 160° in **meta_TS1_c** and **ortho_TS1_c** which is close to the value of the angle (180°) in the most favorable conformation. While this angle distorts to be 135° in **para_TS1_c**.

In order to elucidate how the substrate distortion controls the regioselectivity, a distortion-interaction analysis was performed. As shown in Table 2.2, *meta*-TS has the lowest distortion energy. It is found all the TSs have similar distortion energies in catalyst part and the major difference is from the substrate part. The substrate in **ortho_TS1_c** and **para_TS1_c** suffers greater distortion leading to higher distortion energies of 5.5 and 3.4 kcal/mol than **meta_TS1_c**, respectively, further supporting that the substrate distortion in the C–H activation transition states controls the regioselectivity.

2.4   Summary

In this chapter, we studied the reaction mechanism and regioselectivity for the palladium acetate catalyzed remote *meta*-C–H activation and olefination reaction. Possible reaction mechanisms with monomeric $Pd(OAc)_2$, dimeric $Pd_2(OAc)_4$, dimeric $Pd–Ag(OAc)_3$, and trimeric $Pd_3(OAc)_6$ acting as active catalyst were investigated. Among these mechanisms, trimeric Pd model is ruled out due to the high activation barrier and the CMD mechanism with dimeric catalyst is found to be the most favorable mechanism. The frequently proposed monomeric $Pd(OAc)_2$ model has a higher activation barrier than dimeric models and leads to *ortho* product. Instead, the novel dimeric Pd–Pd and Pd–Ag mechanisms successfully reproduce the experimentally observed *meta*-selectivity. In the dimeric model, the nitrile group and the activated C–H are bound to two different Pd atoms of dimeric catalyst which forms a larger macrocycle. In the dimeric *meta*-TS, the large sized macrocycle direct the Pd to *meta*-C–H bond without inducing ring strain and torsion strain, thus promoting *meta*-C–H activation. This new model extends our knowledge about dimeric metal system as well as provides new ideas for the design of directing groups and new insights for the possible roles of additives used in

organic reactions. $Ag(OAc)_2$ is usually considered to act as oxidant, while our work suggests that silver salt may be involved in the active dimeric catalyst. After our work, Schaefer and co-workers [87] also proposed similar dimeric Pd–Pd and Pd–Ag models for Pd-catalyzed C–H activation reaction. Other works using dimeric catalyst or exploring the role of silver salts [88–92] have been reported recently.

References

1. Daugulis O, Do H-Q, Shabashov D (2009) Acc Chem Res 42:1074
2. He J, Wasa M, Chan KSL, Shao Q, Yu J-Q (2016) Chem Rev DOI: 10.1021/acs.chemrev.6b00622
3. Chen DYK, Youn SW (2012) Chem Eur J 18:9452
4. Shi G, Zhang Y (2014) Adv Synth Catal 356:1419
5. Godula K, Sames D (2006) Science 312:67
6. Goldberg KI, Goldman AS (eds) (2004) Activation and functionalization of C–H bonds, vol 885. American Chemical Society, Washington, DC
7. Bergman RG (2007) Nature 446:391
8. Zheng C, You S-L (2014) RSC advances 4:6173
9. Chen X, Engle KM, Wang D-H, Yu J-Q (2009) Angew Chem Int Ed 48:5094
10. Ackermann L, Vicente R, Kapdi AR (2009) Angew Chem Int Ed 48:9792
11. Labinger JA, Bercaw JE (2002) Nature 417:507
12. Arockiam PB, Bruneau C, Dixneuf PH (2012) Chem Rev 112:5879
13. Rousseau G, Breit B (2011) Angew Chem Int Ed 50:2450
14. Horino H, Inoue N (1981) J Org Chem 46:4416
15. Dupont J, Consorti CS, Spencer J (2005) Chem Rev 105:2527
16. Yang S, Li B, Wan X, Shi Z (2007) J Am Chem Soc 129:6066
17. Lyons TW, Sanford MS (2010) Chem Rev 110:1147
18. Tremont SJ (1984) Hayat ur. R J Am Chem Soc 106:5759
19. Wang G-W, Yuan T-T, Wu X-L (2008) J Org Chem 73:4717
20. Ano Y, Tobisu M, Chatani N (2011) Org Lett 14:354
21. Leow D, Li G, Mei T-S, Yu J-Q (2012) Nature 486:518
22. Dai H-X, Li G, Zhang X-G, Stepan AF, Yu J-Q (2013) J Am Chem Soc 135:7567
23. Lee S, Lee H, Tan KL (2013) J Am Chem Soc 135:18778
24. Wan L, Dastbaravardeh N, Li G, Yu J-Q (2013) J Am Chem Soc 135:18056
25. Bera M, Modak A, Patra T, Maji A, Maiti D (2014) Org Lett 16:5760
26. Tang R-Y, Li G, Yu J-Q (2014) Nature 507:215
27. Yang G, Lindovska P, Zhu D, Kim J, Wang P, Tang R-Y, Movassaghi M, Yu J-Q (2014) J Am Chem Soc 136:10807
28. Bag S, Patra T, Modak A, Deb A, Maity S, Dutta U, Dey A, Kancherla R, Maji A, Hazra A, Bera M, Maiti D (2015) J Am Chem Soc 137:11888
29. Bera M, Maji A, Sahoo SK, Maiti D (2015) Angew Chem Int Ed 54:8515
30. Deng Y, Yu J-Q (2015) Angew Chem Int Ed 54:888
31. Frost CG, Paterson AJ (2015) ACS Cent Sci 1:418
32. Li S, Ji H, Cai L, Li G (2015) Chem Sci 6:5595
33. Maji A, Bhaskararao B, Singha S, Sunoj RB, Maiti D (2016) Chem Sci 7:3147
34. Bakhmutov VI, Berry JF, Cotton FA, Ibragimov S, Murillo CA (2005) Dalton Trans, 1989
35. Ryabov AD, Sakodinskaya IK, Yatsimirsky AK (1958) J Chem Soc Dalon Trans 2629
36. Gomez M, Granell J, Martinez MJ (1998) Chem Soc Dalon Trans 37
37. Dick AR, Kampf JW, Sanford MS (2005) J Am Chem Soc 127:12790
38. Giri R, Chen X, Yu J-Q (2005) Angew Chem Int Ed 44:2112

39. Powers DC, Ritter T (2009) Nat Chem 1:302
40. Powers DC, Geibel MAL, Klein JEMN, Ritter T (2009) J Am Chem Soc 131:17050
41. Davies DL, Donald SMA, Macgregor SA (2005) J Am Chem Soc 127:13754
42. Balcells D, Clot E, Eisenstein O (2010) Chem Rev 110:749
43. García-Cuadrado D, Braga AAC, Maseras F, Echavarren AM (2006) J Am Chem Soc 128:1066
44. Rousseaux S, Gorelsky SI, Chung BKW, Fagnou K (2010) J Am Chem Soc 132:10692
45. Sun H-Y, Gorelsky SI, Stuart DR, Campeau L-C, Fagnou K (2010) J Org Chem 75:8180
46. Lafrance M, Fagnou K (2006) J Am Chem Soc 128:16496
47. Gorelsky SI, Lapointe D, Fagnou K (2011) J Org Chem 77:658
48. Chen X, Li J-J, Hao, X-S, Goodhue CE, Yu J-Q (2006) J Am Chem Soc 128: 78
49. Giri R, Lan Y, Liu P, Houk KN, Yu J-Q (2012) J Am Chem Soc 134:14118
50. Callear S, Spencer J, Patel H, Deadman J, Hursthouse M (2011) J Chem Crystallogr 41:523
51. Bercaw JE, Durrell AC, Gray HB, Green JC, Hazari N, Labinger JA, Winkler JR (2010) Inorg Chem 49:1801
52. Powers DC, Ritter T (2011) Acc Chem Res 45:840
53. Powers DC, Xiao DY, Geibel MAL, Ritter T (2010) J Am Chem Soc 132:14530
54. Cotton FA, Koshevoy IO, Lahuerta P, Murillo CA, Sanaú M, Ubeda MA, Zhao Q (2006) J Am Chem Soc 128:13674
55. Deprez NR, Sanford MS (2009) J Am Chem Soc 131:11234
56. Tan Y, Barrios-Landeros F, Hartwig JF (2012) J Am Chem Soc 134:3683
57. Sanhueza IA, Wagner AM, Sanford MS, Schoenebeck F (2013) Chem Sci 4:2767
58. Lafrance M, Gorelsky SI, Fagnou K (2007) J Am Chem Soc 129:14570
59. Gorelsky SI, Lapointe D, Fagnou K (2008) J Am Chem Soc 130:10848
60. Lapointe D, Fagnou K (2010) Chem Lett 39:1118
61. Gephart RT, McMullin CL, Sapiezynski NG, Jang ES, Aguila MJB, Cundari TR, Warren TH (2012) J Am Chem Soc 134:17350
62. Gaussian 09, Revision C.01, Frisch MJ, Trucks GW, Schlegel HB, Scuseria GE, Robb MA, Cheeseman JR Scalmani G, Barone V, Mennucci B, Petersson GA, Nakatsuji H, Caricato M, Li X, Hratchian HP, Izmaylov AF, Bloino J, Zheng G, Sonnenberg JL, Hada M, Ehara M, Toyota K, Fukuda R, Hasegawa J, Ishida M, Nakajima T, Honda Y, Kitao O, Nakai H, Vreven T, Montgomery JA Jr, Peralta JE, Ogliaro F, Bearpark M, Heyd JJ, Brothers E, Kudin KN, Staroverov VN, Kobayashi R, Normand J, Raghavachari K, Rendell A, Burant JC, Iyengar SS, Tomasi J, Cossi M, Rega N, Millam NJ, Klene M, Knox JE, Cross JB, Bakken V, Adamo C, Jaramillo J, Gomperts R, Stratmann RE, Yazyev O, Austin AJ, Cammi R, Pomelli C, Ochterski JW, Martin RL, Morokuma K, Zakrzewski VG, Voth GA, Salvador P, Dannenberg JJ, Dapprich S, Daniels AD, Farkas Ö, Foresman JB, Ortiz JV, Cioslowski J, Fox DJ (2010) Gaussian, Inc., Wallingford
63. Becke AD (1993) J Chem Phys 98:5648
64. Lee C, Yang W, Parr RG (1988) Phys Rev B 37:785
65. Becke AD (1993) J Chem Phys 98:1372
66. Stephens PJ, Devlin FJ, Chabalowski CF, Frisch MJ (1994) J Phys Chem 98:11623
67. Hay PJ, Wadt WR (1985) J Chem Phys 82:299
68. Roy LE, Hay PJ, Martin RL (2008) J Chem Theory Comput 4:1029
69. Ditchfield R, Hehre WJ, Pople JA (1971) J Chem Phys 54:724
70. Hariharan PC, Pople JA (1973) Theor Chim Acta 28:213
71. Krishnan R, Binkley JS, Seeger R, Pople JA (1980) J Chem Phys 72:650
72. Dolg M, Wedig U, Stoll H, Preuss H (1987) J Chem Phys 86:866
73. Andrae D, Häußermann U, Dolg M, Stoll H, Preuß H (1990) Theor Chim Acta 77:123
74. Zhao Y, Truhlar D (2008) Theor Chem Acc 120:215
75. Marenich AV, Cramer CJ, Truhlar DG (2009) J Phys Chem B 113:6378
76. Legault CY (2009) CYLView, 1.0b. Université de Sherbrooke, Canada. http://www.cylview.org
77. Biswas B, Sugimoto M, Sakaki S (2000) Organometallics 19:3895

78. Gómez M, Granell J, Martinez M (1997) Organometallics 16:2539
79. Tunge JA, Foresee LN (2005) Organometallics 24:6440
80. Ackermann L (2011) Chem Rev 111:1315
81. Zhang S, Shi L, Ding Y (2011) J Am Chem Soc 133:20218
82. Ess DH, Houk KN (2008) J Am Chem Soc 130:10187
83. Zhao Y, Truhlar DG (2011) Chem Phys Lett 502:1
84. Zhao Y, Truhlar DG (2009) J Chem Theory Comput 5:324
85. Zhao Y, Truhlar DG (2008) Acc Chem Res 41:157
86. See supporting information of ref. 93
87. Anand M, Sunoj RB, Schaefer HF (2014) J Am Chem Soc 136:5535
88. Hernando E, Villalva J, Martínez ÁM, Alonso I, Rodríguez N, Gómez Arrayás R, Carretero JC (2016) ACS Catal 6:6868
89. Senan AM, Qin S, Zhang S, Lou C, Chen Z, Liao R-Z, Yin G (2016) ACS Catal 6:4144
90. Whitaker D, Burés J, Larrosa I (2016) J Am Chem Soc 138:8384
91. Lee SY, Hartwig JF (2016) J Am Chem Soc 138:15278
92. Lotz MD, Camasso NM, Canty AJ, Sanford MS (2017) Organometallics 36:165
93. Yang Y-F, Cheng G-J, Liu P, Leow D, Sun T-Y, Chen P, Zhang X, Yu J-Q, Wu Y-D, Houk KN (2014) J Am Chem Soc 136:344

Chapter 3
# Mechanistic Studies on Pd(MPAA)-Catalyzed *Meta*- and *Ortho*-C–H Activation Reactions

Abstract This chapter presents a mechanistic study on Pd/MPAA (mono-N-protected amino acid)-catalyzed *meta*- and *ortho*-C–H activation reactions by a combined mass spectrometry and density functional theory (MS/DFT) method. A novel model for C–H activation was established which reveals the role of MPAA in promoting reactivity by favorably forming bidentate coordination with Pd and serving as the proton acceptor in C–H activation. It opens a new avenue for ligand and template design.

3.1 Introduction

The direct C–H bond activation provides an efficient methodology for constructing carbon–carbon or carbon–heteroatom bond. Improving selectivity and reactivity represents a longstanding goal in the field of C–H bond activation. In recent years, ligands have been widely applied in C–H activation due to their ability to modulate the activity and selectivity of transition metal catalysts. Recently, the Yu group developed mono-N-protected amino acid (MPAA) ligands which are successfully applied to various C–H activation reactions to improve reactivity and control selectivity. In 2012, they reported a remote *meta*-C–H activation directed by a nitrile-containing template (Eq. 3.1) [1]. With the assistance of the MPAA ligand, the template overrides the intrinsic electronic and steric biases achieving high *meta*-selectivity (up to 96%). The MPAA ligand was found to be essential to obtain high yield and regioselectivity. Similar reaction conditions were applied to ether directed *ortho*-C–H activation of substrate **3** (Eq. 3.2). MPAA ligand significantly improves the yield from 11% (without ligand) to 92% [2].

$$(3.1)$$

$$(3.2)$$
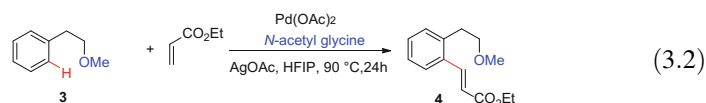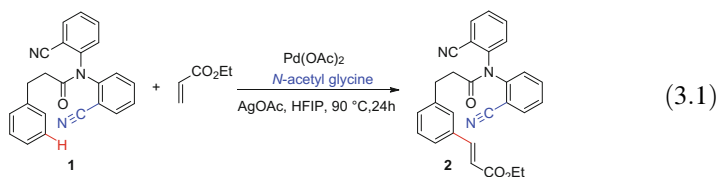
The Pd(OAc)$_2$/MPAA catalyst system has been successfully applied in a broad of reactions to improve yield, shorten the reaction time, promote regio- and enantio-selectivity. Reported reactions include carboxyl directed C–H alkylation [3], olefination [4] and arylation reactions [5], hydroxyl group directed C–H olefination reaction [6], nitrile group directed cross-coupling reaction [7], amide directed arylation [8], carboxyl directed C–H activation and C–O bond coupling reaction [9], silanol directed olefination [10], P(O)Ph$_2$ group directed olefination [11], intramolecular coupling reactions [12], and so forth. Chiral MPAA ligands are also employed to achieve asymmetric C–H activation [13–20] which will be discussed in the next chapter.

MPAA ligands are amino acid derivatives which are simple and commercially available or could be easily synthesized. The capability to improve reactivity and selectivity as well as readily availability make MPAA ligands to be especially appealing for C–H activation. The understanding on the mechanism of MPAA-assisted C–H activation and the effect of MPAA will provide important information for further development of new ligands and new reactions. In a computational study by Musaev and coworkers, they proposed a reaction mechanism involving N–H bond cleavage followed by C–H bond activation by an external base [21]. In the present work, we explored the Pd/MPAA-catalyzed *meta*-C–H and *ortho*-C–H activation reactions (Eqs. 3.1 and 3.2) by combined mass spectrometry and density functional theory (MS/DFT) method to reveal a novel model involving monomeric Pd(MPAA) species and understand the role of MPAA in promoting reactivity as well as controlling regioselectivity.

3.2 Experimental Methods and Computational Details

3.2.1 Experimental Methods

The experiments were performed with a SYNAPT G2-S HDMS instrument with an electrospray ion source [22]. The instrument is equipped with a quadruple mass filter after ion source for the selection of parent ions. In the collision-induced

dissociation (CID) experiment, the mass-selected ions enter an argon-filled linear ion trap in which argon is present at an approximate pressure of 8×10^{-3} mbar. After collision, the ions enter a time-of-flight (TOF) region for analysis.

For a given ion of interest, the elemental composition is confirmed by examination of the associated isotope envelopes in the source spectra and the structure is determined by analyzing the fragments obtained from collision induced dissociation experiments.

For ion generation, millimolar solutions of $Pd(OAc)_2$ (Energy Chemical, 99%), N-Ac-Glycine (Energy Chemical, 98%), and N-Boc-Glycine (Energy Chemical, 98%), respectively, in HPLC-grade methanol (Fisher-Scientific) or acetonitrile (Fisher-Scientific) were prepared. 1:1 mixed solutions of $Pd(OAc)_2$ and N-protected glycine (N-Ac-Glycine and N-Boc-Glycine) dissolved in methanol or acetonitrile were infused to the ESI at a flow rate of 3 µl min^{-1} via a syringe pump. Nitrogen was used as a nebulizing and desolvation gas at a source temperature of 100 °C.

3.2.2 Computational Details

All DFT calculations were carried out using Gaussian 09 program [23]. Geometry optimization was performed with B3LYP [24–27] hybrid density functional theory. LANL2DZ + f (1.472) [28, 29] basis set with ECP was used for palladium atom and 6-31G (d) [30, 31] basis set was used for other atoms. Frequency calculation for optimized structures was conducted at the same level of theory to verify the stationary points to be real minima (no imaginary frequency) or transition state (one imaginary frequency) and to obtain thermodynamic energy corrections. Single point energies were calculated at M06/SDD-6-311 ++G(d, p) [32–35] level and the solvent effect was evaluated by using SMD solvation model [36]. The relative energies with ZPE corrections and free energies (at 298.15 K) are in kcal/mol. RMSD values were calculated by chimera software [37] and RMSD counts all atoms which involved in model. 3D structures are displayed with CYLView [38].

3.3 Results and Discussion

3.3.1 Identifying Pd(MPAA)(Solvent) Complexes by ESI-MS

Mass spectrometry experiments were carried out to explore the coordination complexes generated from the trimeric precatalyst $[Pd(OAc)_2]_3$ and MPAA ligands. A 1:1 mixture of $Pd(OAc)_2$ and N-acetyl-glycine or N-Boc-glycine dissolved in methanol or acetonitrile was analyzed by electrospray ionization mass spectrometry (ESI-MS). No charged palladium acetate species were detected. Instead
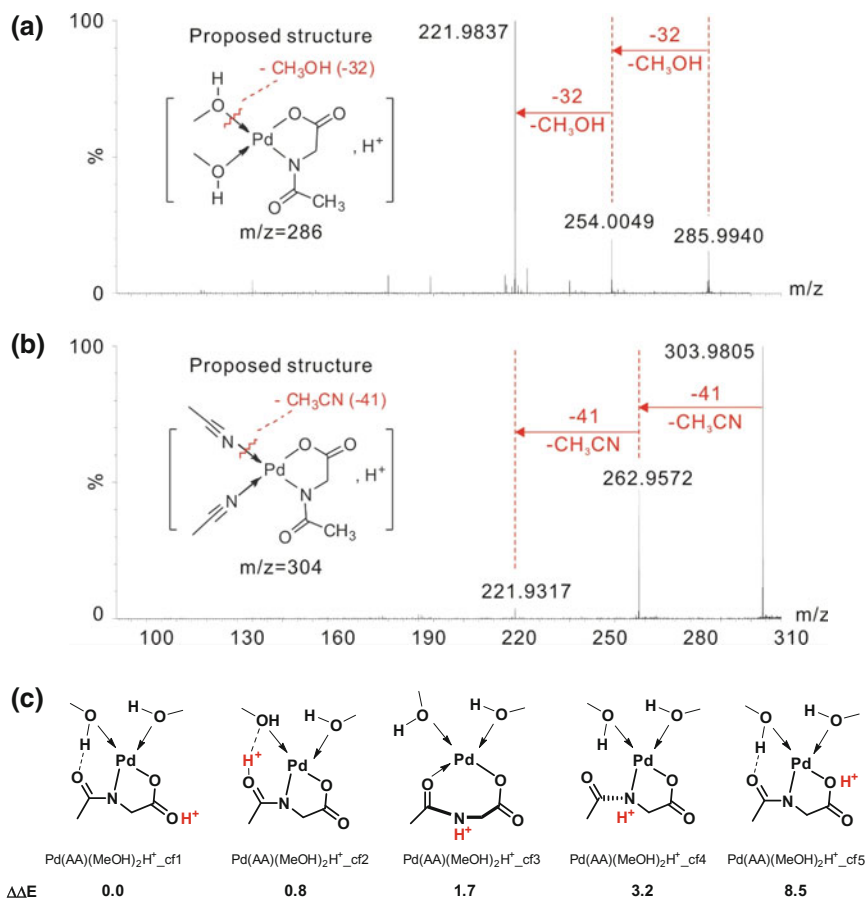
Fig. 3.1 Collision-induced dissociation (CID) mass spectra of **a** [Pd(*N*-Ac-Glycine)(CH$_3$OH)$_2$, H]$^+$ and **b** [Pd(*N*-Ac-Glycine)(CH$_3$CN)$_2$, H]$^+$. **c** Possible protonation positions for [Pd(*N*-Ac-Glycine)(CH$_3$OH)$_2$, H]$^+$ and corresponding relative energies (in kcal/mol). Reprinted with the permission from Ref. [58]. Copyright 2013 American Chemical Society

MPAA-coordinated palladium complexes, [Pd(N-Ac-Glycine)(solvent)$_2$, H]$^+$ and [Pd(*N*-Boc-Glycine)(solvent)$_2$, H]$^+$, (solvent = methanol or acetonitrile) were observed and confirmed by the isotope pattern in source spectra [39]. As shown in Fig. 3.1, two solvent molecules (methanol or acetonitrile) successively dissociate from [Pd(N-Ac-Glycine)(solvent)$_2$, H]$^+$ upon collision with argon gas in trap cell, suggesting that solvent molecules bind with Pd as neutral ligands. The dissociation of solvent molecules was also observed for [Pd(*N*-Boc-Glycine)(solvent)$_2$, H]$^+$ which confirms the solvent molecules acts as neutral ligands to coordinate with Pd (Fig. 3.2). The most possible protonation position is the carbonyl group of the carboxyl group or the N-protecting group of MPAA ligand as indicated by DFT
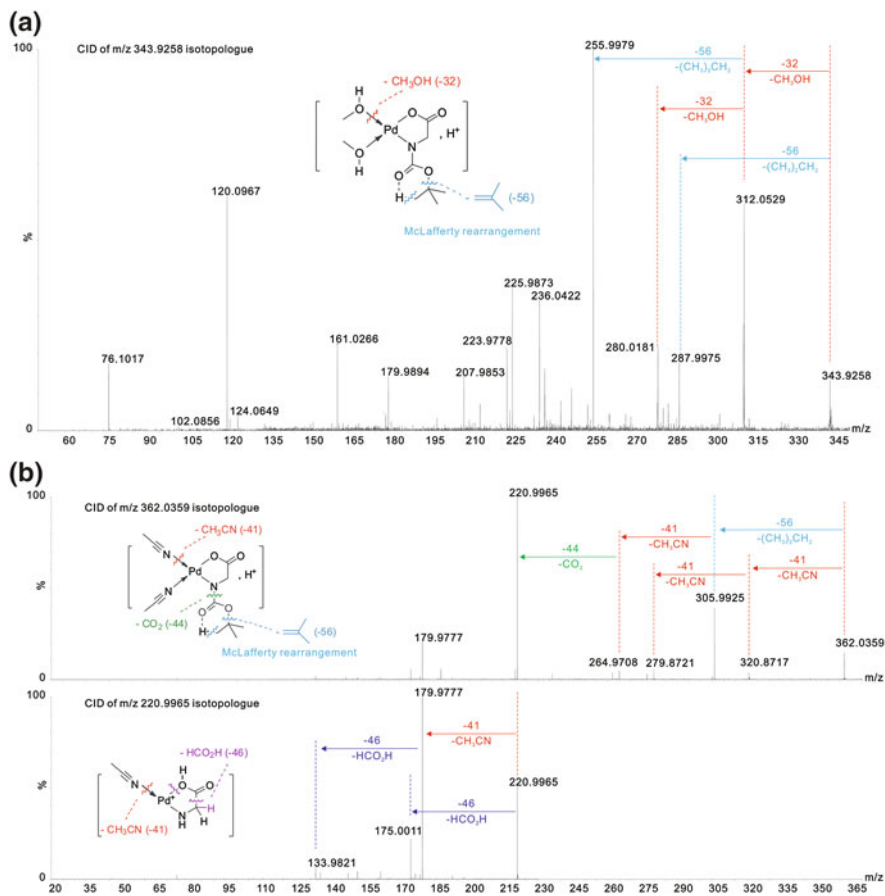
Fig. 3.2 Collision-induced dissociation (CID) mass spectra of **a** [Pd(N-Boc-Glycine)(CH₃OH)₂, H]⁺ and **b** [Pd(N-Boc-Glycine)(CH₃CN)₂, H]⁺

calculations (Fig. 3.1c). Thus the MS experiment and DFT calculation demonstrate that the deprotonated amino acid coordinates with Pd in a bidentate fashion. This provides the first experimental evidence that both acetates in Pd(OAc)₂ are replaced upon MPAA coordination. Previously, displacement of one of the acetates [21] or an acetylacetonate [40] from palladium(II) complexes by MPAA has been observed by NMR. Monomeric and dimeric Pd acetate species have been observed previously in a mixture of Pd(OAc)₂ and benzoquinone in AcOH/DMSO(1:1) [41]. Under the present reaction condition, palladium black was easily formed especially in methanol solvent which has a reductive property and [Pdₙ(CH₃CN)ᵐ]⁺ clusters were detected in acetonitrile solvent. These observations indicate that Pd(II) can be easily reduced to Pd(0) under the reaction condition used here and on the other hand it demonstrates that MPAA promotes formation of monomeric Pd(II) complexes even without an oxidant or excess AcOH.

3.3.2 Computational Studies on the Dissociation of Trimeric [Pd(OAc)₂]₃

3.3.2.1 Dissociation of Trimeric [Pd(OAc)$_2$]$_3$ to Monomeric Palladium Complex

MS experiments have detected the MPAA-coordinated monomeric Pd complex. Then we conducted computational studies to investigate the dissociation of trimeric [Pd(OAc)$_2$]$_3$ precatalyst. As illustrated in Fig. 3.3, the dissociation of [Pd(OAc)$_2$]$_3$ to form monomeric Pd(OAc)$_2$ complex is endergonic by 15.2 kcal/mol [42]. MPAA ligand may replace one acetate molecule and coordinate with Pd in monodentate mode leading to complex **5-B**. The energy required for the formation of **5-B** is 14.6 kcal/mol which is similar to that for **5-A**. The acetate could further activate the N–H bond of MPAA affording a dianionic ligand which binds with Pd

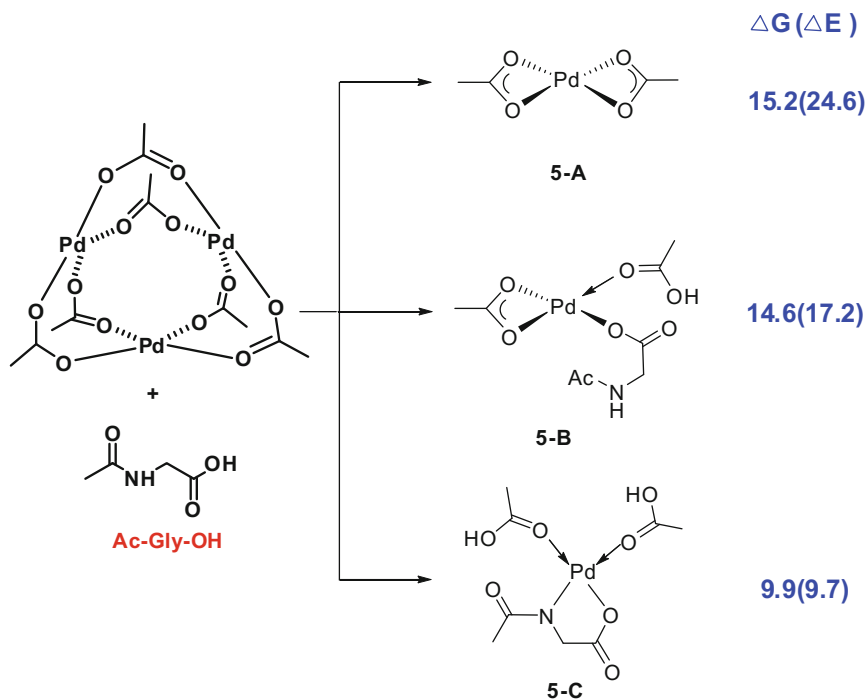**Fig. 3.3** Dissociation of the [Pd(OAc)$_2$]$_3$ trimer to form three possible active monomeric Pd catalysts, **5-A**, **5-B**, and **5-C**. In complexes **5-B** and **5-C**, MPAA is deprotonated by one or both of the acetates. Free energies (electronic energies in parentheses) with respect to [Pd(OAc)$_2$]$_3$ and Ac-Gly-OH are given in kcal/mol

in bidentate fashion to form complex **5-C**. The N–H deprotonation requires to overcome a low barrier of 16.8 kcal/mol with respect to $[Pd(OAc)_2]_3$ and the resulting intermediate **5-C** is 5.3 kcal/mol more stable than monomeric $Pd(OAc)_2$ (**5-A**). Here the normally unfavorable deprotonation of the N–H bond in amino acids is promoted by both the *N*-acyl group and the stronger binding of the deprotonated N with Pd, leading to a stable Pd complex with a dianionic bidentate MPAA ligand (**5-C**). This is in agreement with the above MS experimental observations of the stable Pd-MPAA complex.

3.3.2.2 Dissociation of Trimeric $[Pd(OAc)_2]_3$ to Dimeric Palladium Complex

The dissociation of trimeric $[Pd(OAc)_2]_3$ precatalyst to dimeric palladium complex was also studied. As shown in Fig. 3.4, the dissociation of $[Pd(OAc)_2]_3$ could lead to a four acetate molecules linked dimeric $[Pd(OAc)_2]_2$ complex (**Ac_dimer_Pd**) which is featured with a cage structure. This process is endergonic by 11.5 kcal/mol. The open structured dimeric $[Pd(OAc)_2]_2$ complex (**Ac_dimer_Pd_C**) with two acetate bridges has a higher energy than the cage structure by 6.5 kcal/mol. The MPAA-coordinated dimeric Pd complexes have also been investigated. The dimeric $Pd_2(OAc)_2(MPAA)_2$ has four possible conformations. In **AG_dimer_cf1**, two acetate groups act as bridge molecules to connect two Pd atoms and two MPAA ligands bind with different Pd atoms in bidentate mode, respectively. The energy of **AG_dimer_cf1** is 16.5 kcal/mol. In **AG_dimer_cf2**, two MPAA ligands and two acetate molecules act as bridges to link two Pd atoms forming a cage structure. The energy of **AG_dimer_cf2** is as high as 32.2 kcal/mol. In **AG_dimer_cf3** and **AG_dimer_cf4**, two acetate groups bind with two different Pd atoms, respectively, and two MPAA ligands link two Pd atoms. The difference between them lies in the binding mode of MPAA. The carboxyl group and the N-protecting group of MPAA coordinate with Pd in **AG_dimer_cf4**. The free energies for **AG_dimer_cf3** and **AG_dimer_cf4** are 49.4 and 35.6 kcal/mol, respectively.

Thus the $[Pd(OAc)_2]_2$ complex, **Ac_dimer_Pd** adopting a cage structure is the most stable dimeric palladium compound. **Ac_dimer_Pd** is more stable than monomeric $Pd(OAc)_2$ by 3.7 kcal/mol, but is still higher than the monomeric MPAA-coordinated complex **5-C** by 1.6 kcal/mol. On the other hand, dimeric **Ac_dimer_Pd** will form an open structure upon the binding of the substrate which is much higher than **5-C** in energy. Therefore, the formation of monomeric Pd (MPAA) complex is much more favorable than dimeric palladium complex at the present of MPAA ligand. In other words, MPAA ligand promotes the dissociation of trimeric Pd precatalyst to generate monomeric complex.
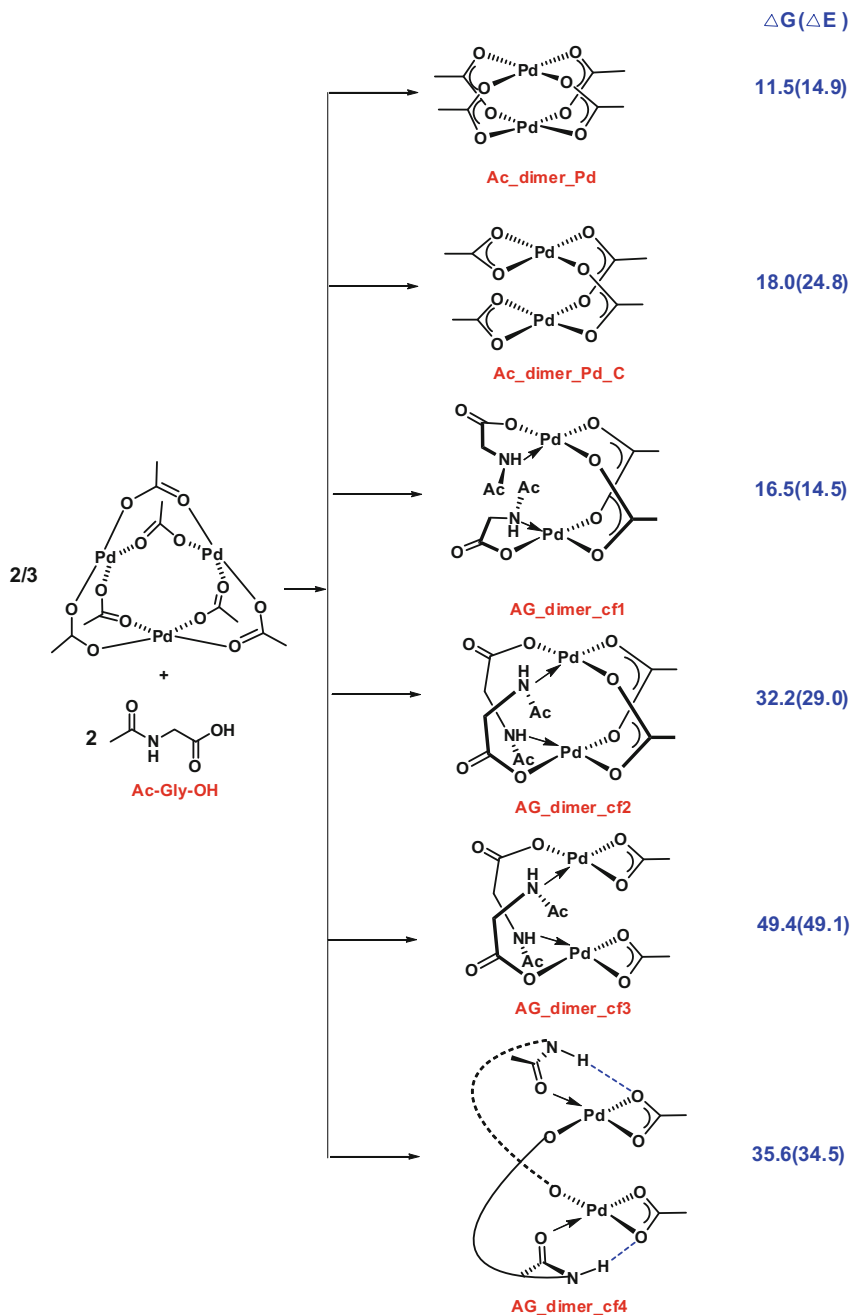
Fig. 3.4 Dissociation of the [Pd(OAc)$_2$]$_3$ trimer to form possible active dimeric Pd catalysts. Free energies (electronic energies in parentheses) with respect to [Pd(OAc)$_2$]$_3$ and Ac-Gly-OH are given in kcal/mol
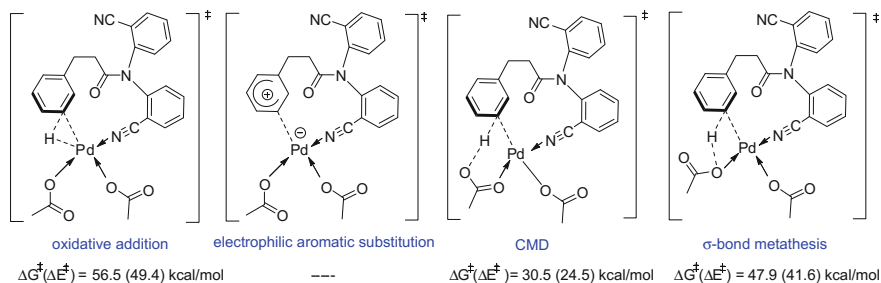
Fig. 3.5 Four conventionally proposed mechanisms for transition metal-catalyzed C–H activation and corresponding activation free energies (activation electronic energies)

3.3.3 C–H Activation Mechanism

3.3.3.1 Four Conventionally Proposed Mechanisms for C–H Activation

For transition-metal catalyzed C–H activation reactions, there are four most frequently proposed mechanisms [43] including oxidative addition, electronic aromatic substitution, concerted metalation and deprotonation (CMD) [44–49], and σ-bond metathesis. Computational studies on these four mechanisms for reaction 1 suggest that the reaction is unlikely to proceed through oxidative addition or σ-bond metathesis mechanisms since their barriers are about 50 kcal/mol (Fig. 3.5). Location of the transition state for electronic aromatic substitution pathway always led to the arene-coordinated intermediate, indicating this pathway is also unfavorable. The CMD pathway has the lowest activation barrier among these four pathways, which is consistent with previous studies on Pd-catalyzed C–H activation reactions [50, 51]. Thus, the following studies are based on CMD mechanism (Fig. 3.6).

3.3.3.2 Monomeric Palladium-Catalyzed C–H Activation

The C–H activation by monomeric palladium catalyst was investigated. We explored various CMD models of C–H activation of substrates **1** and **3** involving different counter-ions coordinated to the Pd and employing either the acetate (pathways A, B, D, E, and H) or the N-acyl carbonyl (pathway C) or the carboxyl group of MPAA (pathway F and G) to activate the C–H bond. The calculated activation barriers for these pathways are summarized in Table 3.1.

Pathway A represents the traditional Pd(OAc)$_2$ (**5-A**) catalyzed C–H activation in the absent of MPAA ligand. The activation barriers of pathway A for substrates **1** and **3** are 30.5 (*meta*-C–H bond) and 34.3 kcal/mol, respectively. In pathway B, the MPAA ligand coordinates with Pd in a monodentate way and acetate group abstracts the proton from the substrate. The activation barriers for pathway B are
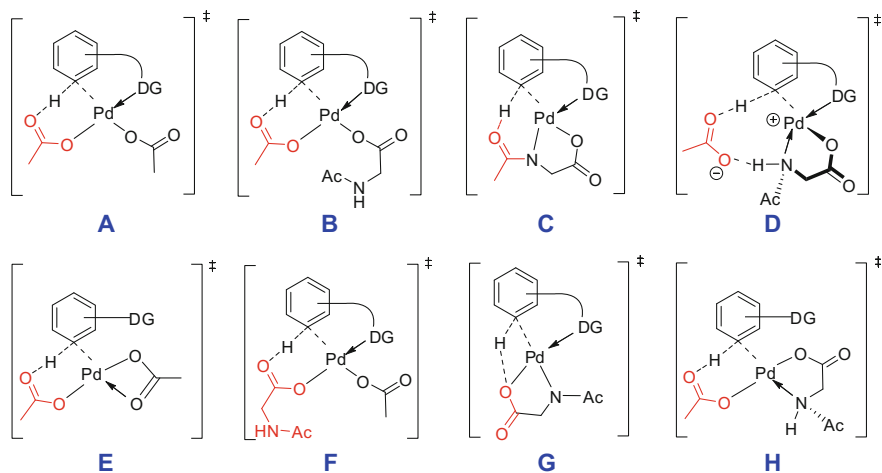
Fig. 3.6 Possible CMD models for monomeric palladium-catalyzed C–H activation of substrates **1** and **3**

Table 3.1 Calculated activation free energies (activation electronic energies) of pathways A-H (kcal/mol) for substrates **1** and **3**

		A	B	C	D	E	F	G	H
1	*ortho*	30.2 (23.3)	30.0 (23.6)	25.5 (21.4)	44.1 (33.6)	36.2 (31.1)	31.6 (25.0)		31.0 (21.7)
	meta	30.5 (24.5)	29.2 (22.2)	23.6 (20.8)	46.4 (37.0)	36.4 (33.0)	31.5 (24.3)	59.7 (56.7)	34.8 (26.8)
	para	31.3 (24.0)	29.1 (21.5)	24.1 (20.6)	41.0 (32.0)	33.8 (31.8)	32.0 (24.3)		33.5 (27.4)
3	*ortho*	34.3 (29.1)	33.0 (26.9)	28.9 (27.3)	43.8 (35.9)	34.2 (30.9)	34.9 (29.4)	65.9 (64.6)	33.5 (27.3)

similar to pathway A, suggesting the effect of monodentate MPAA ligand on the reactivity of palladium catalyst is negligible.

For bidentate MPAA-coordinated catalyst **5-C** (Pd(MPAA)(AcOH)$_2$), two AcOH molecules dissociate upon the coordination of the directing group and C–H bond of the substrate. Traditional CMD mechanism requires an acetate to deprotonate the C–H bond. While here all four coordination sites of the Pd are occupied by the ligand and the substrate, leaving no binding site for acetate. Employing an acetate to activate the C−H bond in this Pd(MPAA)(substrate) complex will require either dissociation of the MPAA ligand to form an unfavorable monodentate binding mode (pathway B) or outer-sphere deprotonation with an unbound acetate (Pathway D). Pathway D is highly unfavorable due to the charge separation in transition state and the activation barriers are more than 40 kcal/mol for both substrates **1** and **3**.

The present study proposed a novel C–H deprotonation mechanism involving the bidentate Pd(MPAA) catalyst (Pathway C). Instead of an external acetate, the

N-acyl group on the dianionic MPAA ligand acts as a base to deprotonate the C–H bond. The activation free energies for Pathway C are 23.6 and 28.9 kcal/mol for substrates **1** and **3**, respectively, which are 4–7 kcal/mol lower than those of Pathways A and B (Table 3.1). This is in agreement with the increased reactivities in the presence of MPAA ligand.

Other CMD models were also considered. Pathway E is the intermolecular C–H activation by Pd(OAc)$_2$ which has a higher (for substrate **1**) or similar (for substrate **3**) activation barrier than pathway A. Pathway F uses the monodentate MPAA as proton acceptor and has a similar activation energy with its counterpart, pathway B. In pathway G, the carboxyl group of bidentate MPAA acts as base to deprotonate the substrate. The carboxyl group of bidentate MPAA is a poor proton acceptor, and the calculated activation free energies for pathway G is about 60 kcal/mol. For pathway H, the dissociation of directing group releases a coordinating site for acetate group which eliminates the charge separation encountered by pathway D. But the activation barrier for pathway H is still much higher than that for pathway C.

3.3.3.3 Dimeric, Trimeric Pd, and Dimeric Pd–Ag Catalyzed C–H Activation

For substrate **1**, the long linker between the *meta*-C–H bond and nitrile group enables the C–H activation by dimeric Pd–Pd or Pd–Ag or trimeric Pd catalysts (Fig. 3.7) as proposed in Chap. 2. The calculated activation energies are summarized in Table 3.2. Both the [Pd(OAc)$_2$]$_2$ and [Pd(OAc)$_2$]$_3$ models have much higher activation barriers than model C. This could be explained by the dissociation of precatalyst (Figs. 3.3 and 3.4). The calculated dissociation energies have demonstrated that MPAA ligand promotes the dissociation of [Pd(OAc)$_2$]$_3$ and the formation of monomeric Pd(MPAA) complex is more favorable than the formation of [Pd(OAc)$_2$]$_2$. The activation energy for PdAg(OAc)$_3$ model is 25.2 kcal/mol (*meta*-C–H bond) which is lower than [Pd(OAc)$_2$]$_2$ and [Pd(OAc)$_2$]$_3$ models.

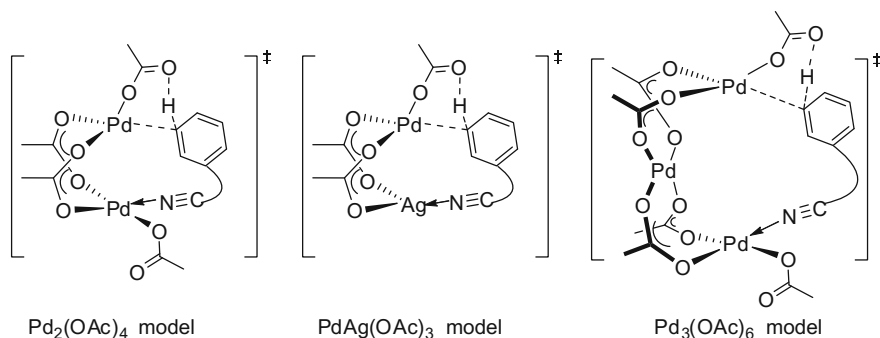Pd$_2$(OAc)$_4$ model   PdAg(OAc)$_3$ model   Pd$_3$(OAc)$_6$ model

Fig. 3.7 C–H bond activation of substrate **1** catalyzed by dimeric Pd–Pd, Pd–Ag, and trimeric Pd catalysts

Table 3.2 Calculated activation free energies (activation electronic energies) of dimeric Pd–Pd, Pd–Ag, and trimeric Pd-catalyzed C–H activation of substrates **1**. Energies are given in kcal/mol

		$[Pd(OAc)_2]_2$ model	$PdAg(OAc)_3$ model	$[Pd(OAc)_2]_3$ model
1	*ortho*	34.2 (22.2)	24.0 (11.0)	42.5 (27.4)
	meta	35.0 (23.8)	25.2 (12.9)	52.3 (35.9)
	para	33.3 (22.5)	25.7 (12.1)	49.2 (33.9)

However, the $PdAg(OAc)_3$ model prefers *ortho*-C–H activation and could not reproduce the experimentally observed *meta*-selectivity.

3.3.3.4 Summary for C–H Activation Mechanisms

In the present work, various monomeric palladium, dimeric palladium, dimeric palladium-silver, and trimeric palladium catalysts catalyzed C–H activation mechanisms were investigated. Among these mechanisms, the new model C proposed in this work is the most favorable mechanism.

To understand why pathway C is more favorable than other mechanisms and the origin of the promotion effects of MPAA on reactivity, an energy decomposition analysis was conducted for the representative models (models A, B, and C). As shown in Fig. 3.8, the process of palladium acetate catalyzed C–H activation can be divided into three steps: dissociation of $[Pd(OAc)_2]_3$ precatalyst to active catalyst, binding of substrate to the catalyst, and the C–H bond cleavage. Therefore, the
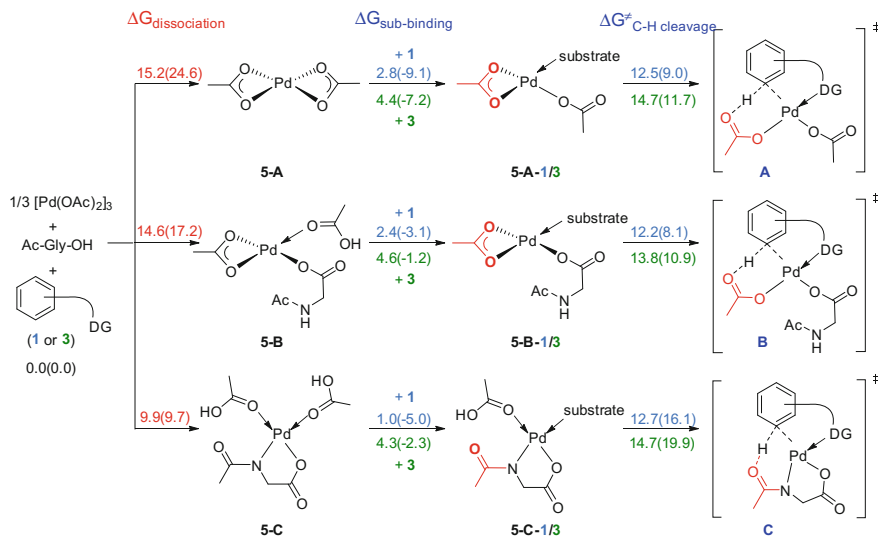
Fig. 3.8 Energy decomposition analysis for models A, B and C

activation barrier for C–H bond activation is composed of the dissociation energy from precatalyst to active catalyst ($\Delta G_{dissociation}$), the binding energy of substrate ($\Delta G_{sub\text{-}binding}$) and the energy required for C–H bond cleavage ($\Delta G_{C\text{–}H\ cleavage}$). Figure 3.8 demonstrates that the binding of substrate to catalysts **5-A**, **5-B**, and **5-C** ($\Delta G_{sub\text{-}binding}$) needs similar free energies for substrates **1** and **3**, respectively. Analogously, the activation free energies for C–H bond cleavage ($\Delta G_{C\text{–}H\ cleavage}$) are comparable for substrate coordinated complexes. The main differences of these three pathways lie in the dissociation energy ($\Delta G_{dissociation}$). The formation of catalyst **5-C** is much more favorable than **5-A** and **5-B**. Thus the preference of pathway C and the promotion effect of MPAA ligand on reactivity can be attributed to the stabilization of monomeric palladium species by bidentate MPAA ligand which decreases the dissociation energy and lowers the whole barrier for C–H activation. This also explains the preference of pathway C over the dimeric Pd-Pd, Pd-Ag and trimeric Pd mechanisms in the presence of MPAA ligand.

Similar effects have been found in strong σ-donor ligand accelerated C–H activations in which the strong binding ligand may also stabilize the active monomeric palladium catalyst leading to improved reactivity [52]. However, for substrates with weak binding affinity neutral σ-chelating ligand, e.g., pyridine, may occupy all available binding sites of palladium which deactivates palladium catalyst [53]. Here as a dianionic ligand, MPAA ligand replaces two carboxylate anions to occupy two coordinate sites, and thus does not compete with substrate coordination. This advantage enables MPAA ligand to facilitate C–H activation of substrates with weakly coordinating directing groups.

The C–H activation with Pd(MPAA) complex also benefits from the greater basicity of the *N*-acyl carbonyl (i.e., an amidate) than acetate (e.g., pathways A and B). The smaller bite angle of the MPAA ligand compared to two acetate ligands also leads to less steric hindrance for coordination of the directing group. The planar geometry of the dianionic MPAA ligand places the *N*-acyl group in a favorable co-planar orientation to deprotonate the C–H bond while maintaining the square planar geometry of the palladium (see Fig. 3.10 for 3D structure).

3.3.4   Potential Energy Surface for Reaction 1

The reaction process and energy profile of reaction 1 is shown in Fig. 3.9. The reaction initiates from the dissociation of trimeric [Pd(OAc)$_2$]$_3$ precatalyst to monomeric palladium catalyst. The binding of MPAA ligand to palladium leads to complex **int0** which undergoes N–H bond activation to generate dianionic MPAA coordinated complex **int1**. The activation free energy for N–H bond cleavage is 16.8 kcal/mol. Then the substrate coordinates with palladium and MPAA activates the C–H bond of the substrate to generate the cyclopalladium complex **int3**. The
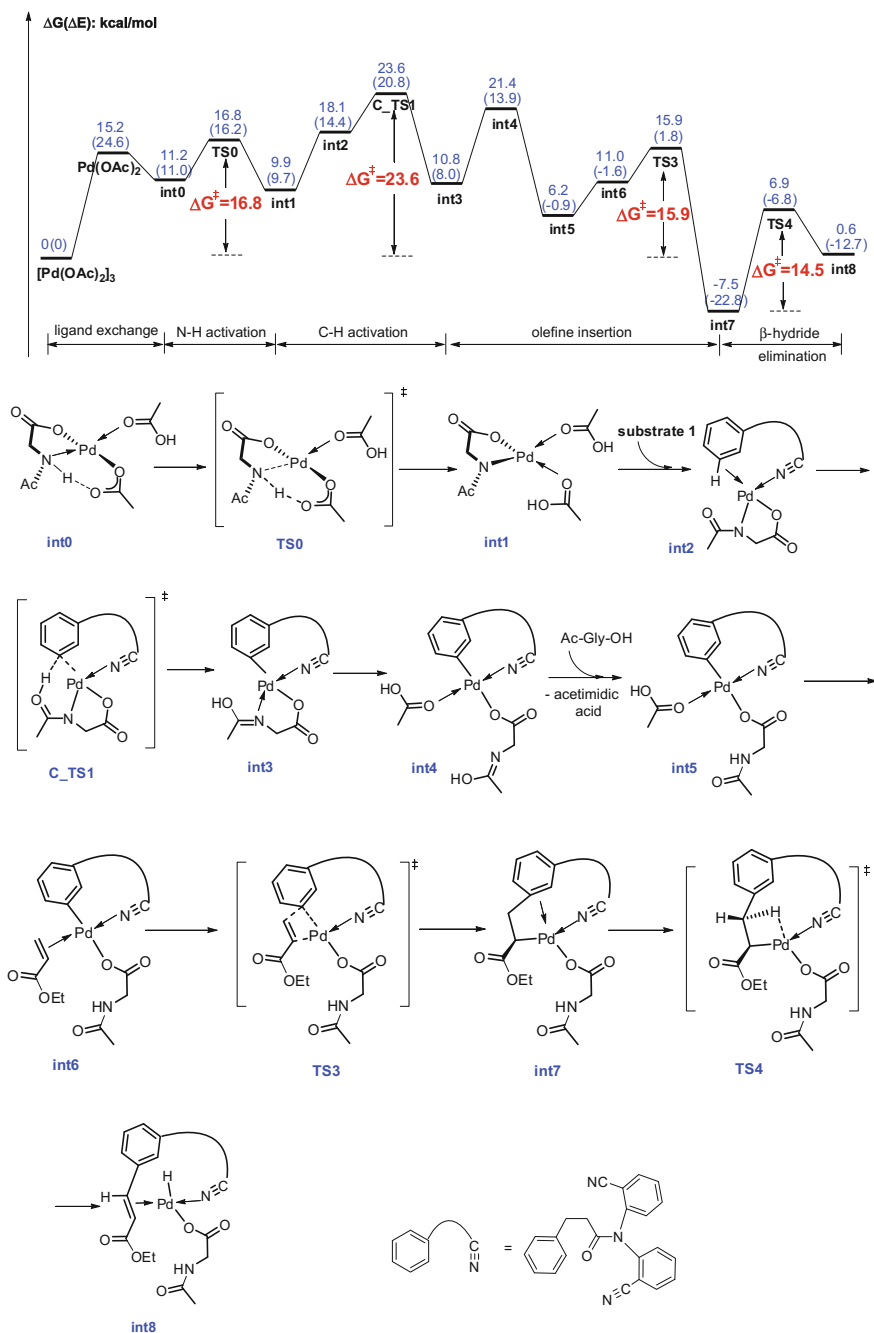
Fig. 3.9 Energy profile of reaction 1 and its reaction process

activation barrier of C–H bond activation is 23.6 kcal/mol. After accepting the proton from substrate, MPAA ligand converts to acetimidic acid which could easily isomerize to amino acid and regenerate MPAA ligand. Following the C–H activation and several ligand exchange steps, olefin insertion and β-hydride elimination leads to olefination product. Activation free energies for olefin insertion and β-hydride elimination steps are 15.9 and 14.5 kcal/mol, respectively. Finally, the product dissociates from the catalyst and the oxidation of Pd(0) regenerates Pd(II) catalyst. It is found that the C–H bond activation is the rate-determining step [50, 54, 55] and the regioselectivity-determining step.

3.3.5 Origin of Meta-Selectivity

After determining the role of the MPAA ligand on reactivity, we investigate the origin of regioselectivity. For substrate **3**, the experimentally observed *ortho*-selectivity can be easily understood since the substrate can form six-membered cyclopalladium ring to activate *ortho*-C–H bond while the short linker apparently prevents the Pd from accessing the *meta*- and *para*-C–H bond. Therefore, we focused on the origin of the unique *meta*-selectivity in the reaction with substrate **1**.

A systematic conformational search located 9, 9, and 5 conformers for *ortho*-, *meta*-, and *para*-C–H activation transition state, respectively. The most stable *ortho*-, *meta*-, and *para*- TS conformations in pathway C are depicted in Fig. 3.10. The transition state leading to the *meta*-product is the most stable TS, which is in agreement with experiment.

To unveil the origin of *meta*-selectivity, a model TS without a linker between benzene and acetonitrile was constructed. Without the constraint of the linker, the substrate in **6-TS** could adopt the most favorable conformation to interact with MPAA ligand and Pd catalyst. The structure of **6-TS** is perfectly planar with Pd1, C2, O3, and C4 atoms in the same plane ($\alpha1_{(Pd1-C2-O3-C4)} = 0°$). This places the *N*-acyl group to an ideal orientation to deprotonate the benzene C–H bond. The benzene plane is perpendicular to the coordination plane of Pd ($\alpha2 = 90°$) in order to achieve the optimum orbital overlap between the π orbital of benzene and the *d* orbital of the Pd. Here, we compared the *ortho*-, *meta*-, and *para*-TS with the model TS and found *meta*-**7-TS** is the closest structure to **6-TS**. The planarity of the *N*-acyl group and the perpendicular orientation of the benzene ring are reasonably well preserved in *meta*-**7-TS** ($\alpha1 = 0°$ and $\alpha2 = 88°$). Slight deviation from this optimum geometry was observed in *para*-**7-TS** ($\alpha1 = -6°$ and $\alpha2 = 84°$). More significant distortion is observed in *ortho*-**7-TS** ($\alpha1 = 17°$ and $\alpha2 = 81°$). Superimposing these three TSs with model TS reveals RMSDs (Root Mean Square Deviation, RMSD) of 0.10, 0.19, and 0.42 Å for the *meta*-, *para*-, and *ortho*-TS, respectively, indicating that the *meta*-TS mimics the non-constrained model best. On the hand, it is well known that the C–C single bond adjacent to carbonyl (i.e., O5 = C6-C7-C8) prefers a syn-planar geometry ($\alpha3 = 0°$). The dihedral angle $\alpha3$ is $-7°$ in reactant **1**, and it increases to $-27°$, $-42°$, and $-60°$ in *meta*-**7-TS**, *para*-

6-TS

meta-**7-TS**

23.6 (20.8)

para-**7-TS**
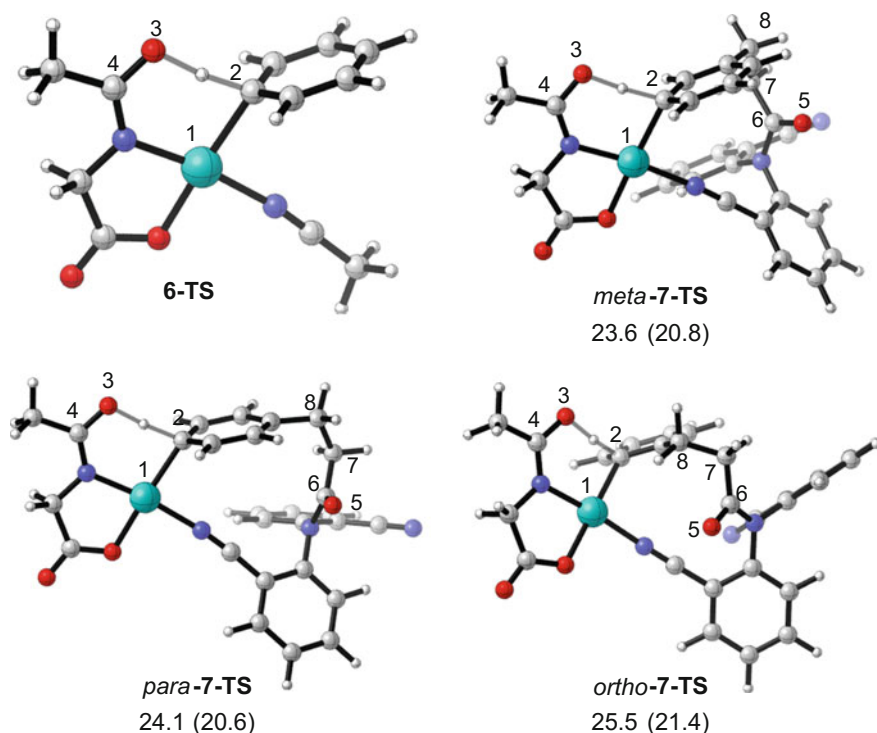
24.1 (20.6)

ortho-**7-TS**

25.5 (21.4)

Fig. 3.10 Model transition state **6-TS** and the most stable conformations for *meta-*, para-, and *ortho*-TS of substrate **1** in pathway C. Activation free energies (activation electronic energies) are given in kcal/mol. Reprinted with the permission from Ref. [58]. Copyright 2013 American Chemical Society

7-TS, and *ortho*-**7-TS**, respectively. Therefore, the template is less distorted in *meta*-TS while the template suffers stronger distortion in *para*- and *ortho*-TS.

3.3.6 Substituents Effects of MPAA Ligand

According to the proposed model C, the electronic and steric effects of substituents R^1 and R^2 on MPAA ligand could affect the electrophilicity of palladium and the basicity of N-protecting group, hence influencing the reactivity of C–H bond activation. In accordance with this prediction based on model C, the yield decreases from 95 to 10% when replacing the acetyl group with a tert-butyl group for R^1. The calculated activation barrier of C–H bond activation with the Boc-Gly-OH is 2.7 kcal/mol higher than with the Ac-Gly-OH ligand, in agreement with experimental observation. The tert-butoxyl group of Boc-Gly-OH ligand is electron-withdrawing group which decreases the basicity of the carbonyl group of
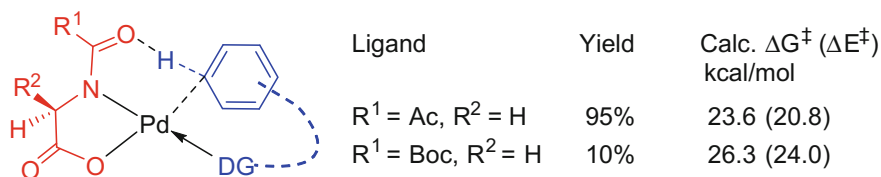
Ligand	Yield	Calc. $\Delta G^{\ddagger}$ ($\Delta E^{\ddagger}$) kcal/mol
R^1 = Ac, R^2 = H	95%	23.6 (20.8)
R^1 = Boc, R^2 = H	10%	26.3 (24.0)

Fig. 3.11 Effects of substituents on the MPAA ligand. Reprinted with the permission from Ref. [58]. Copyright 2013 American Chemical Society

N-protecting and results in a higher activation barrier. The agreement between theory and experiment further supports the proposed mechanism. In addition, by properly introducing effective R^2 groups on the rigid chelating MPAA skeleton, it is possible to create a chiral environment for asymmetric C–H bond activation [13–20]. The chiral MPAA ligand assisted asymmetric C–H activation will be discussed in the next chapter.

A long linker between coordinating group and active site of C–H bond enables substrates to achieve remote functionalization. Based on the monomeric transition state model, the linker in substrates can be adjusted to obtain unusual selecitivies in arenes functionalization by remote C–H bond activation [56, 57] (Fig. 3.11).

3.4   Summary

In summary, the mono-N-protected amino acid (MPAA)-assisted C–H activation and olefination reactions have been studied by combined mass spectrometry and computational methods. The key intermediate Pd(MPAA) complex was captured by MS. It is the first time to observe the dianionic bidentate MPAA coordinated Pd complex by experiment. Our study uncovered a novel CMD mechanism in which the MPAA ligand acts as bidentate ligand and the N-protecting group of MPAA acts as proton acceptor. This innovative model successfully explained the promoting effects of MPAA ligand on reactivity and the origin of regioselectivity. It is found that MPAA promotes the dissociation of trimeric palladium precatalyst to form active monomeric catalyst and thus decreases the barrier for C–H bond activation, leading to improved reactivity. The model with the direct involvement of dianionic MPAA as the proton acceptor in C–H activation opens new avenues for ligand and template design. For example, it is attractive to develop other kinds of ligands which could act as both bidentate ligand and base. Recently, the Yu group designed a new hydroxamic acid ester ligand in which the carboxyl group of MPAA is substituted by hydroxamic acid ester and applied this new ligand for asymmetric C–H activation [8]. In addition, currently MPAA ligand is employed along with palladium catalyst in most of the cases, the development of application of MPAA ligand with other transition metals may bring new catalytic properties

and new reactions. On the other hand, based on the monomeric transition state model, the linker in substrates can be adjusted to accomplish site-selective functionalization of remote C–H bonds in various arenes and heteroarenes.

References

1. Leow D, Li G, Mei T-S, Yu J-Q (2012) Nature 486:518
2. Li G, Leow D, Wan L, Yu J-Q (2013) Angew Chem Int Ed 52:1245
3. Thuy-Boun PS, Villa G, Dang D, Richardson P, Su S, Yu J-Q (2013) J Am Chem Soc 135:17508
4. Wang D-H, Engle KM, Shi B-F, Yu J-Q (2010) Science 327:315
5. Engle KM, Thuy-Boun PS, Dang M, Yu J-Q (2011) J Am Chem Soc 133:18183
6. Lu Y, Wang D-H, Engle KM, Yu J-Q (2010) J Am Chem Soc 132:5916
7. Wan L, Dastbaravardeh N, Li G, Yu J-Q (2013) J Am Chem Soc 135:18056
8. Xiao K-J, Lin DW, Miura M, Zhu R-Y, Gong W, Wasa M, Yu J-Q (2014) J Am Chem Soc 136:8138
9. Novák P, Correa A, Gallardo-Donaire J, Martin R (2011) Angew Chem Int Ed 50:12236
10. Huang C, Chattopadhyay B, Gevorgyan V (2011) J Am Chem Soc 133:12406
11. Wang H-L, Hu R-B, Zhang H, Zhou A-X, Yang S-D (2013) Org Lett 15:5302
12. Meng X, Kim S (2013) J Org Chem 78:11247
13. Xiao K-J, Chu L, Chen G, Yu J-Q (2016) J Am Chem Soc 138:7796
14. Du Z-J, Guan J, Wu G-J, Xu P, Gao L-X, Han F-S (2015) J Am Chem Soc 137:632
15. Xiao K-J, Chu L, Yu J-Q (2016) Angew Chem Int Ed 55:2856
16. Peng HM, Dai L-X, You S-L (2010) Angew Chem Int Ed 49:5826
17. Shi Y-C, Yang R-F, Gao D-W, You S-L (2013) Beilstein J Org Chem 9:1891
18. Evans DA, Michael FE, Tedrow JS, Campos KR (2003) J Am Chem Soc 125:3534
19. Gao D-W, Shi Y-C, Gu Q, Zhao Z-L, You S-L (2012) J Am Chem Soc 135:86
20. Marson A, van Oort AB, Mul Wilhelmus P (2002) Eur J Inorg Chem 2002:3028
21. Musaev DG, Kaledin A, Shi B-F, Yu J-Q (2011) J Am Chem Soc 134:1690
22. Pringle SD, Giles K, Wildgoose JL, Williams JP, Slade SE, Thalassinos K, Bateman RH, Bowers MT, Scrivens JH (2007) Int J Mass Spectrom 261:1
23. Gaussian 09, Revision C.01, Frisch MJ, Trucks GW, Schlegel HB, Scuseria GE, Robb MA, Cheeseman JR, Scalmani G, Barone V, Mennucci B, Petersson GA, Nakatsuji H, Caricato M, Li X, Hratchian HP, Izmaylov AF, Bloino J, Zheng G, Sonnenberg JL, Hada M, Ehara M, Toyota K, Fukuda R, Hasegawa J, Ishida M, Nakajima T, Honda Y, Kitao O, Nakai H Vreven T, Montgomery JA Jr, Peralta JE, Ogliaro F, Bearpark M, Heyd JJ, Brothers E, Kudin KN, Staroverov VN, Kobayashi R, Normand J, Raghavachari K, Rendell A, Burant JC, Iyengar SS, Tomasi J, Cossi M, Rega N, Millam NJ, Klene M, Knox JE, Cross JB, Bakken V, Adamo C, Jaramillo J, Gomperts R, Stratmann RE, Yazyev O, Austin AJ, Cammi R, Pomelli C, Ochterski JW, Martin RL, Morokuma K, Zakrzewski VG, Voth GA, Salvador P, Dannenberg JJ, Dapprich S, Daniels AD, Farkas Ö, Foresman JB, Ortiz JV, Cioslowski J, Fox DJ (2010) Gaussian, Inc., Wallingford
24. Becke AD (1993) J Chem Phys 98:5648
25. Lee C, Yang W, Parr RG (1988) Phys Rev B 37:785
26. Becke AD (1993) J Chem Phys 98:1372
27. Stephens PJ, Devlin FJ, Chabalowski CF, Frisch MJ (1994) J Phys Chem 98:11623
28. Hay PJ, Wadt WR (1985) J Chem Phys 82:299
29. Roy LE, Hay PJ, Martin RL (2008) J Chem Theory Comput 4:1029
30. Ditchfield R, Hehre WJ, Pople JA (1971) J Chem Phys 54:724
31. Hariharan PC, Pople JA (1973) Theor Chim Acta 28:213

32. Krishnan R, Binkley JS, Seeger R, Pople JA (1980) J Chem Phys 72:650
33. Dolg M, Wedig U, Stoll H, Preuss H (1987) J Chem Phys 86:866
34. Andrae D, Häußermann U, Dolg M, Stoll H, Preuß H (1990) Theor Chim Acta 77:123
35. Zhao Y, Truhlar D (2008) Theor Chem Acc 120:215
36. Marenich AV, Cramer CJ, Truhlar DG (2009) J Phys Chem B 113:6378
37. Pettersen EF, Goddard TD, Huang CC, Couch GS, Greenblatt DM, Meng EC, Ferrin, TE (2004) UCSF Chimera–a visualization system for exploratory research and analysis. J Comput Chem 25:1605
38. Legault CY (2009) CYLView 1.0b. Université de Sherbrooke, Canada. http://www.cylview.org
39. See Figure S1–S4 of the supporting information in ref. 58
40. Navarro R, García J, Urriolabeitia EP, Cativiela C, Diaz-de-Villegas MD (1995) J Organomet Chem 490:35
41. Vasseur A, Harakat D, Muzart J, Le Bras J (2012) J Org Chem 77:5751
42. The calculated dissociation free energy in the present chapter is different from that in chapter 2 because they were calculated at different temperatures
43. Ackermann L (2011) Chem Rev 111:1315
44. Lapointe D, Fagnou K (2010) Chem Lett 39:1118
45. Biswas B, Sugimoto M, Sakaki S (2000) Organometallics 19:3895
46. Gómez M, Granell J, Martinez M (1997) Organometallics 16:2539
47. Gomez M, Granell J, Martinez MJ (1998) Chem Soc Dalon Trans 37
48. Davies DL, Donald SMA, Macgregor SA (2005) J Am Chem Soc 127:13754
49. Tunge JA, Foresee LN (2005) Organometallics 24:6440
50. Zhang S, Shi L, Ding Y (2011) J Am Chem Soc 133:20218
51. Giri R, Lan Y, Liu P, Houk KN, Yu J-Q (2012) J Am Chem Soc 134:14118
52. (a) Steinhoff BA, Guzei IA, Stahl SS (2004) J Am Chem Soc 126:11268 (b) Emmert MH, Cook AK, Xie YJ, Sanford MS (2011) Angew Chem Int Ed 50:9409 (c) Kubota A, Emmert MH, Sanford MS (2012) Org Lett 14:1760
53. Zhang Y-H, Shi B-F, Yu J-Q (2009) J Am Chem Soc 131:5072
54. Chaumontet M, Piccardi R, Audic N, Hitce J, Peglion J-L, Clot E, Baudoin O (2008) J Am Chem Soc 130:15157
55. Rousseaux S, Gorelsky SI, Chung BKW, Fagnou K (2010) J Am Chem Soc 132:10692
56. Tang R-Y, Li G, Yu J-Q (2014) Nature 507:215
57. Bag S, Patra T, Modak A, Deb A, Maity S, Dutta U, Dey A, Kancherla R, Maji A, Hazra A, Bera M, Maiti D (2015) J Am Chem Soc 137:11888
58. Cheng G-J, Yang Y-F, Liu P, Chen P, Sun T-Y, Li G, Zhang X, Houk KN, Yu J-Q, Wu Y-D (2014) J Am Chem Soc 136:894

Chapter 4
Mechanistic Studies on Pd(MPAA)-Catalyzed Enantioselective C–H Activation Reactions

Abstract A combined ion-mobility mass spectrometry (IM-MS) and DFT study has been carried out to investigate Pd/MPAA(mono-N-protected amino acid)-catalyzed direct asymmetric C–H activation reactions of several prochiral substrates. The IM-MS experiments reveal that the activation of C–H bond can be achieved in Pd^{II}(MPAA)(substrate) complex which supports that the N-protecting group acts as proton acceptor. DFT studies lead to the establishment of a chirality relay model which successfully explains the enantioselectivity for all the relevant reactions studied. The enantioselectivity originates from the rigidity of the bidentate MPAA and rigid coordination of the substrate. The effect of bulkiness of the N-protecting group on enantioselectivity is also discussed.

4.1 Introduction

The direct functionalization of inert C–H bonds [1–16] provides a powerful method for organic synthesis which has attracted extensive attention. Many efforts have been devoted to this research area, while enantioselective C–H activation still remains as one of the challenges in this field [17–20]. In recent years, Yu and coworkers developed a strategy that employs chiral monoprotected amino acids (MPAA) as ligands [21–23] to realize enantioselective C–H activation. This method has been successfully applied to desymmetric C–H functionalization of prochiral

substrates and enantioselective C–H functionalization of racemic compound via kinetic resolution [24–38]. An example is shown in Eq. 4.1.


$$(4.1)$$
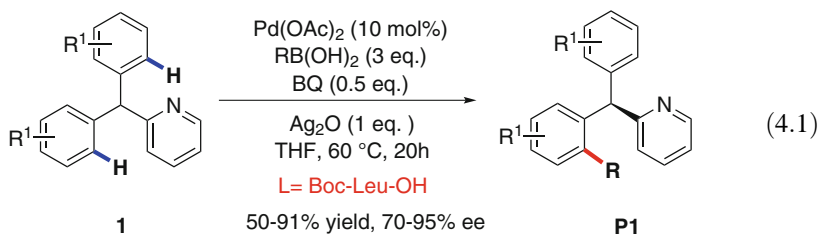
The prochiral substrate **1** contains two identical aromatic rings which have same chemical reactivities and steric environments, imposing great challenges on differentiating them to achieve enantioselective C–H activation. In 2008, the Yu group successfully realized an effective desymmetric C–H activation/C–C coupling reaction of prochiral substrate **1** by using chiral N-protected amino acids as ligand [35]. The nature of N-protecting group of the MPAA ligand has a significant influence on the enantioselectivity and reactivity. As shown in Scheme 4.1, using the mono-N-protected amino acid Boc-Val-OH (**L1**) as ligand leads to a good yield and *e.e.* while the unprotected amino acid **L2** suppresses the reactivity. The Piv-protected amino acid ligand, **L3**, results in a poor enantioseletivity. The use of ester (**L4**) and diprotected amino acids, **L5** and **L6** were found to afford rather poor enantioselectivity.
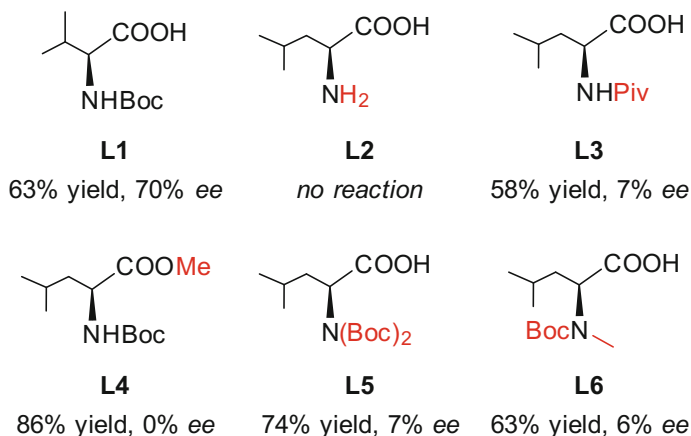

Scheme 4.1 Selected results of ligand screening experiment for Pd/MPAA-catalyzed desymmetric C–H activation/C–C coupling reaction Eq. 4.1

After this pioneer work, Pd(OAc)$_2$/MPAA catalyst system was widely employed to enantioselective C–H activation reactions. The enantioselective C–H activation of diphenylacetic acids was accomplished using Boc-Ile-OH as chiral ligand. With PhI(OAc)$_2$ as oxidant and KOAc as base, the enantioselective C–H activation/C–O bond formation reaction affords chiral benzofuranones with excellent *e.e.* (**p2-a**) [26]. The enantioselective C–H olefination of diphenylacetic acids was also realized using MPAA as ligand (**p2-b**) [24].

$$(4.2)$$

$$(4.3)$$
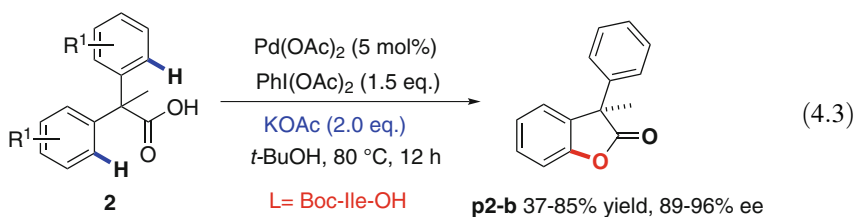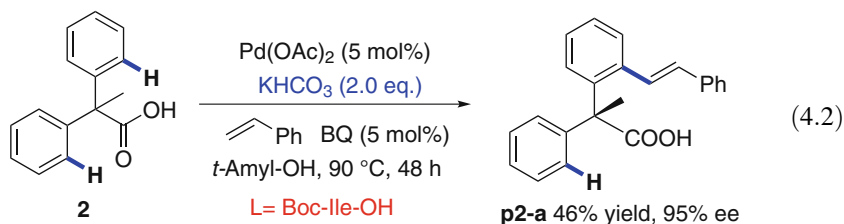
Enantiopure diarylmethylamines (**p3**) are important drug scaffolds, and considerable effort has been devoted to synthetic method development. Yu and coworkers reported the first example of enantioselective C–H iodination of prochiral diaryl-methylamine (**3**) using readily available chiral MPAA as ligand [27].

$$(4.4)$$
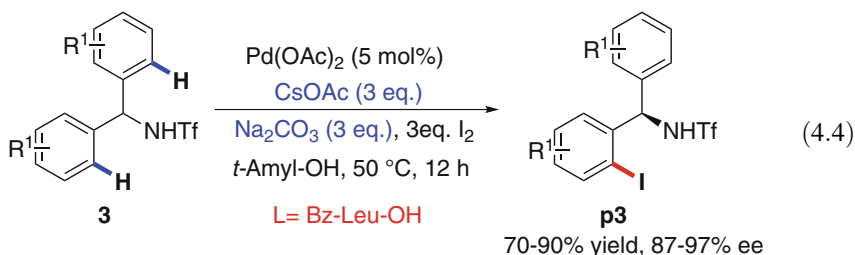
They extended the strategy of employing chiral MPAA ligands to enantiose-lective alkylation of C(*sp*^{3})–H bonds. Promising initial results were also obtained in asymmetric alkyl C–H activations of a pyridyl substrate containing gem-dimethyl groups (**4**) with up to 37% *e.e.* (Eq. 4.5) [35]. They further developed enantiose-lective C–H activation of cyclopropanes (**5**) employing MPAA as chiral ligands

[36]. This reaction was found to be compatible with a diverse range of organoboron reagents and proceeds under mild conditions (Eq. 4.6).

$$\text{(4.5)}$$

$$\text{(4.6)}$$
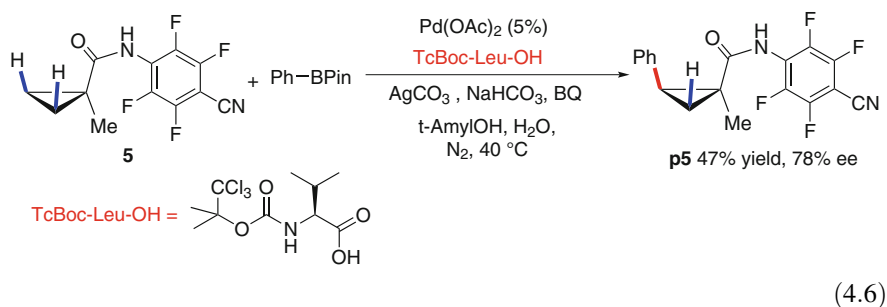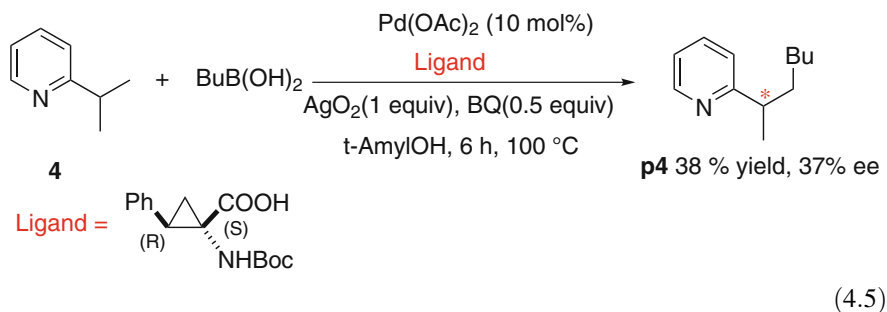
Planar chiral ferrocenes are very useful chiral ligands. Preparation of planar chiral ferrocenes is a longstanding interest but also challenge in organic synthesis. In 2013, the You group [25] and the Wu group [28] reported the asymmetric C–H arylation and olefination reactions of N,N-dimethylaminomethylferrocene (**6**), respectively. In both reactions, MPAA ligands were used as the chiral ligand, affording high enantioselectivity (90–99%). Beside the application in desymmetric C–H activation reactions introduced above, MPAA is also used in kinetic resolution as introduced in Chap. 1 [31, 32, 37, 38].

$$\text{(4.7)}$$

$$\text{(4.8)}$$
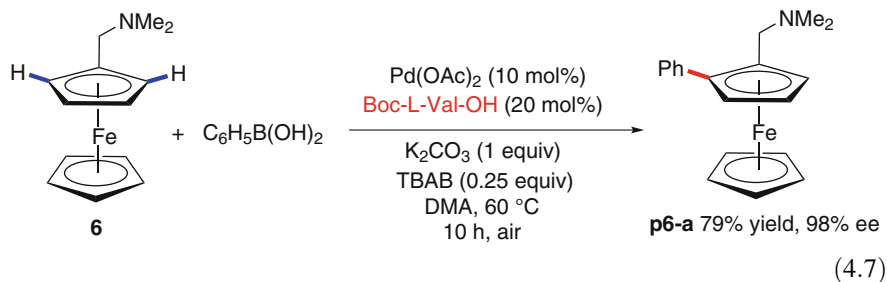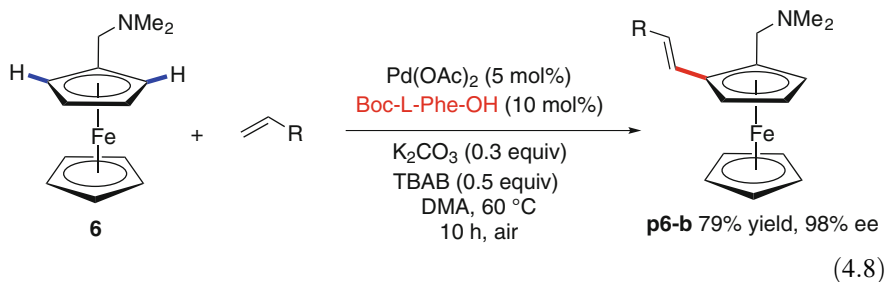
The reactions introduced above demonstrate the great potential of MPAA as effective chiral ligands for enantioseletice C–H activation reactions. In addition, MPAA are simple and readily available ligand which makes it more appealing. A mechanistic understanding of how chiral MPAA control the enantioselectivity will be helpful to the further development of enantioselective C–H bond activation. Obviously, the conventional concerted deprotonation and metalation (CMD) mechanism [39–44] for C–H bond activation involving palladium acetate (models **A** and **B** in Scheme 4.2) [40, 43–48] cannot account for the origin of enantioselectivity. Yu and coworkers obtained an X-ray crystal structure of the dimeric $Pd_2(1)_2(OAc)_2$ complex and proposed that MPAA binds with Pd in a bidentate manner [35], which is believed to be crucial for the enantioselectivity. Kinetic study by Blackmond and coworkers also supported the MPAA-bidentate model [49]. Yu proposed a gearing effect that relays the chirality from MPAA to substrate via Pd complex. However, the detail of how the *gears* connect to each other is absent. Musaev and coworkers reported a theoretical study on the enantioselectivity of reaction 1 using the bidentate MPAA model in the enantioselectivity-determining step [50]. Through a series of calculations, they found that model **C** (Scheme 4.2) is most favorable for the C–H bond activation. This model features an acetate anion as the deprotonation base in an outer-sphere manner. They also reported that this model reproduces the experimentally observed *R* selectivity [51]. This model nicely explains the observation that monodentate ligands **L4**, **L5**, and **L6** fail to give *e.e.* higher than 10%, because they cannot achieve bidentate coordination. But it is not clear how the model can explain the low enantioselectivity by **L3**. In addition, the origin of the enantioselectivity has not been unambiguously identified.
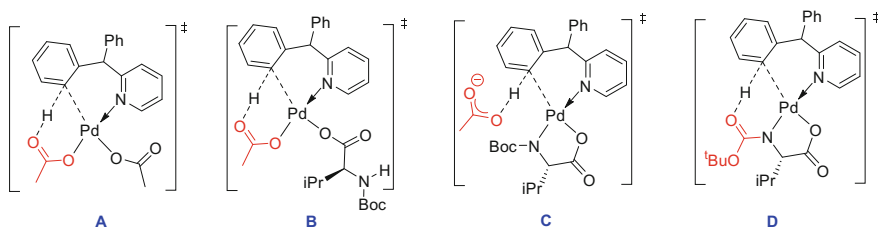
Scheme 4.2 Possible CMD (concerted metalation and deprotonation) mechanisms for the C–H activation of substrate **1**

In our recent study of Pd/MPAA-catalyzed *meta*-selective C–H activation of tethered arenes bearing a template, we identified the Pd^{II}-MPAA(solvent)$_2$ complex with MS [52]. Most interestingly, calculations indicated that the N-protecting group can serve as an internal base to deprotonate the C–H bond. This model reproduces the experimentally observed *meta*-selectivity well. A significant difference of the internal model (**D** shown in Scheme 4.2) from the model **C** is the absence of an external base. This makes model **D** very rigid, thus it may provide a better stereo-control.

Despite these studies, the involvement of the N-protecting group in C–H bond activation has not been directly proved. The detailed understanding of enantioselectivity (or the gearing effect) is still lacking. In the present study, we applied a combination of ion-mobility mass spectrometry (IM-MS) and theoretical study to reveal the critical role of N-protecting group in C–H activation. We captured the key intermediates from the mixture of catalyst, MPAA ligand and substrates, and confirmed the C–H activation can occur without an external base. We then developed a step-by-step relay of chirality model to understand the gearing effect with various MPAA ligands. The chirality relay model is also found to operate for reactions studied [53].

4.2 Experimental Methods and Computational Details

4.2.1 Experimental Methods

The MS experiments were conducted with a SYNAPT G2-s HDMS instrument with an electrospray ion source. More details about this hybrid mass spectrometer are presented elsewhere [54]. The instrument is mainly composed of an ion source, a quadrupole mass analyzer, a trap cell, a traveling wave ion-mobility analyzer, a transfer cell, an orthogonal acceleration time-of-flight (TOF) mass analyzer and a detector (Scheme 4.3a). Under HDMS mode, the mass-selected ions are accumulated in the trap section and periodically released into the ion-mobility (IM) section, in which the ions are separated according to their mobility. After extraction from the IM section, the ions pass through a transfer cell and enter a reflectron TOF region and arrive at the detector which continuously records mass spectra and the arrival time distribution. As described in Scheme 4.3b, the collision induced dissociation (CID) experiment can be performed in the trap cell (in front of the IM section) under TOF mode by increasing the applied voltage of the trap cell (E_{trap}). In this case the fragments will separated only based on *m/z* (Scheme 4.3b). Or as shown in Scheme 4.3c, CID can be performed in the transfer cell (behind the IM section) in which the generated daughter ions will have the same drift time as their parent ions under HDMS mode. Experimental drift time can be converted to the collision cross section (CCS) values by calibration approach, descriptions of this approach can be found in Chap. 1 [55–57]. CCS data were calibrated using polylysine.

(a) Schematic outline of the SYNAPT G2-s HDMS setup.

(b) ESI-MS/MS (CID conducted in trap section under TOF mode)

(c) IMS-CID (CID conducted in transfer section under HDMS mode)

Scheme 4.3 **a** Schematic outline of the SYNAPT G2-s HDMS setup. **b** ESI-MS/MS experiment. Mass-selected ions are fragmentated in the trap section. Since IMS section is off, fragments of ions with same *m/z* arrive at detector at the same time. **c** IMS-CID experiment. CID is conducted in transfer section after IMS separation. Ions with same *m/z* are separated based on size in IM section and their fragments generated in the transfer section maintain the mobility separation

For a given ion of interest, the elemental composition was confirmed by examination of the associated isotope patterns in the source spectra. Fragmentation analysis was performed with CID experiment to analyze the structure of ions. All the species detected in the present study were assigned by comparing the experimentally obtained isotopic pattern with the theoretically calculated one. The structures were determined based on the CID experiment and theoretical calculation.

4.2.2   Computational Details

Theoretical CCSs were estimated using the open source software program MOBCAL [58]. In brief, this program calculates rotationally averaged cross sections of input coordinate files based on three different models/algorithms, including the projection approximation (PA) [59], exact hard sphere scattering (EHSS) [60], and the trajectory method (TM) [61]. The trajectory method (TM) is considered to be the most reliable method to calculate the CCS since this approach takes into account the long-range interactions and close collisions between the ion and buffer gas atom, as well as the effects of multiple collisions. In this work, the CCS values obtained from MOBCAL using trajectory method and DFT optimized structure as input were compared to the experiment-derived ones.

All the DFT calculations were carried out with the Gaussian 09 package [62]. Unless mentioned otherwise, geometry optimizations were performed with the B3LYP hybrid functional [63–66]. The LANL2DZ + f (1.472) [67, 68] basis set with ECP was used for Pd atom and the 6-31G (d) [69, 70] basis set was used for other atoms. Frequency analysis was conducted at the same level of theory to verify the stationary points to be real minima or saddle points and to obtain the thermo-dynamic energy corrections. Single point energies were calculated at the M06/SDD-6-311++G(d, p) [71–74] level. Solvent effects (Solvent = THF for substrate **1**, solvent = (2-propanol, read), eps = 12.47 for substrate **2** and solvent = 1-pentanol for substrate **3**) were evaluated by using the SMD solvation model [75]. The relative energies with ZPE corrections and free energies (at 298.15 K) are in kcal/mol. 3D structures are displayed with CYLView [76].

4.3 Results and Discussion

4.3.1 Identifying Pd(MPAA)(Substrate 1) Complexes by ESI-MS/MS

Owning to the capability to introduce species in solution sample to the gas phase, electrospray ionization (ESI) enables mass spectrometry (MS) to become a powerful tool in mechanistic studies. We started the study by identifying the critical intermediates of the reaction of 2-benzhydrylpyridine (**1**) using electrospray ionization mass spectrometry (ESI-MS). The presence of a strongly coordinating group, pyridine, makes it possible to isolate and manipulate the Pd(MPAA)(substrate) complex in the mass spectrometer. An 1:1:1 mixture of Pd(OAc)$_2$, N-acetyl-Alanine [77] and **1** in methanol was analyzed by ESI-MS. The expected [Pd(N-Ac-Alanine)(**1**), -H]$^+$ complex was detected at *m/z* 481 and confirmed by the isotope pattern (Fig. 4.1).
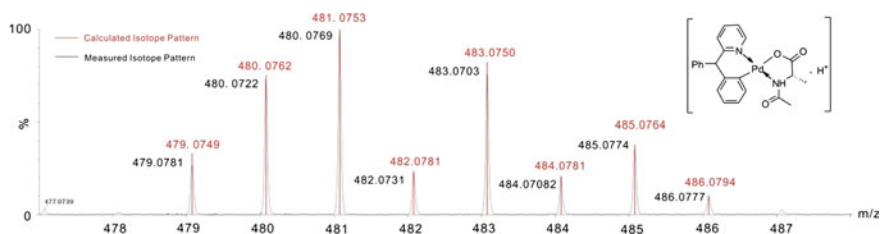

Fig. 4.1 Isotope pattern of protonated complex [Pd(N-Ac-Alanine)(**1**), -H]$^+$ derived from a 1:1:1 mixture of Pd(OAc)$_2$, N-acetyl-alanine and **1** dissolved in CH$_3$OH. Calculated isotope pattern is shown in *red* and measured isotope pattern is in *black*
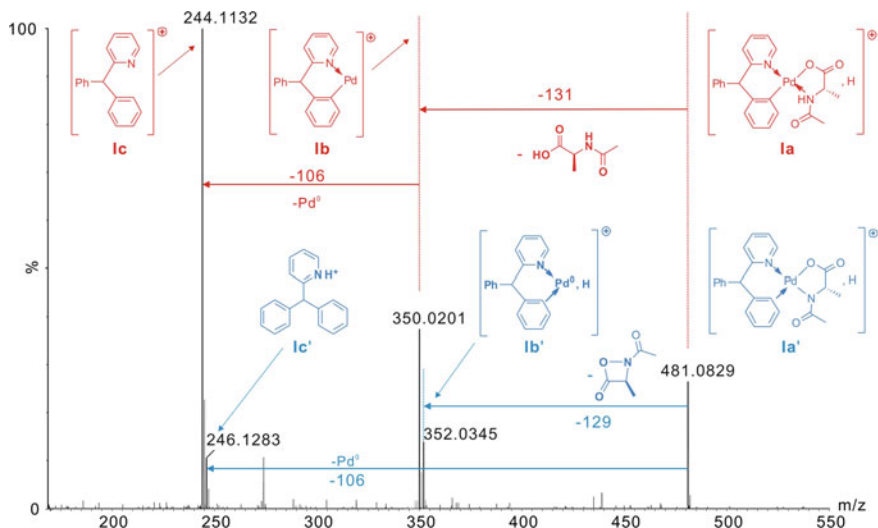
Fig. 4.2 Fragmentation analysis of protonated complex [Pd(N-Ac-Alanine)(**1**), -H]$^+$ derived from a 1:1:1 mixture of Pd(OAc)$_2$, N-acetyl-alanine and **1** dissolved in CH$_3$OH. Fragmentation analysis was conducted at E$_{trap}$ = 10 eV. Reproduced from ref. [96] by permission of John Wiley & Sons Ltd.

To obtain more information about its structure, the ion of *m/z* 481 was subjected to further MS/MS analysis. Upon collision with Ar, the parent ion *m/z* 481 dissociated in two channels colored with red and blue, respectively (Fig. 4.2). Dissociation channel I (red) showed the loss of the N-Ac-Alanine ligand (−131 Da) and resulted in the formation of the cyclopalladated complex ion (**Ib**) of *m/z* 350. Further dissociation of a neutral Pd (−106 Da) from **Ib** released a cationic complex **Ic** of *m/z* 244. This major dissociation channel indicates that the activation of C–H bond in **1** and the formation of Pd–C metalation complex take place in solvent or during collision induced dissociation (CID) process (as discussed in the next paragraph). As a minor pathway, dissociation channel II (blue) was observed with the formation of an ion **Ib′** of *m/z* 352. This fragment ion was assigned as the protonated complex of unactivated **1** and Pd, with the loss of dehydrogenated N-Ac-Alanine (−129 Da). The ion *m/z* 246 (**Ic′**) matches the protonated substrate **1**, which dissociates from **Ib′** with the loss of Pd (−106 Da).

The observation of two dissociation channels implies two possibilities: (1) The parent peak at *m/z* 481 contains one species **Ia′**, in which substrate **1** has not been activated before evaporating into the gas phase from solution. CID leads to both activation of C–H in **1** (major) and dissociation of unactivated **1** (minor); (2) If the substrate **1** has been activated in solution, the parent peak at *m/z* 481 may contain two different species **Ia** and **Ia′**. CID of the mixture of **Ia** and **Ia′** then results in two dissociation channels. Clarifying these two scenarios by characterizing the components of the parent complexes would provide important information to understand the reaction mechanism. If **Ia′**, in which the C–H bond remains intact, is isolated in the gas phase and activated upon low energy CID, then the MS provides

direct evidence that the C–H bond can be abstracted by MPAA in the absence of an external base. Characterization of the components of the parent ion will be discussed in the next section.

4.3.2 The IM-MS Experiment of Pd(MPAA)(Substrate 1) Complexes

The observation of the two possible channels of dissociations of intermediates **I** indicates the possibility of coexistence of **Ia/Ia′**. However, **Ia/Ia′** cannot be separated by a conventional mass spectrometer since they have same *m/z*. Thus, an additional tool is needed to address this issue. Ion-mobility mass spectrometry (IM-MS) [54, 78, 79], which can distinguish ions with the same *m/z* based on the molecular shapes, has been proven to be powerful for illustrating structural information of biomolecules [80–84]. Schröder and Roithová's pioneering work demonstrated the capability of IM-MS in studying reaction mechanisms [85–90]. Therefore, we were encouraged to employ IM-MS to probe the components and structure of the parent ions.

   Ia/Ia′ was first subjected to an ion-mobility investigation. Unfortunately, mass-selected ion of *m/z* 481 (**Ia/Ia′**) could not be separated in the ion-mobility section. A single IMS peak corresponding to a collision cross section (CCS) of 125 Å^2 was detected (Fig. 4.3). Theoretical CCSs [91] for **Ia** and **Ia′** were

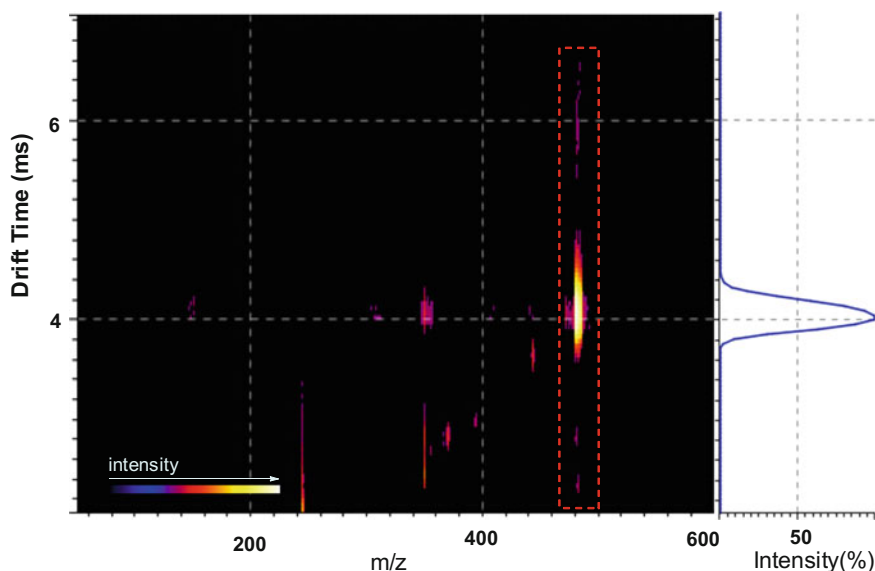
Fig. 4.3 Ion-mobility trace of the protonated ions [Pd(N-Ac-Alanine)(**1**), -H]$^+$ (*m/z* 481). (mobility gas: N$_2$, gas pressure: 5.23 mbar; collision gas: Ar, gas pressure: 1.87×10^{-2} mbar, U$_{trap}$: 0 V, U$_{ransfer}$: 0 V)

calculated to be 129 and 130 Å^2 [92], respectively, which were unable to be differentiated by the instrument.

4.3.3   Identifying Pd(MPAA)(Substrate 2) Complexes by ESI-MS/MS

Because the [Pd(N-Ac-Alanine)(**1**), -H]$^+$ cannot be separated in ion-mobility section, we then turned to examine the intermediates derived from substrate **2**, diphenylacetic acid. An 1:1:1:1 mixture of Pd(OAc)$_2$, N-acetyl-alanine, **2** and potassium acetate [93] dissolved in methanol was analyzed by ESI-MS. A cationic complex [Pd(N-Ac-Alanine)(**2**), K, -2H]$^+$ was detected at m/z 500, as indicated by the isotope pattern and fragment analysis (Fig. 4.4).

The ion of m/z 500 was selected for further MS/MS experiment. Two dissociation channels were also observed for [Pd(N-Ac-Alanine)(**2**), K, -H]$^+$ as shown in Fig. 4.5. In the major dissociation channel (red channel), the parent ion [Pd (N-Ac-Alanine)(**2**), K, -H]$^+$ either lost the neutral ligand, N-Ac-Alanine, to generate a cyclopalladated complex ion **IIb** (m/z 369) or lost the neutral complex Pd(**2**) to release a cationic complex **IId** of m/z 170. The further elimination of Pd from ion **IIb** resulted in a cationic complex **IIc** of m/z 263. The observation of this dissociation channel suggests the C–H activation of **2** and the formation of Pd–C metalation complex. In the minor dissociation channel (blue channel), the dissociation of a neutral substrate (m/z 226) was detected which indicates the existence of unactivated substrate **2** in the parent ion.

As discussed in the previous section for substrate **1** (vide supra), the observation of two dissociation channels implies two possibilities that either the parent ion of m/z 500 contains one species **IIa′** or two different species **IIa** and **IIa′**. More importantly, if **IIa** which contains unactivated substrate is isolated in the gas phase
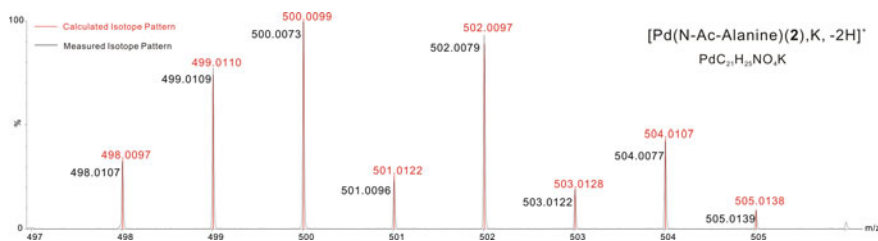

Fig. 4.4 Characterization of protonated complex [Pd(N-Ac-Alanine)(**2**), K, -2H]$^+$ with mass spectrometry. Calculated isotope pattern is shown in *red* and measured isotope pattern is in *black*
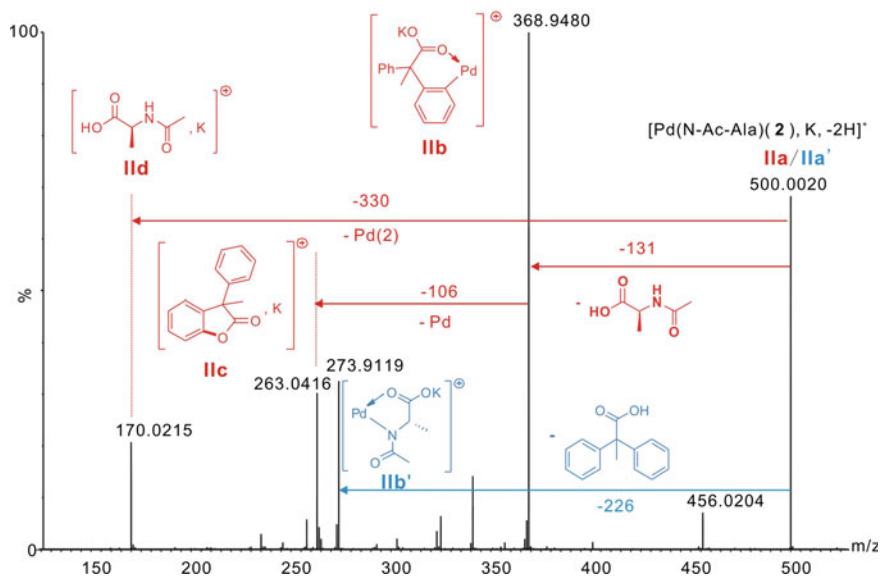
Fig. 4.5 Fragmentation analysis of protonated complex [Pd(N-Ac-Alanine)(**2**), K, -2H]$^+$ (*m/z* 500) (collision gas: Ar, gas pressure: 1.87×10^{-2} mbar, U$_{trap}$: 10 eV, U$_{ransfer}$: 0 eV). Reproduced from Ref. [96] by permission of John Wiley & Sons Ltd.

and activated upon low energy CID, then the MS experiment provides direct evidence that the C–H bond can be activated by MPAA in the absence of an external base. To characterize the components of the parent ion, IM-MS experiment was conducted which is discussed in the next section.

4.3.4   Separating Pd(MPAA)(Substrate 2) Complexes by IM-MS

The mass-selected ion of *m/z* 500 was analyzed by IM-MS method and separated into two peaks (Fig. 4.6), indicating that there are two distinguishable isomers or conformations for the cationic complex [Pd(N-Ac-Alanine)(**2**), K, -2H]$^+$. In this experiment, a smaller component has a shorter drift time compared to a larger one. The drift time for each component was converted into a CCS value. The experimentally derived CCS values for the fast and slow components are 123 and 141 Å^2, respectively.
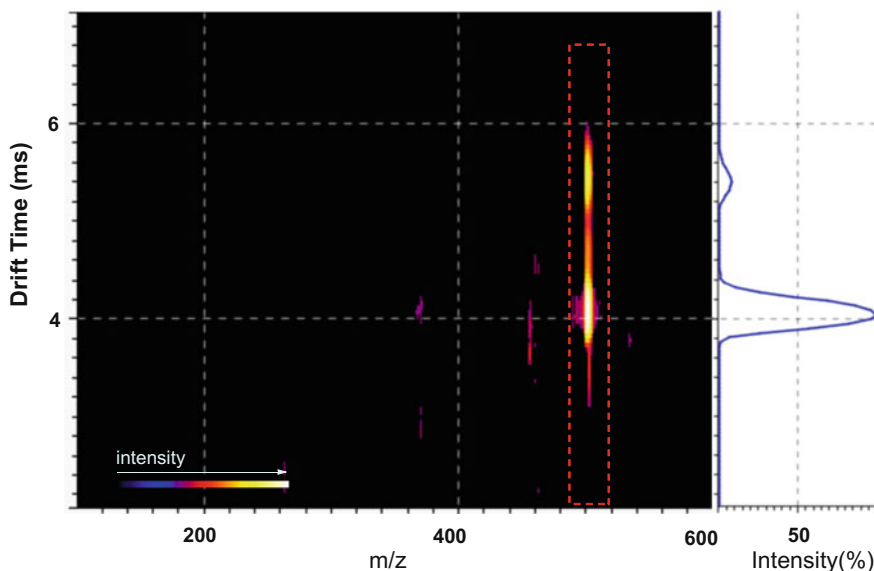
Fig. 4.6 Ion-mobility trace of the protonated ions [Pd(N-Ac-Alanine)(**2**), K, -2H]$^+$ (*m/z* 500). (mobility gas: N$_2$, gas pressure: 5.23 mbar; collision gas: Ar, gas pressure: 1.87×10^{-2} mbar, U$_{trap}$: 0 V, U$_{ransfer}$: 0 V)

4.3.5   Structural Assignment of Pd(MPAA)(Substrate 2) Complexes

Density functional theory (DFT) calculations were conducted to optimize the possible structures of the complex [Pd(N-Ac-Alanine)(**2**), K, -2H]$^+$ and calculate the corresponding energies. Theoretical CCS values were then calculated for these optimized structures using MOBCAL. The structures of the two peaks were assignment by comparing the theoretical and experimental CCS values. As listed in Fig. 4.7, fifteen possible structures of complex [Pd(N-Ac-Alanine)(**2**), K, -2H]$^+$ were computed considering different locations of K and H, different conformations as well as different states of substrate (activated or unactivated). The substrate is activated in structures **IIa-X** (X = 1 ∼ 6) while it remains unactivated in structures **IIa′-X** (X = 1 ∼ 9). These structures were divided into two groups according to their theoretical CCS values. For structures in group **I**, both the carboxyl group and the phenyl group of the substrate bind with Pd, leading to relatively compact structures, and their calculated CCS values are between 123 and 131 Å^2, which are close to the experimental CCS value (123 Å^2) of the fast peak. Therefore, the group **I** is composed of both activated (**IIa**) and unactivated (**IIa′**) isomers. The calculated CCS values of group **II** are between 139 and 141 Å^2 which agrees well to the experimental CCS value (141 Å^2) of the slow peaks. Group **II** only contains structures with unactivated substrates (**IIa′**) because the larger CCS corresponding
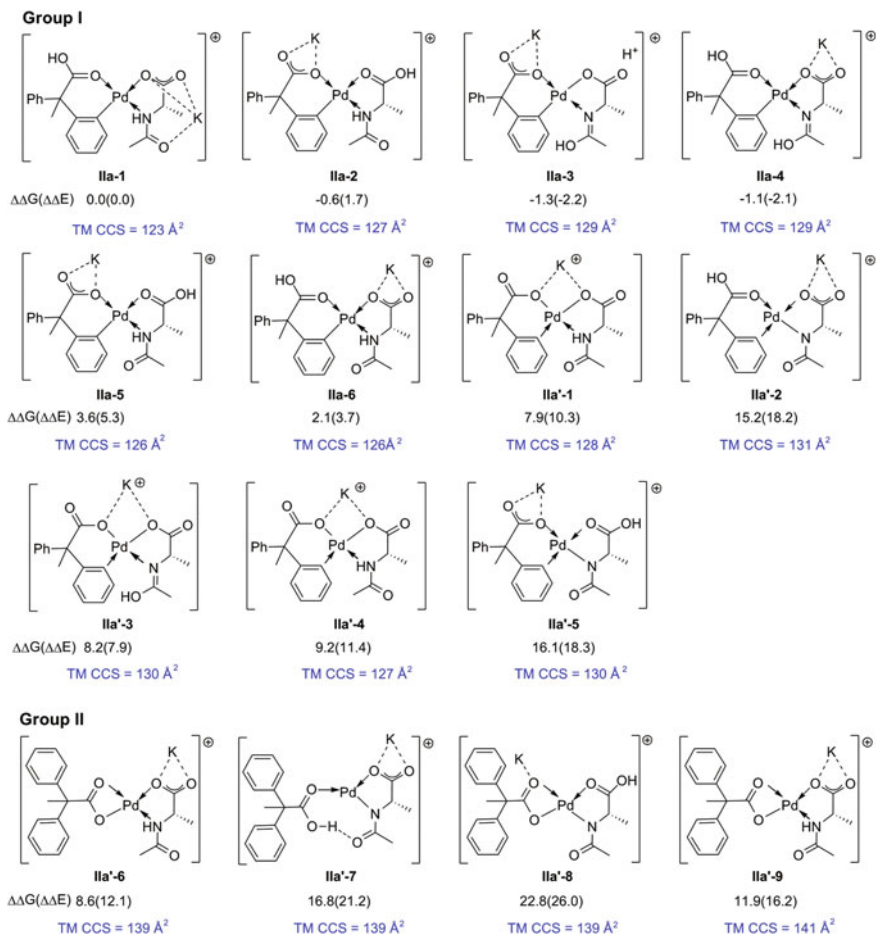
Fig. 4.7 Calculated structures of [Pd(N-Ac-Alanine)(**2**), K, -2H]$^+$ complex (energies are presented in kcal/mol) and theoretical CCS (collision cross section) values of [Pd (N-Ac-Alanine)(**2**), K, -2H]$^+$ complex calculated by MOBCAL with trajectory method (TM)

to extended geometries could only be achieved when the carboxylate group of substrate **2** binds with Pd via bidentate way which orientates two unactivated phenyl groups away from the Pd center.

The observation that complexes [Pd(N-Ac-Alanine)(**1**), -H]$^+$ cannot be differentiated by IMS while two peaks was detected for complex [Pd(N-Ac-Alanine)(**2**), K, -2H]$^+$ demonstrate that the structure of substrate is crucial for the separation between two isomers (**Ia/Ia′** and **IIa/IIa′**). The carboxylate group of substrate **2** can bind with substrate via bidentate way which orientates two phenyl groups away from the Pd center and forms an extended structure. However, the substrate **1** with a

monodentate pyridine group cannot achieve extended geometry in complex **Ia′**. Thus, this experiment further confirmed that the structural difference between **IIa** and **IIa′** is attributed to the substrate part, instead of the MPAA ligand part, supporting the structural assignment for **IIa** and **IIa′**.

4.3.6   Activation of C–H in Pd(MPAA)(Substrate 2) Complexes Proven by IMS-CID Experiment

The detection of two peaks for **IIa** and **IIa′** by IM-MS also assists to clarify the previously proposed two scenarios and supports the second proposal that substrate **2** has been activated in solution and the parent ion peak at *m/z* 500 contains two different species **IIa** and **IIa′**. Most importantly, the separation of **IIa′** with unactivated substrate provides a chance to study the C–H bond activation in the gas phase.

Following the separation of two ions in the ion-mobility section, CID analysis for these two components was conducted in transfer cell (after the IM section) (Fig. 4.8). Upon collision with Ar, the fast component (Fig. 4.8b) may lose N-Ac-Alanine ligand to generate [Pd(**2**), K, -2H]$^+$ complex (*m/z* 369, **IIb**) or neutral [Pd(**2**), -2H] to yield the potassium adduct of N-Ac-Alanine (*m/z* 170, **IId**). Both of these two ions indicate the C–H bond in **2** has been activated. Different from the previous two cases shown in Figs. 4.2 and 4.5, negligible loss of the unactivated starting substrate was observed, implying that the fast component mainly contains activated species.

For the CID of the slow peak (Fig. 4.8c), the primary fragment [Pd (N-Ac-Alanine), K, -2H]$^+$ (*m/z* 274) with a neutral loss of substrate **2**, confirms that the C–H bond of **2** remains intact. According to the analysis in Sect. 4.3.5, the slow peak only contains complexes with unactivated substrates. However, ions of *m/z* 369 and *m/z* 170 were also detected in the CID spectrum of the slow component. This observation indicates that the unactivated substrate **2** in the slow component can be activated after being isolated by ion-mobility section. This facile process to activate **2** in the slow component **IIa'** indicates that the MPAA ligand can abstract a proton from the substrate in the absence of an external base, supporting the model **D** in Scheme 4.2.

In conclusion, we observed the critical Pd^{II}(MPAA)(substrate) complex using MS. Two isomers (with activated or unactivated substrates) of Pd^{II}(MPAA)(substrate **2**) complex were separated by IM-MS. After separation, the substrate was shown to be activated by MPAA ligand for the slow component. This finding supports the internal base model and suggests that the C–H bond of the substrate can be activated without an external base. Having identified the species relevant to C–H activation through MS studies, we turned to computational methods to obtain their structures at the atomic level and elucidate the origin of enantioselectivity.

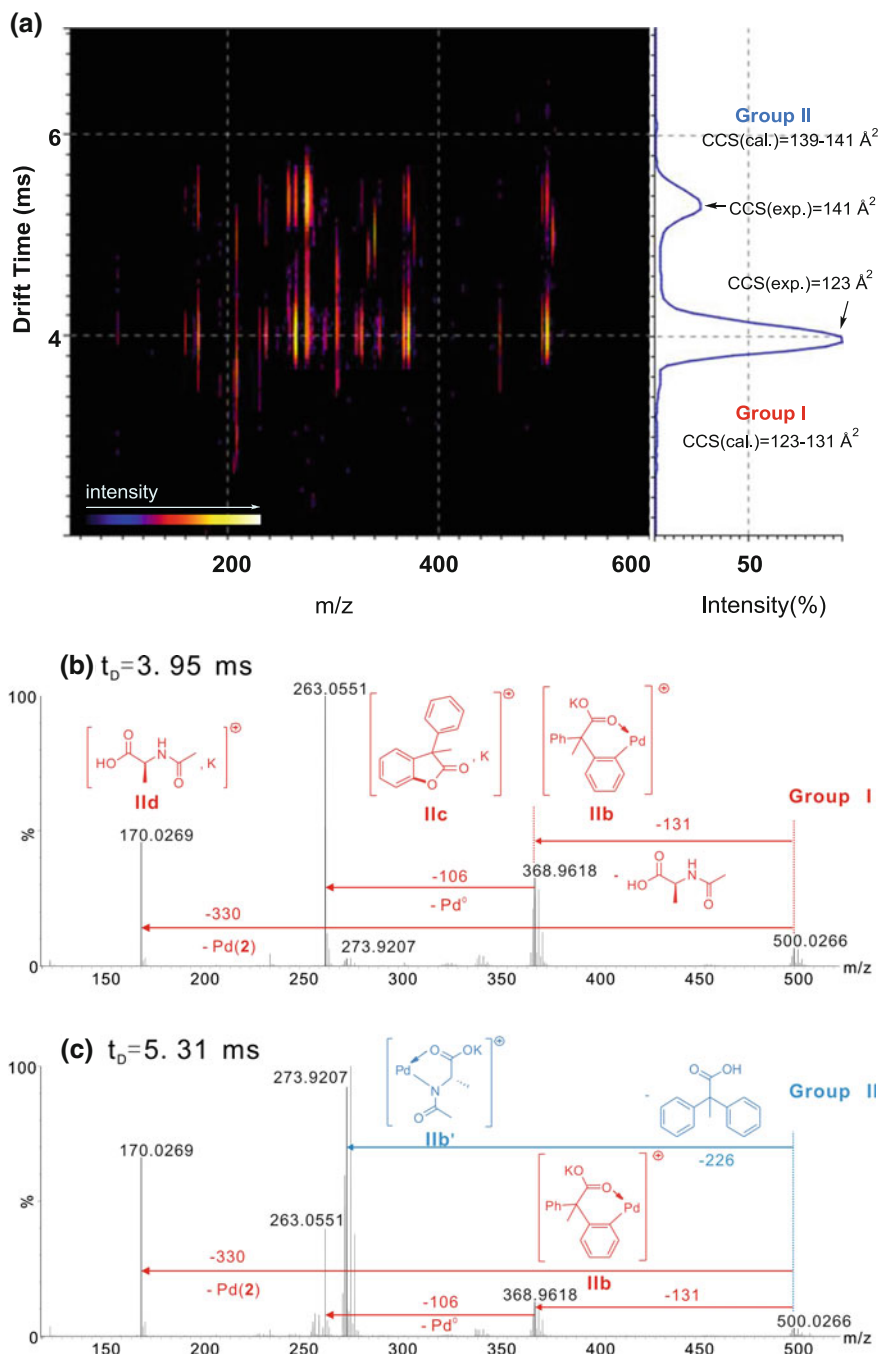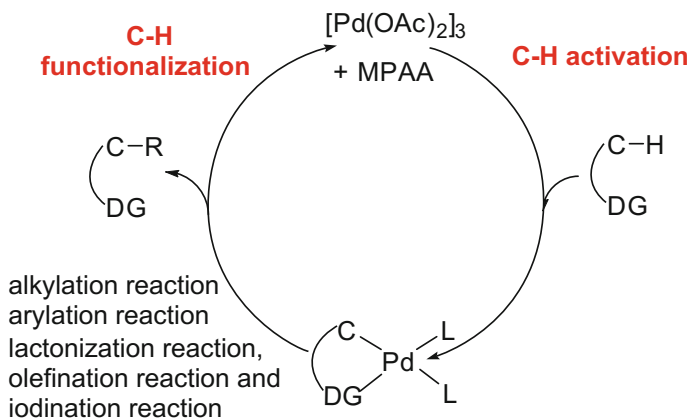**Fig. 4.8 a** Ion-mobility trace of the protonated ions [Pd(N-Ac-Alanine)(**2**), K, -2H]$^+$ (m/z 500) and the CID mass spectra of the fast (**b**) and the slow (**c**) components at E_{trans} = 25 V. Reproduced from Ref. [96] by permission of John Wiley & Sons Ltd.

Scheme 4.4 General catalytic cycle for Pd(OAc)$_2$/MPAA catalyzed C–H activation and functionalization

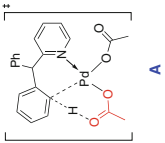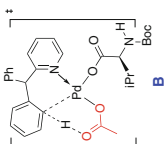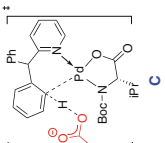## 4.3.7 Computational Study on Reaction Mechanism
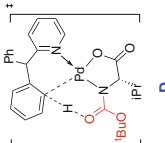
For the different reactions under investigation, a general catalytic cycle is depicted in Scheme 4.4. These reactions share a similar C–H activation step, but differ in the functionalization step, so C–H bond activation is expected to be the enantioselectivity-determining step.

Table 4.1 summarizes the computational results of the four representative pathways (Scheme 4.2). Several calculation methods were tested. Computational results with wB97XD[a] and B3LYP-D3[a] methods which involve corrections for dispersion interaction show similar trends with the result of M06[a]. M06[b] using M06 optimized geometry also gives a consistent result with M06[a]. The following discussion is based on the results of M06[a].

Pathway **A** represents the system without a chiral MPAA ligand. It was calculated to have a moderate activation free energy of 22.6 kcal/mol, which indicates that the reaction can take place in the absence of MPAA ligand. In pathway **B**, a monodentate MPAA ligand bound to the Pd is too flexible and too far away for chiral induction. Thus, it is not surprising that no difference in activation free energy is calculated for the formation of the *R* and *S* enantiomers. Pathway **C** is the outer-sphere model proposed by Musaev and coworkers [50]. In this model, the C–H bond is deprotonated by an external base which is flexible, leading to an activation free energy difference of 1.1 kcal/mol between the pathways leading to the *R* and *S* enantiomers. This model has a higher activation free energy than model **B** and **D**. Furthermore, the IM-MS experiment demonstrates that the C–H bond can be activated in the Pd(MPAA)(substrate) complex without an external base.

In model **D**, the N-protecting group acts as the internal base. It is expected to effectively relay the chirality of the α-chiral carbon center to the spatial orientation of the carboxylate group, which is directly involved in the deprotonation step that

Table 4.1 Activation free energies (in kcal/mol) of pathways (**A**, **B**, **C** and **D**) leading to *R/S* enantiomers

		A	B	C	D
M06[a]	R	22.6	19.2	22.0	19.3
	S	22.6	19.2	23.1	23.3
wB97XD[a]	R	27.3	23.4	26.6	22.1
	S	27.3	23.4	28.0	26.3
B3LYP-D3[a]	R	26.2	22.4	26.0	22.2
	S	26.2	22.5	28.1	26.1
M06[b]	R	21.4	20.6	21.2	17.7
	S	21.4	20.0	23.0	21.1

Geometry optimizations were performed with the [a]B3LYP or [b]M06 using LANL2DZ-6-31G(d) basis set. Single point energies were calculated employing M06, wB97XD and B3LYP-D3 methods with SDD-6-311++G(d, p) basis set

determines the enantioselectivity. Indeed, pathway **D** favors the *R* product over the *S* product by 4.0 kcal/mol which corresponds to a high *e.e.* (99.8%). Nevertheless, the calculated activation free energy for the formation of the preferred *R* enantiomer in pathway **D** is about the same as the one calculated for pathway **B**. It is thus possible that pathway **B** may compete with pathway **D**, resulting in a reduction in enantioselectivity. As will be discussed later, this may indeed be the case for **L3**.

4.3.8 Computational Study on the Origin of Enantioselectivity

We further studied the origin of enantioselectivity for pathway **D**. Figures 4.9 and 4.10 show the four transition states for the C–H activation of substrate **1**, which determine the enantioselectivity. In these transition states, Pd coordinates with two rigid moieties, the MPAA ligand and the substrate in a square planar coordination. The MPAA ligand binds with Pd in a bidentate way, forming a pseudo-planar five-membered ring. The side-chain (*iPr*) of amino acid points upward. This orientation is used throughout the text. The N-protecting group is bent downward below the Pd coordination plane [94] as indicated by a C1–N2–Pd–O3 (α1) dihedral angle of about 140°. Although this leads to a partial loss of conjugation,
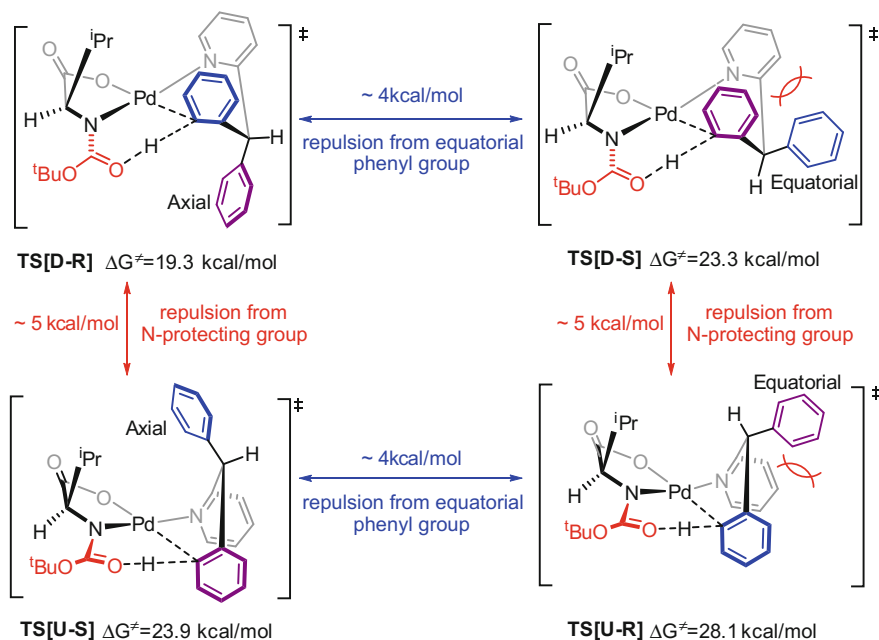

Fig. 4.9 Four transition states for the C–H activation of substrate **1**. The prochiral carbon may point downward (**D**) or upward (**U**)

α1(C1,N2,Pd,O3) = 140.4°

TS[D-R]

α1(C1,N2,Pd,O3) = 139.8°

TS[D-S]

α1(C1,N2,Pd,O3) = -172.4°

TS[U-S]

α1(C1,N2,Pd,O3) = -172.9°

TS[U-R]
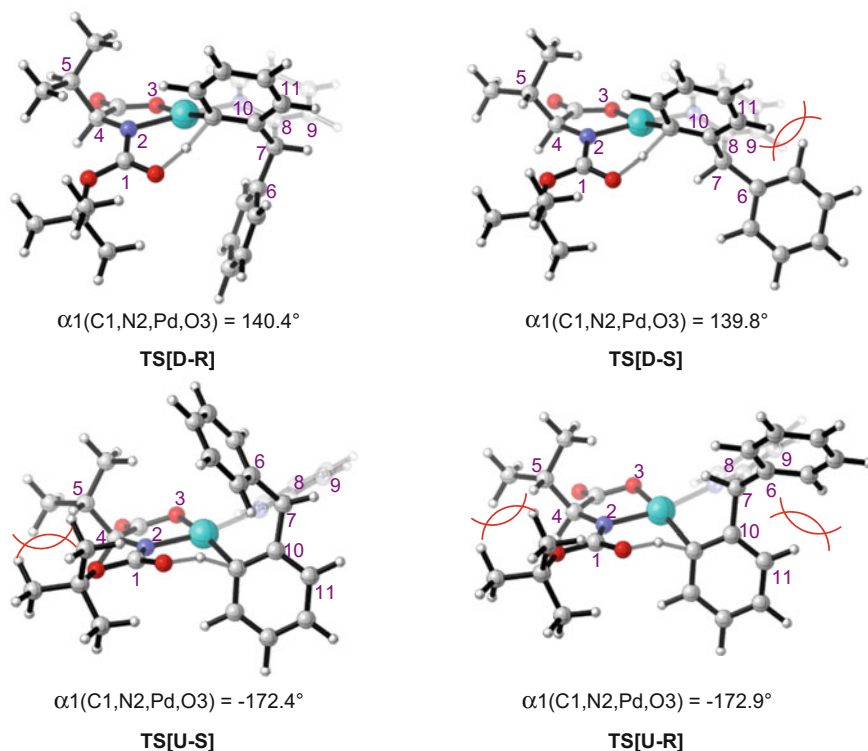
Fig. 4.10 Optimized geometries of four transition states for the C–H activation of substrate **1**

the severe steric repulsion from the *iPr* group is avoided. For the substrate, both the pyridyl group and the phenyl group that undergoes C–H activation coordinate with Pd. The substrate coordinates with Pd in a six-membered ring that adopts a twist-boat conformation. Pd and C7 locate at two heads of the "boat", puckering the activated phenyl group and pyridyl group into a "face-to-face" conformation.

In **TS[D-R]** and **TS[D-S]** the prochiral carbon (C7) points downward, orienting the coplanar *ortho* C–H bond (to be activated) below the Pd coordination plane. The downward orientation of the C–H bond matches with the preferred conformation of the bent internal base (Boc). While in **TS[U-S]** and **TS[U-R]**, the prochiral carbon (C7) is upward, making the *ortho* C–H bond (to be activated) upward. This makes the hydrogen abstraction by the internal base Boc unfavorable. Thus, **TS[D-R]** and **TS[D-S]** are about 5 kcal/mol more stable than **TS[U-S]** and **TS[U-R]**, respectively. It is also clear that the spectator phenyl group at C7 prefers axial over equatorial by about 4 kcal/mol (Fig. 4.9).

Table 4.2 summarizes the calculated relative energies of the four transition states as well as the relative distortion energies of the catalyst part (Pd and MAPP) and substrate part (substrate) of the four transition states. **TS[D-R]** is approximately 4.8 kcal/mol more stable than **TS[U-S]**. The two transition states have nearly the

Table 4.2 Distortion analysis [95] of four TSs for C–H activation of substrate **1** and related key dihedral angles[a] (energies are reported in kcal/mol)

	$\Delta\Delta E^{\neq}$	Relative Distortion Energy		Key dihedral angles			
		Catalyst part	Substrate part	α1 (C1–N2–Pd–O3)	α2 (C1–N2–C4–C5)	α3 (H6–C7–C8–C9)	α4 (C6–C7–C10–C11)
TS[D-R]	**0.0**	**0.0**	**0.0**	140.4	101.6	−103.6	129.6
TS[D-S]	4.0	0.3	3.1	139.8	101.5	−5.2	35.3
TS[U-S]	4.8	3.9	0.6	−172.4	60.5	106.2	−134.4
TS[U-R]	9.2	4.0	3.6	−172.9	60.7	4.9	−37.6

[a]This table summarizes relative electronic energy, and relative distortion energy for the catalyst part and substrate part in these transition states. $\Delta\Delta E_{dis}$(cat.) and $\Delta\Delta E_{dis}$(sub.) are energy difference between corresponding fragments using **TS[D-R]** as reference

same geometry for the substrate part as indicated by the small energy difference of 0.6 kcal/mol. As mentioned above, the activated C–H bond in **TS[D-R]** points downward, matching the downward position of the Boc group However, the C–H bond in **TS[U-S]** points upward. In order to accept the proton, the Boc group is forced to go upward. Thus, the α1 dihedral angle becomes about −172°. This is the main reason why the catalyst part of **TS[U-S]** is less stable than that of **TS[D-R]**.

TS[D-R] is also approximately 4.0 kcal/mol more stable than **TS[D-S]**. Since the two structures have very similar geometry for the catalyst part, the major difference is from the destabilization in the substrate part of **TS[D-S]** (3.1 kcal/mol). The spectator phenyl group in **TS[D-R]** is at the axial position. It avoids steric interaction with the pyridyl and the reactive phenyl groups. On the other hand, the spectator phenyl group in **TS[D-S]** is equatorial and is subject to strong steric repulsions with the two rings. The C6–C7–C8–C9 (α3) and C6–C7–C10–C11 (α4) dihedral angles are −5.2 and 35.3°, respectively. The 9.2 kcal/mol destabilization of **TS[U-R]** with respect to **TS[D-R]** can be mainly attributed to the destabilizations in the catalyst part and the substrate part, as discussed above.

4.3.9   Chirality Relay Model and Its Application

Previously, it was proposed that the repulsion between the substrate and the MPAA leads to the observed enantioselectivity [17, 35]. We do not find a direct interaction between the *iPr* (or Boc) group and the substrate since the closest distance between these moieties is about 3 Å. Therefore, we propose a relay mechanism to explain the enantioselectivity (Fig. 4.11). Here, steric repulsion of the amino acid side-chain (*iPr*) pushes the N-protecting group below the Pd coordination plane. Since the N-protecting group is the internal base for proton abstraction, it requires the substrate to coordinate in such a way to have the activating C–H bond directing downward to the carbonyl oxygen of the N-protecting group. The sp^2 C–H bond constrains the prochiral carbon at the coplanar *ortho* position also to orient downward. Finally, due to the rigid coordination of the substrate, the steric effects of the R^S (small group) and

R^L (large group) discriminate the formation of the R and S enantiomers. The R^L should take the sterically less crowded position (axial) which avoids forming eclipsed conformation with the reacting upward phenyl group.

The above relay model can be easily applied to the reactions of substrates **2** and **3** since these two substrates are diphenyl derivatives and share similar structural features with substrate **1**. As shown in Fig. 4.11, the spectator phenyl group (R^L) adopts the axial position to avoid steric interactions with the neighboring groups, leading to the formation of R enantiomers, in agreement with experimental observations.

The above model can be equally well applied to understand the enantioselective reactions involving substrates **4–6**. The computational results are presented in Fig. 4.12. In the case of substrate **4** containing gem-dimethyl groups, we calculated a difference of activation free energies of 0.9 kcal/mol between R and S enantiomers. Four transition states are possible, but only the two transition states with the spectator methyl group in the axial position are presented. The other two transition states with the spectator methyl group in the equatorial position are less stable due to steric repulsion with the pyridyl ring. Substrate **4** also coordinates to Pd in a twisted conformation. Since there is a near staggering about the C4–C5 bond, the activated C–H bond points downward in **4-TS-R** but upward in **4-TS-S**, as can be clearly seen in Newman projects. However, because the cyclopropane amino acid ligand has two Cα substituents, the bending of the N-protecting group is less significant than in **1**, as indicated by the larger dihedral angle α1 of 167° in **4-TS-R**, as compared to α1 of 140° in **TS[D-R]**. Thus, the calculated free energy difference between **4-TS-R** and **4-TS-S** is reduced to 0.9 kcal/mol.

For the reaction of substrate **5**, we only located two transition states. Because of the rigidity in substrate coordination, only the hydrogen atoms 4 and 5 on the inward face of the cyclopropane plane (*anti* to the methyl group) can be deprotonated by the carbonyl group. The other two hydrogen atoms are placed on the outward face of the cyclopropane plane (*syn* to the methyl group) and are too far away from the carbonyl group of the N-protecting group. Different from the methyl
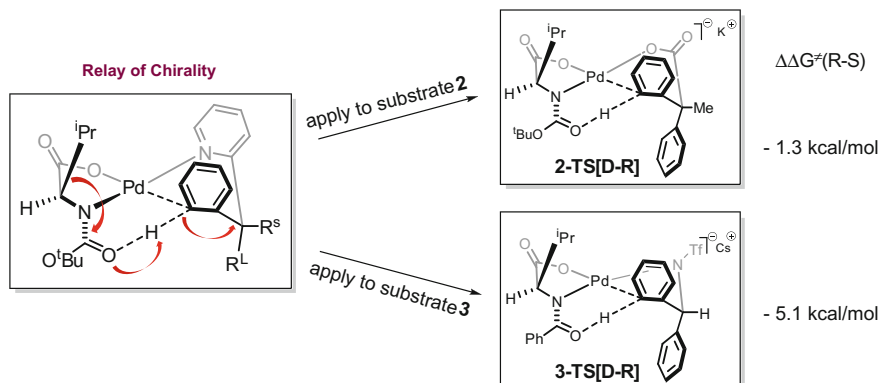
Fig. 4.11 The chirality relay model and its application to the C–H activation of substrates **2** and **3**
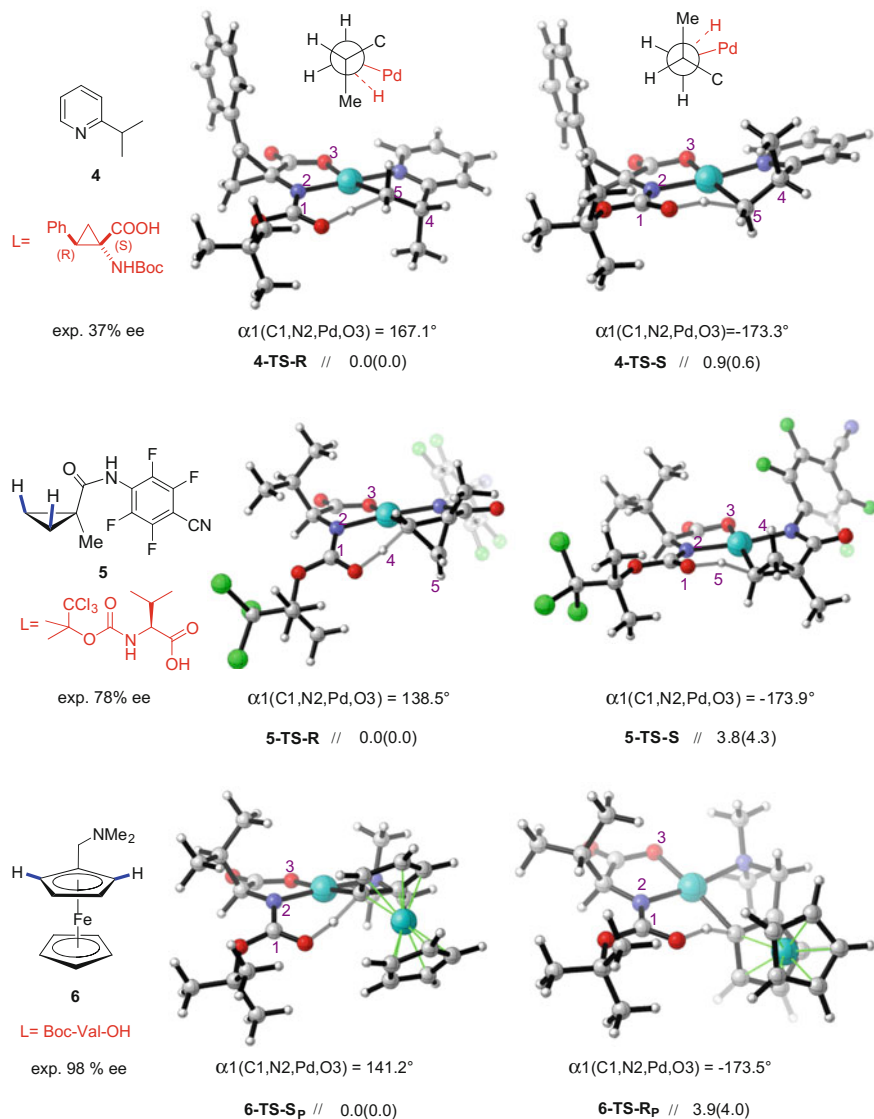
Fig. 4.12 Optimized geometries of transition states for C–H activation of substrates **4, 5** and **6**. Relative activation free energies (relative activation electronic energies in parentheses) are reported in kcal/mol. Reproduced from Ref. [96] by permission of John Wiley & Sons Ltd.

group in **4**, the sp^3 C–H in **5** is constrained by the rigid cyclopropane. **5-TS-R** and **5-TS-S** have a α1 dihedral angle of 135° and −174°, respectively. Thus, the former is calculated to be more stable than the latter by about 3.8 kcal/mol, leading to the preferred formation of the *R* product, as observed experimentally.

In the case of the ferrocene substrate, **6**, we were also able to locate two transition states, as shown in Fig. 4.12. The NMe$_2$ group occupies the upper face of the ferrocene, to avoid steric interactions with the unsubstituted Cp (cyclopentadienyl) group. In the lowest energy transition structure, **6-TS-Sp**, the Fe-Cp moiety is *anti* to the *iPr* of the amino acid. The activated C–H bond orients itself towards the N-protecting group, with α1 dihedral angle of about 141°. In **6-TS-Rp**, the Fe-Cp moiety is *syn* with respect to the *iPr* group. The C–H points upward. Thus, the N-protecting group has to move upward in order to abstract the proton, as indicated by the α1 dihedral angle of about −174°. This results in a destabilization of about 3.9 kcal/mol for the transition state.

4.3.10 Potential Competing Pathways

The above results demonstrate that the internal model (pathway **D**) can effectively relay the chirality from ligand to substrate. For instance, the calculated difference in activation free energy between the formations of *R* and *S* enantiomers is about 4.0 kcal/mol for substrate **1**, corresponding to a high *e.e.* (99.8%). However, the experimental *e.e.* is only about 70%. Our computational results indicate that pathway **B** may compete with pathway **D** in some cases, resulting in partial loss of enantioselectivity. A quantitative evaluation of this competition is rather difficult because the accuracy of the calculations is not sufficient for the small energy differences, but it will be interesting to qualitatively understand the essential loss of enantioselectivity (7% ee) with **L3** for the reaction of substrate **1**. The difference between **L1** and **L3** lies in the N-protecting group. We thus calculated the transition states for the pathways **B** and **D** with **L3**. As shown in Fig. 4.13, the calculated activation free energies for the transition states for pathway **D** leading to the *R* and *S* products are 21.9 and 27.6 kcal/mol, respectively. A very high enantioselectivity would be expected, which is in disagreement with experiment. The calculated
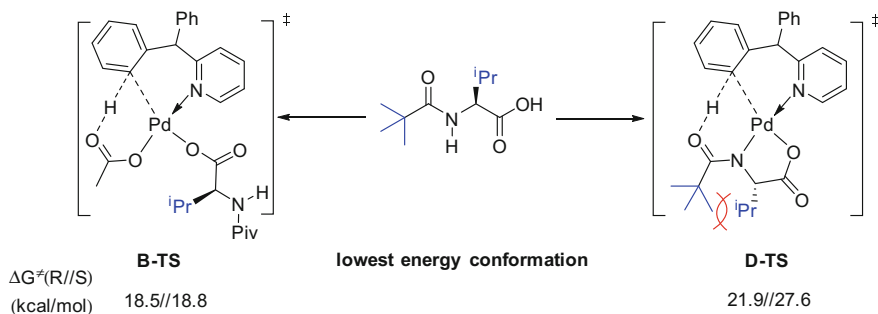

Fig. 4.13 Conformational change for MPAA ligand from the lowest energy conformation to **D-TS** and activation free energies (kcal/mol) for competing pathways **B** and **D** using Piv-Val-OH as ligand
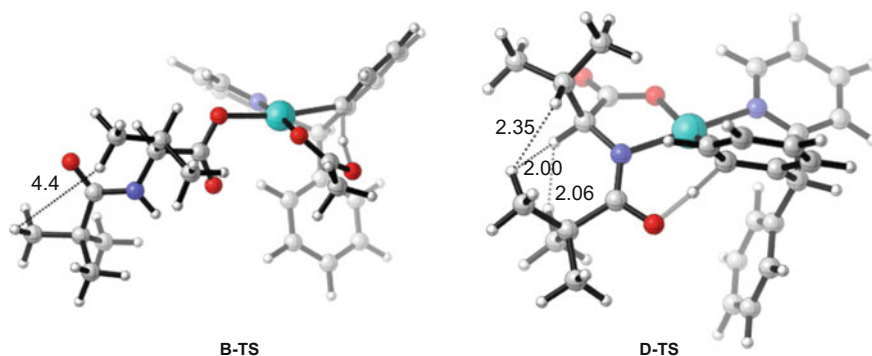
B-TS **D-TS**

Fig. 4.14 Calculated stereoviews of transition states for pathways **B** and **D** using Piv-Val-OH as ligand

activation free energies of the transition states for pathway **B** leading to the *R* and *S* products are 18.5 and 18.8 kcal/mol, respectively. These activation free energies are much lower than those with pathway **D**, indicating that with **L3**, pathway **B** with poor stereoselectivity may be indeed dominant, in agreement with the experimental observation.

As expected, the calculated activation free energies of pathway **B** with **L1** and **L3** are quite similar, as the N-protecting group is away from the reaction center. However, for pathway **D**, the calculated activation free energies with **L3** are over 2.6 kcal/mol higher than those with **L1**. For pathway **D**, the MPAA ligand has to undergo conformational change from the most stable conformation to accommodate the bidentate binding mode (Fig. 4.13). As shown in Fig. 4.14, the bulky tBu group of **L3** suffers from a large steric repulsion in **D-TS**, making pathway **D** less favorable. Therefore, the bulkiness of the N-protecting group can affect the enantioselectivity.

4.4 Summary

In this work, we studied a series of Pd(OAc)$_2$/MPAA catalyzed asymmetric C–H activations by IM-MS and DFT methods. Critical complexes [Pd(MPAA)(**1**), -H]$^+$ and [Pd(MPAA)(**2**), K, -2H]$^+$ have been detected by ESI-MS. With the aid of IM-MS, the complex involving unactivated substrate was separated, and it was found to be deprotonated under further CID experiment, suggesting that the C–H bond of the substrate can be activated without an external base.

In conjunction with DFT calculations, the model postulating the deprotonation by an internal base (pathway **D**) successfully accounts for the enantioselectivity for all studied reactions. In this model, MPAA coordinates with Pd in bidentate fashion and the N-protecting group acts as an internal base in the enantioselectivity-determining step. The enantioselectivity originates from the rigidity of the bidentate MPAA and substrate coordination. The steric repulsion from the amino acid

side-chain positions the N-protecting group below the coordination plane of Pd. As a result, the hydrogen abstraction by the N-protecting group occurs more favorable on the face of Pd coordination plane *anti* to the side-chain of amino acid.

Our computational results also suggest several factors to be considered in further developing Pd/MPAA catalyzed asymmetric reactions: (1) bidentate binding of MPAA, (MPAA with bulky N-protecting group which destabilize the bidentate binding mode such as **L3,** gives poor enantioselectivity); (2) significant bending of the N-protecting group, (the cyclopropane amino acid ligand has two Cα substituents, the bending of the N-protecting group is less significant and consequently results in moderate enantioselectivity); (3) rigid scaffold of substrate for relaying chiral information, (the C–H bond in a flexible group, e.g., freely rotatable sp^3 C–H in methyl group, is more difficult to be well differentiated). Finally, the model here also provides an effective way to rationalize the relay of chirality and could suggest novel approaches for the design of new ligands other than MPAA.

References

1. Stahl SS, Labinger JA, Bercaw JE (1998) Angew Chem Int Ed 37:2180
2. Godula K, Sames D (2006) Science 312:67
3. Bergman RG (2007) Nature 446:391
4. Chen X, Engle KM, Wang D-H, Yu J-Q (2009) Angew Chem Int Ed 48:5094
5. Daugulis O, Do H-Q, Shabashov D (2009) Acc Chem Res 42:1074
6. Lyons TW, Sanford MS (2010) Chem Rev 110:1147
7. Yeung CS, Dong VM (2011) Chem Rev 111:1215
8. Davies HML, Du Bois J, Yu J-Q (2011) Chem Soc Rev 40:1855
9. Engle KM, Mei T-S, Wasa M, Yu J-Q (2011) Acc Chem Res 45:788
10. Colby DA, Tsai AS, Bergman RG, Ellman JA (2011) Acc Chem Res 45:814
11. Doyle MP, Goldberg KI (2012) Acc Chem Res 45:777
12. Neufeldt SR, Sanford MS (2012) Acc Chem Res 45:936
13. Wencel-Delord J, Droge T, Liu F, Glorius F (2011) Chem Soc Rev 40:4740
14. Arockiam PB, Bruneau C, Dixneuf PH (2012) Chem Rev 112:5879
15. Rouquet G, Chatani N (2013) Angew Chem Int Ed 52:11726
16. He J, Li S, Deng Y, Fu H, Laforteza BN, Spangler JE, Homs A, Yu J-Q (2014) Science 343:1216
17. Giri R, Shi B-F, Engle KM, Maugel N, Yu J-Q (2009) Chem Soc Rev 38:3242
18. Zheng C, You S-L (2014) RSC Advances 4:6173
19. Wencel-Delord J, Colobert F (2013) Chem Eur J 19:14010
20. Yang L, Huang H (2012) Catal Sci Technol 2:1099
21. Engle KM, Thuy-Boun PS, Dang M, Yu J-Q (2011) J Am Chem Soc 133:18183
22. Engle KM, Yu J-Q (2013) J Org Chem 78:8927
23. ChanKelvin SL, Wasa M, Chu L, Laforteza BN, Miura M, Yu J-Q (2014) Nat Chem 6:146
24. Shi B-F, Zhang Y-H, Lam JK, Wang D-H, Yu J-Q (2009) J Am Chem Soc 132:460
25. Gao D-W, Shi Y-C, Gu Q, Zhao Z-L, You S-L (2012) J Am Chem Soc 135:86
26. Cheng X-F, Li Y, Su Y-M, Yin F, Wang J-Y, Sheng J, Vora HU, Wang X-S, Yu J-Q (2013) J Am Chem Soc 135:1236
27. Chu L, Wang X-C, Moore CE, Rheingold AL, Yu J-Q (2013) J Am Chem Soc 135:16344
28. Pi C, Li Y, Cui X, Zhang H, Han Y, Wu Y (2013) Chem. Sci. 4:2675
29. Peng HM, Dai L-X, You S-L (2010) Angew Chem Int Ed 49:5826

30. Shi Y-C, Yang R-F, Gao D-W, You S-L (1891) Beilstein J Org Chem 2013:9
31. Xiao K-J, Chu L, Chen G, Yu J-Q (2016) J Am Chem Soc
32. Xiao K-J, Chu L, Yu J-Q (2016) Angew Chem Int Ed 55:2856
33. Du Z-J, Guan J, Wu G-J, Xu P, Gao L-X, Han F-S (2015) J Am Chem Soc 137:632
34. Evans DA, Michael FE, Tedrow JS, Campos KR (2003) J Am Chem Soc 125:3534
35. Shi B-F, Maugel N, Zhang Y-H, Yu J-Q (2008) Angew Chem Int Ed 47:4882
36. Wasa M, Engle KM, Lin DW, Yoo EJ, Yu J-Q (2011) J Am Chem Soc 133:19598
37. Chu L, Xiao K-J, Yu J-Q (2014) Science 346:451
38. Chan KSL, Fu H-Y, Yu J-Q (2015) J Am Chem Soc 137:2042
39. Lapointe D, Fagnou K (2010) Chem Lett 39:1118
40. Biswas B, Sugimoto M, Sakaki S (2000) Organometallics 19:3895
41. Powers DC, Geibel MAL, Klein JEMN, Ritter T (2009) J Am Chem Soc 131:17050
42. Powers DC, Ritter T (2009) Nat Chem 1:302
43. Davies DL, Donald SMA, Macgregor SA (2005) J Am Chem Soc 127:13754
44. Tunge JA, Foresee LN (2005) Organometallics 24:6440
45. Ryabov AD, Sakodinskaya IK, Yatsimirsky AK (1991) J Organomet Chem 406:309
46. Labinger JA, Bercaw JE (2002) Nature 417:507
47. García-Cuadrado D, Braga AAC, Maseras F, Echavarren AM (1066) J Am Chem Soc 2006:128
48. Lafrance M, Fagnou K (2006) J Am Chem Soc 128:16496
49. Baxter RD, Sale D, Engle KM, Yu J-Q, Blackmond DG (2012) J Am Chem Soc 134:4600
50. Musaev DG, Kaledin A, Shi B-F, Yu J-Q (2011) J Am Chem Soc 134:1690
51. After we published the first paper (Ref. 52) about the model in which MPAA acts as base for C–H activation (model D) and during the manuscript preparation of the present work, the Musaeve group applied the same model (model D) to reaction 1 in their review (Chem. Soc. Rev. 2014, 43, 5009)
52. Cheng G-J, Yang Y-F, Liu P, Chen P, Sun T-Y, Li G, Zhang X, Houk KN, Yu J-Q, Wu Y-D (2014) J Am Chem Soc 136:894
53. The present work studied reactions 1–8. Reaction 1.18 and 1.19 in Chapter 1 were not published when this work finished. But the chirality relay model can also be applied to Pd/MPAA catalyzed kinetic resolution reactions 1.18 and 1.19
54. Pringle SD, Giles K, Wildgoose JL, Williams JP, Slade SE, Thalassinos K, Bateman RH, Bowers MT, Scrivens JH (2007) Int J Mass Spectrom 261:1
55. Knapman TW, Valette NM, Warriner SL, Ashcroft AE (2013) Curr Anal Chem 9:181
56. Bush MF, Hall Z, Giles K, Hoyes J, Robinson CV, Ruotolo BT (2010) Anal Chem 82:9557
57. Ruotolo BT, Benesch JLP, Sandercock AM, Hyung S-J, Robinson CV (2008) Nat Protoc 3:1139
58. http://www.indiana.edu/~nano/software.html
59. Wyttenbach T, von Helden G, Batka JJ Jr, Carlat D, Bowers MT (1997) J Am Soc Mass Spectrom 8:275
60. Shvartsburg AA, Jarrold MF (1996) Chem Phys Lett 261:86
61. Shvartsburg AA, Schatz GC, Jarrold MF (1998) J Chem Phys 108:2416
62. Gaussian 09, Revision C.01, Frisch MJ, Trucks GW, Schlegel HB, Scuseria GE, Robb MA, Cheeseman JR, Scalmani G, Barone V, Mennucci B, Petersson GA, Nakatsuji H, Caricato M, Li X, Hratchian HP, Izmaylov AF, Bloino J, Zheng G, Sonnenberg JL, Hada M, Ehara M, Toyota K, Fukuda R, Hasegawa J, Ishida M, Nakajima T, Honda Y, Kitao O, Nakai H, Vreven T, Montgomery JA Jr, Peralta JE, Ogliaro F, Bearpark M, Heyd JJ, Brothers E, Kudin KN, Staroverov VN, Kobayashi R, Normand J, Raghavachari K, Rendell A, Burant JC, Iyengar SS, Tomasi J, Cossi M, Rega N, Millam NJ, Klene M, Knox JE, Cross JB, Bakken V, Adamo C, Jaramillo J, Gomperts R, Stratmann RE, Yazyev O, Austin AJ, Cammi R, Pomelli C, Ochterski JW, Martin RL, Morokuma K, Zakrzewski VG, Voth GA, Salvador P, Dannenberg JJ, Dapprich S, Daniels AD, Farkas Ö, Foresman JB, Ortiz JV, Cioslowski J, Fox DJ (2010) Gaussian, Inc., Wallingford
63. Becke AD (1993) J Chem Phys 98:5648

64. Lee C, Yang W, Parr RG (1988) Phys Rev B 37:785
65. Becke AD (1993) J Chem Phys 98:1372
66. Stephens PJ, Devlin FJ, Chabalowski CF, Frisch MJ (1994) J Phys Chem 98:11623
67. Hay PJ, Wadt WR (1985) J Chem Phys 82:299
68. Roy LE, Hay PJ, Martin RL (2008) J Chem Theory Comput 4:1029
69. Ditchfield R, Hehre WJ, Pople JA (1971) J Chem Phys 54:724
70. Hariharan PC, Pople JA (1973) Theor Chim Acta 28:213
71. Krishnan R, Binkley JS, Seeger R, Pople JA (1980) J Chem Phys 72:650
72. Dolg M, Wedig U, Stoll H, Preuss H (1987) J Chem Phys 86:866
73. Andrae D, Häußermann U, Dolg M, Stoll H, Preuß H (1990) Theor Chim Acta 77:123
74. Zhao Y, Truhlar D (2008) Theor Chem Acc 120:215
75. Marenich AV, Cramer CJ, Truhlar DG (2009) J Phys Chem B 113:6378
76. Legault CY (2009) CYLView, 1.0b. Université de Sherbrooke, Canada. http://www.cylview.org
77. We also used other amino acid ligands in MS study. We decided to present the MS results with N-Ac-Alanine because it is the simplest MPAA ligand without complex side chain and the acetyl group will not be fragmented in CID experiment. Other MPAA ligands may lead to complicated spectra due to the fragmentation of side chain and/or the N-protecting group. The interested reader could refer to the supporting information of ref. 96 for the MS study with N-Boc-Valine ligand
78. Kanu AB, Dwivedi P, Tam M, Matz L, Hill HH (2008) J Mass Spectrom 43:1
79. Harvey SR, MacPhee CE, Barran PE (2011) Methods 54:454
80. Lanucara F, Holman SW, Gray CJ, Eyers CE (2014) Nat Chem 6:281
81. Bohrer BC, Merenbloom SI, Koeniger SL, Hilderbrand AE, Clemmer DE (2008) Annu Rev Anal Chem 1:293
82. Jurneczko E, Barran PE (2011) Analyst 136:20
83. McLean JA, Ruotolo BT, Gillig KJ, Russell DH (2005) Int J Mass Spectrom 240:301
84. Laganowsky A, Reading E, Allison TM, Ulmschneider MB, Degiacomi MT, Baldwin AJ, Robinson CV (2014) Nature 510:172
85. Ducháčková L, Roithová J, Milko P, Žabka J, Tsierkezos N, Schröder D (2010) Inorg Chem 50:771
86. Révész Á, Schröder D, Rokob TA, Havlík M, Dolenský B (2011) Angew Chem Int Ed 50:2401
87. Revesz A, Schroder D, Rokob TA, Havlik M, Dolensky B (2012) Phys Chem Chem Phys 14:6987
88. Schröder D, Buděšínský M, Roithová J (2012) J Am Chem Soc 134:15897
89. Shaffer CJ, Schröder D, Gütz C, Lützen A (2012) Angew Chem Int Ed 51:8097
90. Tsybizova A, Rulíšek L, Schröder D, Rokob TA (2012) J Phys Chem A 117:1171
91. Mesleh MF, Hunter JM, Shvartsburg AA, Schatz GC, Jarrold MF (1996) J Phys Chem 100:16082
92. Theoretical CCSs were calculated employing the open source program, MOBCAL, with trajectory method
93. KOAc was applied in synthesis experiment
94. Evans DA, Campos KR, Tedrow JS, Michael FE, Gagné MR (2000) J Am Chem Soc 122:7905
95. Ess DH, Houk KN (2008) J Am Chem Soc 130:10187
96. Cheng G-J, Chen P, Sun T-Y, Zhang X, Yu J-Q, Wu Y-D (2015) Chem Eur J 21:11180

Chapter 5
Mechanistic Studies on Copper-Catalyzed sp^3-C–H Cross-Dehydrogenative Coupling Reaction

Abstract This chapter introduces a detailed computational study on two Cu-catalyzed sp^3-C–H cross-dehydrogenative coupling (CDC) reactions using O_2 and tert-butyl hydroperoxide (TBHP) as oxidant, respectively. Plausible reaction mechanisms including the single electron transfer (SET) mechanism, a novel mechanism which O_2 directly involves in C–H bond cleavage, Cu^{III} mechanism and radical mechanism were considered. Benchmark studies were performed to select a reliable computational method to describe the SET process.
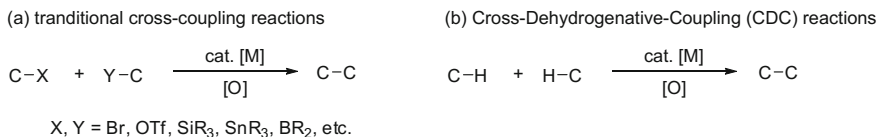
5.1 Introduction

C–C bond formation is central transformation in organic synthesis [1]. Over the past decades, transition metal-catalyzed cross-coupling methods such as Heck [2, 3] reaction, Suzuki [4], Negishi [5], and Stille [6] couplings have been the methods of choice to construct C–C bond. Despite the tremendous success, the requirement of prefunctionalization of substrates limits their applications. Cross-dehydrogenative coupling (CDC) reaction, which couples two C–H bonds directly to form C–C bond [7–13], has emerged as an important protocol to construct C–C bond. Compared to traditional C–C coupling reactions, CDC reaction avoids prefunctionalization which makes synthetic pathway more efficient with less reaction steps and reduces by-products caused by prefunctionalization. During the last decade, CDC reactions have made much progress and various CDC reactions between different types of C–H bonds (sp^3, sp^2 and sp C–H bonds) have been developed [8, 10, 14–17] (Scheme 5.1).

Toward improving CDC reactions, much progress has been made to employ readily available, environmentally friendly oxidant and abundant, sustainable catalysts. In 2007, The Li group reported a copper-catalyzed CDC reaction in water

(a) tranditional cross-coupling reactions   (b) Cross-Dehydrogenative-Coupling (CDC) reactions

$$C-X \ + \ Y-C \ \xrightarrow[\text{[O]}]{\text{cat. [M]}} \ C-C$$

X, Y = Br, OTf, SiR$_3$, SnR$_3$, BR$_2$, etc.

$$C-H \ + \ H-C \ \xrightarrow[\text{[O]}]{\text{cat. [M]}} \ C-C$$

Scheme 5.1 Various cross-coupling methods for C–C bond formation

using O$_2$ as oxidant (Eq. 5.1) [18]. Copper catalysts are cheap, less toxic, and abundant compared to other transition metal catalysts. Oxygen is a sustainable oxidant in green chemistry. This reaction realizes the activation of two sp^3 C–H bonds under mild conditions and produces water as by-product. It serves as an excellent example of green chemistry. On the other hand, its products, tetrahydroisoquinoline derivatives, are important biological active pharmaceuticals which makes this reaction more attractive.

step 1: formation of iminium ion   step 2: nucleophilic addition

(5.1)
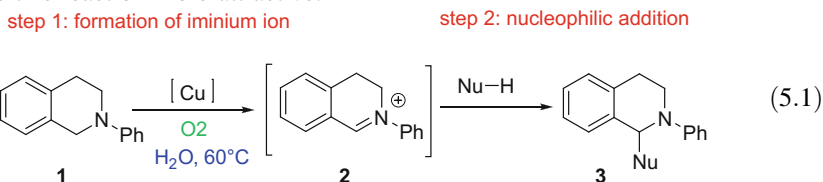
To facilitate further development of this reaction, mechanistic studies have been conducted experimentally. In 2011, Klussmann's group studied a similar reaction and captured the important intermediate—iminium **2** [19], which suggests a reaction sequence that an initial C–H bond activation of tetrahydroisoquinoline to from iminium cation, then nucleophilic addition between iminium cation and nucleophile anion to afford heterocoupling product. It is well known that avoiding homocoupling product is one of the challenges in cross-coupling reactions [20, 21]. Here, for this reaction, the formation of iminium helps to avoid the homocoupling reaction because of charge repulsion which makes this protocol more appealing.

Although the structure of key intermediate **2** has been revealed and this intermediate can successfully explain the selectivity of cross-coupling product, the details of the formation of iminium intermediate remained unknown. This iminium intermediate is usually proposed to be formed via single electron transfer process (SET) [22, 23] since copper can serve as a one-electron oxidant. However, there is no direct experimental evidence to support this hypothesis. On the other hand, the theoretical study for this reaction meets many difficulties which caused by O$_2$ and SET process [24–26]. Reactions of transition metal complexes with O$_2$ often involve state crossing between triplet and singlet states and the calculation of state crossing is still challenging [27–29]. For SET, simulating the dynamic process of SET and calculating the activation energy of SET step are difficult [30, 31].

Moreover, finding an appropriate and reliable method to calculate SET is a hard task because SET process involves radical and ion species with very different electronic structures. To our knowledge, the calculation of SET process is still rare.

In this work, we established a benchmarking to validate a reliable method to calculate SET process. Using this method, we did DFT calculations to investigate the mechanism and gave a detailed picture of the formation of iminium intermediate and subsequent nucleophilic addition. We also explored an alternative pathway for the similar CDC reaction which employs tert-butylhydroperoxide (TBHP) as oxidant.

5.2 Computational Method

All DFT calculations were performed using Gaussian 09 program [32]. Based on the benchmark studies in Sect. 5.3 (vide infra) and good performance of M06 [33] functional in describing cooper system reported in literatures, here we used M06 functional for geometry optimization and energy calculation. The 6-311+G(d, p) basis set was employed for the C, H, N, and O atoms and def2-TZVP [34–37] was used for Cu and Br. SMD [38] model was applied to account for solvent effects. Frequency calculations at the same level of theory were also performed to verify the stationary points as minima (zero imaginary frequencies) or transition states (one imaginary frequency). Transition states were located using the Berny algorithm. Intrinsic reaction coordinates (IRC) were calculated for the transition states to confirm that such structures indeed connect two relevant minima [39]. Reactions of transition metal complexes with O_2 often involve state crossing between triplet and singlet states. We employed an approach developed by Harvey and coworkers to optimize the geometry of minimum energy crossing points (MECP) [40] between potential energy surfaces of different spin states. The relative energies with ZPE corrections and free energies (at 298.15 K) are in kcal/mol. 3D structures are displayed with CYLView [41].

5.3 Results and Discussion

5.3.1 Benchmark Studies

As introduced in Sect. 5.1 (vide supra) it is very important to choose a reliable computational method to describe copper system and single electron transfer process for the studied reaction. Recent theoretical studies have demonstrated that B3LYP [42–44], mPWPW [45–47], and the M06 [48–50] series have good

performance in modeling similar copper systems. But the accurate calculation of SET process which needs to compare the open- and closed-shell configurations of different charge states is still challenging [30, 31]. Based on our long-standing interest in evaluating DFT functionals, we conducted benchmark studies to seek an appropriate method for the system under investigation.

However, there are no systematic data for SET process reported in literature. Considering the one-electron redox involves the electron transfer from donor to acceptor which represents the thermodynamics of SET process, we chose experimental one-electron redox potentials for benchmark studies. Five amines [51, 52] which share some structural similarities with the substrate **1** and have available experimental redox potential values were chosen (Scheme 5.2, complexes **A** to **E**). With this data set, we examined the performance of a series of functionals, including B3LYP, mPWPW, M06, M06L and M06-2X, together with various basis sets by comparing the calculated and experimental redox potential.

The redox potential $E_{calc.}$ (in V) was computed as indicated in Eq. 5.2 [53–57]:

$$E_{calc} = \left(G^{Ox} - G^{Red}\right)/F - 0.03766 - 4.44, \tag{5.2}$$

where G^{Ox} and G^{Red} are the free energies (in Hartree) of the oxidized and reduced systems in solvent, respectively. F is the Faraday constant which equals to 23.06 kcal mol^{-1} V. -0.03766 eV is the energy value of a free electron at 298 K which was calculated by Barmess [58]. -4.44 eV is the free energy change associated with the reference NHE half-reaction (i.e., $H^+(aq) + e^-(g) \rightarrow 1/2 H_2(g)$) [59]. Solvent effects were estimated by SMD model in acetonitrile since most
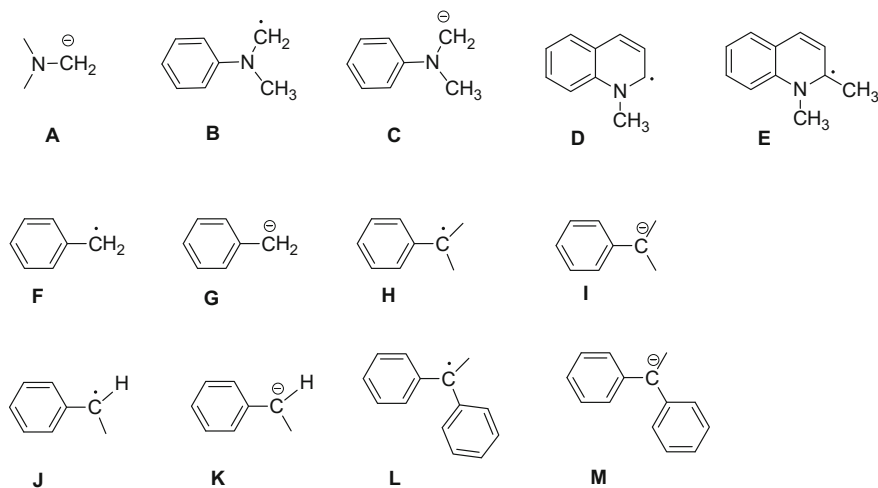
Scheme 5.2 Relevant compounds employed in benchmark studies

Table 5.1 Differences between the experimental standard redox potential and theoretical standard redox potential calculated at different theoretical levels. Reproduced from Ref. [71] by permission of John Wiley & Sons Ltd.

Method	$E_{calc}-E_{exptl}$(V)					
	A	B	C	D	E	Average
B3LYP/6-31g	−1.085	−0.586	−0.789	−0.680	−0.670	−0.762
B3LYP/6-31+g(d)	−0.484	−0.341	−0.318	−0.467	−0.475	−0.417
B3LYP/6-311+g(d, p)	−0.436	−0.306	−0.234	−0.397	−0.412	−0.357
B3LYP/6-311++g(2df, 2p)	−0.464	−0.302	−0.284	−0.423	−0.440	−0.382
mPWPW/6-311+g(d, p)	−0.429	−0.253	−0.252	−0.352	−0.363	−0.330
M06/6-311+g(d, p)	−0.294	−0.235	−0.142	−0.312	−0.326	−0.262
M06L/6-311+g(d, p)	−0.422	−0.318	−0.232	−0.419	−0.443	−0.367
M062X/6-311+g(d, p)	−0.338	−0.331	−0.158	−0.360	−0.376	−0.313

experimental redox values are measured in acetonitrile. The energies of these compounds using different methods were calculated with their optimized geometries.

Table 5.1 lists the values of error of calculated single electron redox potentials (E_{cal}-E_{exptl}). It shows that all methods tested underestimate the single electron redox potentials of the testing data set. The computational results of the first four rows of Table 5.1 which use B3LYP functional but with different basis sets demonstrate that 6-311+G(d, p) has the best performance. In all the functionals tested, M06 gave the smallest average error (−0.262 V). It is worth noting that M06 performed better than M06-2X for this system [33, 60], although the latter was parameterized for main group thermochemistry. According to previous works about redox potential calculation [53], the systematic errors of calculated redox potentials in Table 5.1 could be carefully calibrated.

In order to test the robustness of our method, we extended the tested compounds to another 8 complexes (Scheme 5.2, complexes **F** to **M**) which share less structural similarities with our reactant. The correlation between the experimental and M06/6-311+G(d,p)-calculated standard redox potentials is plotted in Fig. 5.1. The slope and intercept are 1.00 and 0.35 V respectively. The correlation coefficient is 0.99 which shows a strong correlation between the experimental and theoretical standard redox potentials, indicating that this method is reliable to calculate SET processes.

According to the benchmark studies and the performance on describing copper system, M06 was chosen for the following mechanistic studies. 6-311+G(d,p) was used for C, H, N, and O atoms. Correspondingly, the triple-ζ detf2-TZVP basis set was employed for Cu and Br.
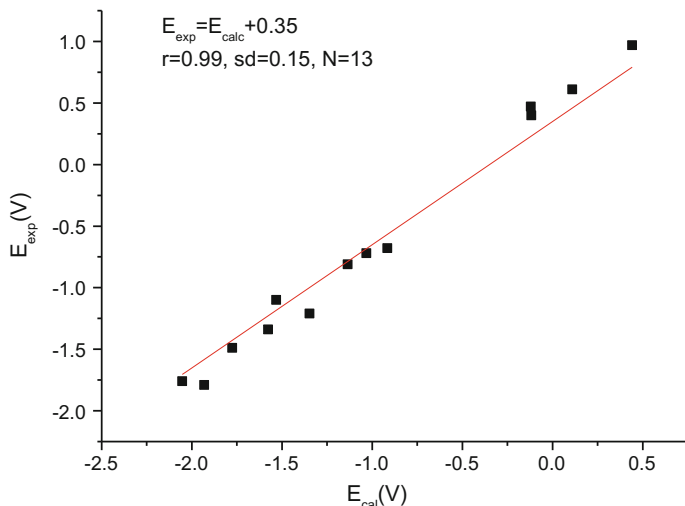
Fig. 5.1 Correlation between the experimental and calculated standard redox potentials

5.3.2   Mechanistic Studies on the Reaction Using Oxygen as Oxidant

5.3.2.1   The Formation of Iminium Intermediate 2

As introduced in Sect. 5.1 (vide supra), Klussmann captured the critical iminium intermediate under a similar reaction condition [19] which suggests a catalytic cycle involving iminium ion. However, details about the formation of this iminium intermediate remained unclear. As depicted in Scheme 5.3, there are several plausible pathways to form iminium ion. In the pathways A–C, CuBr is the active catalyst. In pathway A, the C–H bond is cleavaged by bromide via a σ-bond metathesis manner which is often proposed for transition metal-catalyzed C–H bond activation. In pathway B, Cu abstracts H of the substrate via a three-membered ring TS to afford iminium and copper hydride intermediates. Pathway B can also be considered as oxidative addition of C–H bond to Cu^I center. In pathway C, O$_2$ is directly involved in the C–H activation step: O$_2$ interacts with Cu and abstracts the proton from substrate **1** to generate iminium ion and peroxide complex BrCu^{I}OOH$^-$. The Stahl group has reported the insertion of oxygen to Pd-H bond [61, 62], but reports about oxygen directly activate C–H bond is still rare in literature [63]. In most of the oxygen involved transition metal-catalyzed reactions, oxygen is considered as terminal oxidant to regenerate catalyst. In pathways D and E, Cu^{II} act as the active catalyst. The difference between pathways D and E lies in that the deprotonation takes place at the first SET step (pathway D) or at the second SET step (pathway E).

Figures 5.2 and 5.3 show the potential energy profiles of pathways A-C and the potential energy profiles of pathways D and E, respectively. For pathway A,
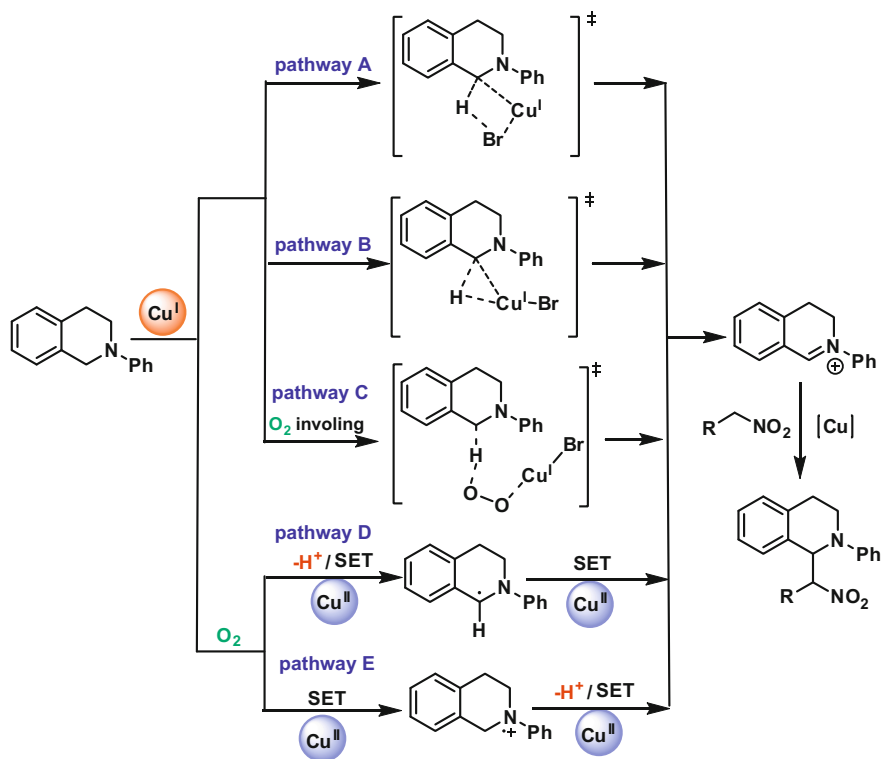
Scheme 5.3 Four proposed pathways for the formation of the iminium intermediate. Reproduced from Ref. [71] by permission of John Wiley & Sons Ltd.

attempts to locate the TS of σ-bond metathesis failed. The optimizations of TS of pathway A always obtain the reactant structure. Then we calculated the intermediate **A1** generated after C–H activation and found **A1** has a very high energy of 47.5 kcal/mol. Therefore, the activation barrier for pathway A should be higher than 56.0 kcal/mol, suggesting that pathway A is not possible under the reported reaction condition. Pathway B has a high activation barrier of 43.4 kcal/mol due to the formation of unstable copper hydride complex which also rules out this mechanism. Pathway C is initiated by the coordination of O_2 with Cu to form triplet intermediate **C2** in which the spin density locates mainly at the O_2. The singlet-state counterpart **C2′** is less stable by 15.2 kcal/mol. Computational result demonstrates that the C–H bond cleavage occurs at the triplet surface. In the transition state structure **TS1-C**, copper adopts a linear bis-coordination ($\angle BrCuO = 170.5°$) revealing the oxidation state of Cu has not changed. The O–O bond in **TS1-C** is elongated to 1.29 Å (O–O bond is 1.20 Å in **C2**), indicating O_2 is reduced to peroxide. Furthermore, the C–H bond of tetrahydroisoquinoline increases to 1.38 Å, demonstrating the oxidation of substrate **1**. The minimum energy crossing point (MECP) between triplet and singlet states was successfully located. It is quite
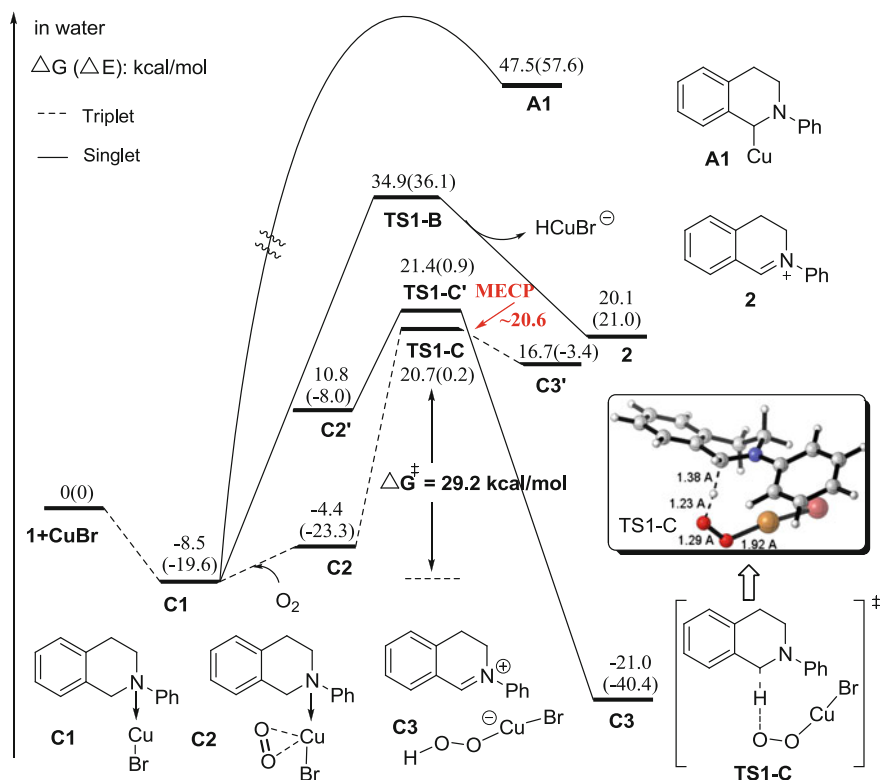
Fig. 5.2 Potential energy profiles of pathways A, B, and C. Free energies and electronic energies are given in kcal/mol. Reproduced from Ref. [71] by permission of John Wiley & Sons Ltd.

close to **TS1-C** in structure and energy. The intermediate **C3** obtained from C–H bond activation is very stable and its free energy is −21.0 kcal/mol. In **C3**, the iminium ion coordinates with Cu via electrostatic interactions, the distance between Cu and N atom is 3.48 Å. The activation barrier for pathway A is 29.2 kcal/mol which could be overcome under the experimental condition.

It is widely accepted that Cu^I can be easily oxidized to Cu^{II} in the present of an oxidant [64–66] which is also the precondition of SET mechanism D and E. Possible Cu^{II} species under the experimental condition include Cu^{II}Br(OH) and CuBr$_2$. Cu^{II}Br(OH) might be precipitate. On the other hand, Cu^{I}X$_2$ (X = Cl or Br) was detected as counterion in the crystal structure of iminium ion **2**. Therefore, Cu^{II}Br$_2$ was used as active catalyst in SET mechanism because it can form Cu^{I}Br$_2$ anion by accepting one electron.

Different from the bis-coordinated, linear Cu^I complex, Cu^{II} complex prefers to adopt four coordination structures. Cu^{II}Br$_2$ binds with two water molecules to
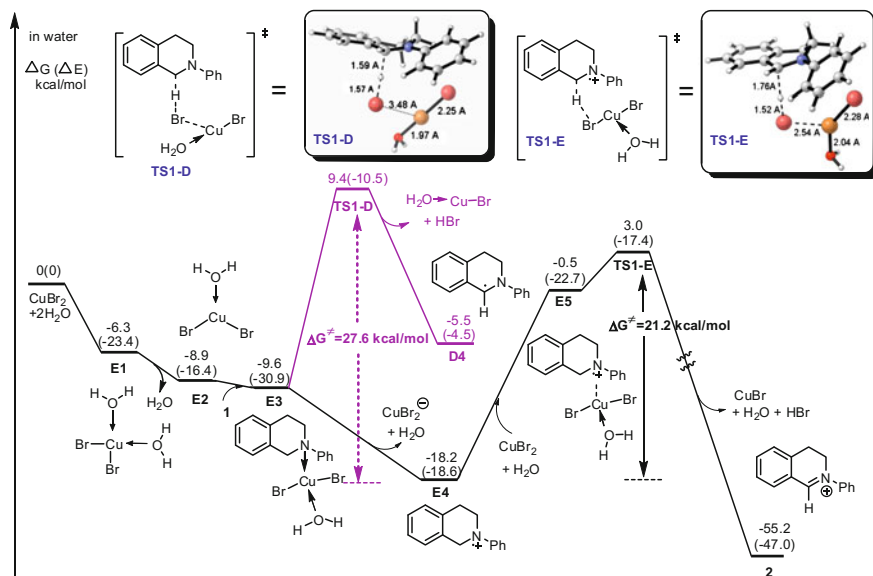
Fig. 5.3 Potential energy profiles of pathways D and E. Free energies and electronic energies are given in kcal/mol. Reproduced from Ref. [71] by permission of John Wiley & Sons Ltd.

afford a four-coordinated complex **E1** which undergoes ligand exchange to form **E3**. **E3** also adopts four-coordinated geometry and the spin density mainly distributed on $CuBr_2$, indicating **E3** remains a Cu^{II} complex. **E3** can either undergo C–H activation (pathway D) to afford intermediate **D4** or undergo single electron transfer (pathway E) to form intermediate **E4**. The computation result shows that **E4** is much more stable than **D4**. For pathway D, the distance between Br and Cu is 3.48 Å in **TS1-D**, indicating Br atom that abstract the proton is likely to be a radical. Thus a considerable activation barrier (27.6 kcal/mol) is expected. The following SET step from **D4** to imiunium **2** is an exothermic process. For pathway E, the single electron transfer of **E3** leads to doublet intermediate **E4** and $Cu^{I}Br_2^-$ ion. This SET step is a facile process thermodynamically and kinetically. Then replacing $Cu^{I}Br_2^-$ with $Cu^{II}Br_2$ affords **E5** which undergoes the second SET. The transition state **TS1-E** can be regarded as a TS of proton-coupled electron transfer. In **TS1-E**, electron transfers to Cu^{II} and in the meanwhile the proton is abstracted by Br^-, leading to iminium intermediate **2** and $Cu^{I}Br$ with a large driving force. The overall barrier for pathway E is 21.2 kcal/mol.

As analysis above, the critical iminium intermediate **2** is possibly formed via pathways C and E. The calculated activation barriers for these two pathways can be overcome under the experimental condition and the calculated KIE values of both pathways are in agreement with KIE experiments (vide infra) [67]. Although a lower barrier for pathway E suggests the reaction may be more possible to proceed via SET mechanism, pathway C cannot be excluded for the following reasons:

(1) the oxidation of Cu^I to Cu^{II} is unclear in pathway E; (2) $Cu^I X_2^-$ (X = Br or Cl) anion was observed in the crystal structure of iminium intermediate, indicating Cu^I can be existed in the present of O_2; (3) the direct comparison between pathways C and E is less accurate because the two pathways proceed at different spin states.

5.3.2.2   The Nucleophilic Addition Step

The reaction process after the formation of iminium intermediate **2** is straightforward: the nucleophile is deprotonated and further reacts with iminium ion **2** via nucleophilic addition to afford product **E9**. The potential energy profile of the reaction of nitromethane and iminium ion **2** is depicted in Fig. 5.4. The computational result shows that the nucleophilic addition step is a faster process than the formation of iminium intermediate **2**, which is in accord with experimental results.

Based on the overall reaction profile, C–H activation is the rate-determining step. The calculated kinetic isotope effect (KIE) k_H/k_D values of **TS1-C** and **TS1-E** are 5.1 and 5.3, respectively, which are comparable to the experimental value (4.5) [67]. In pathway C, O_2 directly involves in the C–H bond activation step and the O-O bond is elongated in **TS1-C**. Pathway E does not include O_2, thus these two pathways could be differentiated by ^{18}O KIE. The calculated ^{18}O KIE value of **TS1-C** is 1.5 [68, 69], while **TS1-E** will not show ^{18}O kinetic isotope effect. Therefore, we expect that the ^{18}O KIE experiment could further verify the mechanism.

Combining all the computational results discussed above, we summarized the catalytic cycle for reaction 1 as depicted in Scheme 5.4. The catalytic cycle is mainly constituted by C–H activation step and nucleophilic addition step. Our theoretical study on the copper-catalyzed aerobic CDC reaction supports that the critical iminium
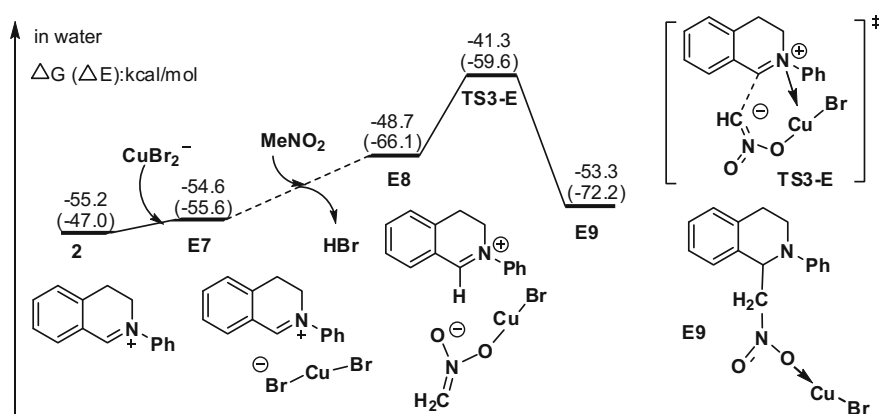

Fig. 5.4 Potential energy profile for the nucleophilic addition step. Free energies and electronic energies are given in kcal/mol. Reproduced from Ref. [71] by permission of John Wiley & Sons Ltd.

Scheme 5.4 Catalytic cycle for the SET mechanism (*black*) and an alternative mechanism in which O_2 is directly involved in the C–H abstraction step (*blue*). Reproduced from Ref. [71] by permission of John Wiley & Sons Ltd.
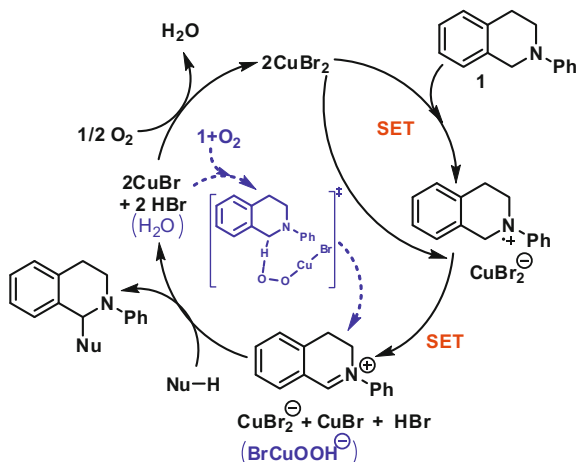

intermediate **2** is formed via SET mechanism but also unveils an alternative mechanism in which O_2 is directly involved in C–H bond cleavage (blue part).

5.3.3 Mechanistic Studies on the CDC Reaction Using TBHP as Oxidant

The CDC reactions of tetrahydroisoquinoline derivatives have been extensively explored with different catalysts, oxidants, and nucleophiles. Klussmann and coworkers reported a CDC reaction of substrate **1** using tert-butyl hydroperoxide (TBHP) as oxidant [67]. They found that different from the reaction employing O_2 as oxidant, an amino peroxide **3a** instead of imunium ion was detected (Eq. 5.3). Klussmann and coworkers ruled out the SET mechanism (pathways D and E in Scheme 5.3) by comparing the relative nucleophilicity of TBHP with other nucleophilic reactants. Instead, they proposed a radical mechanism (Scheme 5.5) according to further detailed kinetic studies.

$$(5.3)$$
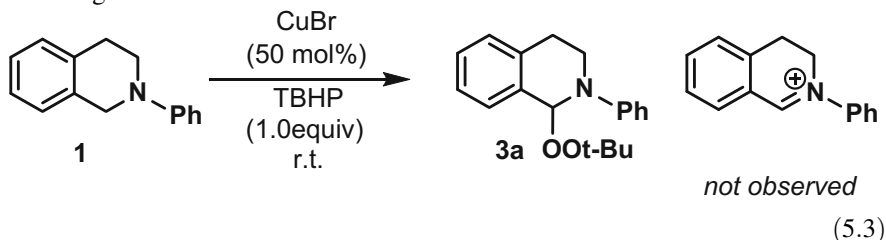
Scheme 5.5 Catalytic cycle of the radical mechanism for Cu/TBHP-catalyzed CDC reaction. Reproduced from Ref. [71] by permission of John Wiley & Sons Ltd.
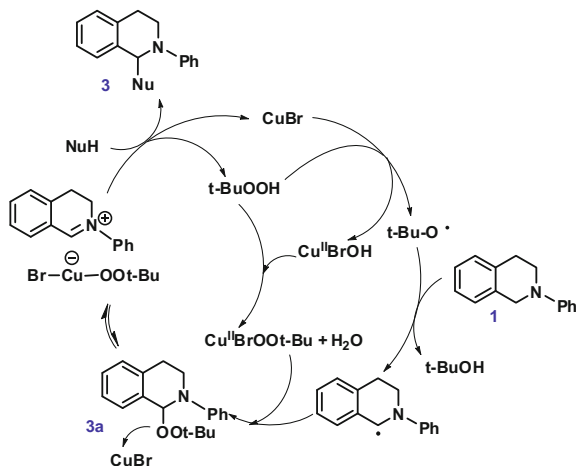
Given that the existing contradiction of the radical inhibition reactions between Li's and Klussmann's groups and the observation that radical inhibitor cannot completely suppress the reaction in Klussmann's experiment, also concerning about radical reactions may generate homo-coupled side products which is not reported in this cross-coupling reaction, thus we carried out computational study to explore the possibility of alternative pathways for the CDC reaction when using TBHP as oxidant. It also serves as a comparative study for the previous reaction with O_2 as oxidant to investigate whether different oxidant leads to different reaction mechanisms. Because the radical mechanism was proposed based on a critical experimental observation of **3a** as an intermediate, therefore we focused on the formation of **3a**.

The energy profile of the radical mechanism is depicted in Fig. 5.5. The radical pathway F starts with the oxidation of Cu^{I}Br by tBuOOH to form Cu^{II}Br(OH) and tBuO· radical. Cu^{II}Br(OH) reacts with a second molecule of TBHP via a four-membered ring **TS1-F** to afford Cu^{II}Br(OOtBu) and water. In the following step, the tBuO· radical abstracts a hydrogen atom from substrate **1** to generate a radical **F6**. The activation barrier for this step is 22.7 kcal/mol. Then the radical **F6** reacts with the doublet compound **F5** formed during the previous process to produce complex **3a** and Cu^{I}Br. Based on the overall profile, the hydrogen abstracting step is the rate-determining step for radical pathway. The calculated KIE value of radical pathway F is 1.45, which is much smaller than the experimental KIE value (3.4). This theoretical KIE value of **TS1-F** is close to the calculated KIE value
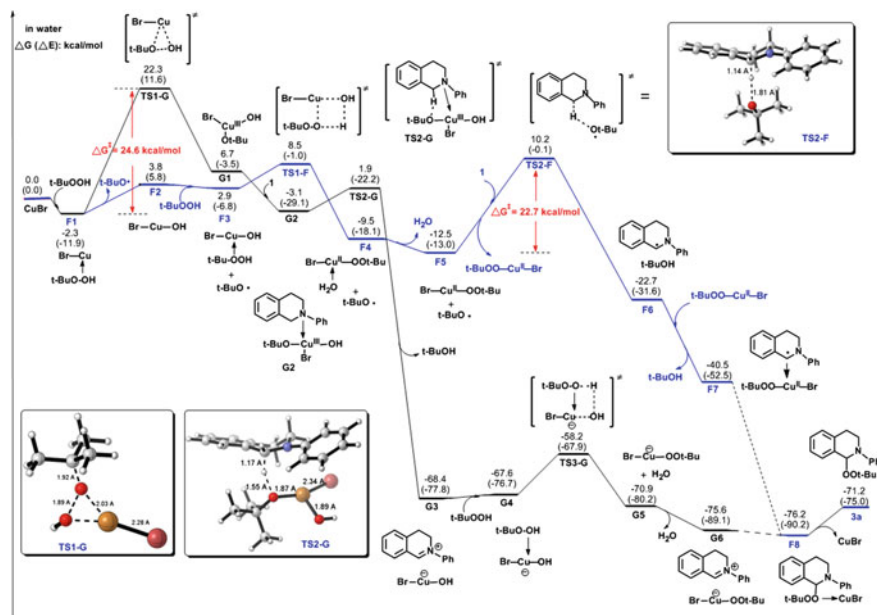
Fig. 5.5 Potential energy profiles of pathways F (radical pathway) and G (Cu^{III} pathway). Free energies and electronic energies are given in kcal/mol. Reproduced from Ref. [71] by permission of John Wiley & Sons Ltd.

(1.79) for the CuBr catalyzed oxidation reaction of *N,N*-dimethylaniline by T-HYDRO.

Aside from the radical pathway, we also considered an alternative mechanism which involves a Cu^{I}/Cu^{III} catalytic cycle. The Himo group reported that the barrier for the reaction of Cu^{I}Br and TBHP to form high-valent complex Cu^{III}Br(OtBu)$_2$ is 16.9 kcal/mol [70] which can be easily overcome under the experimental condition under investigation. As shown in Fig. 5.5, the Cu^{III} pathway G starts with the oxidative addition reaction of BrCu^{I}(TBHP) (**F1**) to form Cu^{III}Br(O^{t}Bu)(OH) (**G1**). The activation free energy for the first step was calculated to be 24.6 kcal/mol. Substrate **1** coordinates with intermediate **G1** leading to a four-coordinated Cu^{III} complex (**G2**). Then tBuO ligand abstracts the hydrogen of the substrate, in the meanwhile the electron transfer to the copper center, generating imiunium intermediate **G3**. This process takes place with a low barrier and a large driving force due to the instability of high-valent Cu^{III} species **G2**. The following nucleophilic addition by another molecule of TBHP affords the observed intermediate **3a**. But for the Cu^{III} mechanism, the oxidative addition step is the rate-determining step, which is not consistent with the KIE experiment.

Because TBHP can oxidize Cu^{I} to Cu^{II}, thus SET mechanism is also possible for the Cu/TBHP system. As shown in Fig. 5.3 and 5.5, the SET pathway has a comparable activation barrier with Cu^{III} mechanism. In summary, computational

results for the Cu-catalyzed CDC reaction with TBHP as oxidant demonstrate that the radical pathway is more favorable. But Cu^{III} and SET mechanism cannot be excluded completely. The experimental KIE value (3.4) is between the KIE value of pathway E (5.11) and the KIE value of pathway F (1.49), suggesting both pathways are possible for this Cu/TBHP system.

5.4   Summary

In this chapter, we studied the Cu-catalyzed sp^3 C–H cross-dehydrogenative coupling reactions with O$_2$ and TBHP as oxidant. In order to choose an appropriate computational method to describe the Cu system and SET process, a benchmark study was performed. The single electron redox potentials were employed for calibration since it reflects the thermodynamic properties of single electron transfer process. Our computational results as well as the data in literature suggest that M06/6-311+(d,p) is an appropriate method for calculating the system under investigation since it is reliable for calculating the SET process and it has good performance in describing Cu system.

Applying this method, we did the first computational study on the Cu-catalyzed aerobic CDC reaction of tetrahydroisoquinoline derivative. The computational results suggest this reaction is likely to take place via a single electron transfer mechanism in which the critical iminium intermediate **2** is formed from a radical cation compound **E4** rather than a radical species **D4**. Besides the SET mechanism, our study unveils another alternative reaction mechanism (pathway C) in which O$_2$ is directly involved in the C–H bond cleavage step. For the overall reaction process, the C–H bond activation step is the rate-determining step while the subsequent electrophilic addition step is a faster step. For both pathways C and E, C–H activation is the rate-determining step and the calculated KIE values are 5.05 and 5.11, respectively, which are comparable to the experimental value (4.5). Considering the different roles of O$_2$ in pathway C and E, we predicted that ^{18}O KIE may be able to differentiate these two mechanisms.

As a comparative study, we also investigate the similar CDC reaction with TBHP as oxidant. Different from the reaction with O$_2$ as oxidant, an amino peroxide instead of iminium ion was observed for the reaction employing TBHP as oxidant. For this reaction, the radical pathway, Cu^{III} pathway and SET pathway were found to have comparable activation free energies. Cu^{III} mechanism can be ruled out because the oxidative addition is calculated to be the rate-determining step which contradicts with experimental observations. For both radical pathway and SET pathway, the C–H activation step is the rate-determining step which is consistent with experiments. The KIE experiments and computational results cannot exclude either of these pathways at this point.

References

1. (a) Hartley FR (ed) (1985) S.P. carbon–carbon bond formation using organometallic compounds, vol 3. Marcel Dekker, New York. (b) Corey EJ, Cheng XM (eds) (1989) The logic of chemical synthesis. Wiley, New York
2. Heck RF (1979) Acc Chem Res 12:146
3. Dieck HA, Heck FR (1975) J Organomet Chem 93:259
4. Miyaura N, Suzuki A (1995) Chem Rev 95:2457
5. King AO, Okukado N, Negishi E-I (1977) J Chem Soc Chem Commun 683
6. Milstein D, Stille JK (1978) J Am Chem Soc 100:3636
7. Scheuermann CJ (2010) Chem Asian J 5:436
8. Li Z, Li C-J (2005) J Am Chem Soc 127:3672
9. Li C-J (2008) Acc Chem Res 42:335
10. Li Z, Bohle DS, Li C-J (2006) Proc Natl Acad Sci 103:8928
11. Yeung CS, Dong VM (2011) Chem Rev 111:1215
12. Shi W, Liu C, Lei A (2011) Chem Soc Rev 40:2761
13. Cho SH, Kim JY, Kwak J, Chang S (2011) Chem Soc Rev 40:5068
14. Wei C, Li C-J (2002) Green Chem 4:39
15. Li Z, Li C-J (2005) J Am Chem Soc 127:6968
16. Li C-J, Wei C (2012) *Chem Commun* 268
17. Koradin C, Polborn K, Knochel P (2002) Angew Chem Int Ed 41:2535
18. Basle O, Li C-J (2007) Green Chem 9:1047
19. Boess E, Sureshkumar D, Sud A, Wirtz C, Fares C, Klussmann M (2011) J Am Chem Soc 133:8106
20. Ashenhurst JA (2010) Chem Soc Rev 39:540
21. Negishi E-I, Hata M, Xu C (2000) Org Lett 2:3687
22. Zhang C, Tang C, Jiao N (2012) Chem Soc Rev 41:3464
23. Wendlandt AE, Suess AM, Stahl SS (2011) Angew Chem Int Ed 50:11062
24. Huber SM, Moughal Shahi AR, Aquilante F, Cramer CJ, Gagliardi L (2009) J Chem Theory Comput 5:2967
25. Schröder D, Fiedler A, Herrmann WA, Schwarz H (1995) Angew Chem Int Ed Engl 34:2517
26. Poli R, Harvey JN (2003) Chem Soc Rev 32:1
27. Landis CR, Morales CM, Stahl SS (2004) J Am Chem Soc 126:16302
28. Wang R, Zhang X-H, Chen S-J, Yu X, Wang C-S, Beach DB, Wu Y-D, Xue Z-L (2005) J Am Chem Soc 127:5204
29. Keith JM, Nielsen RJ, Oxgaard J, Goddard WA (2005) J Am Chem Soc 127:13172
30. Jones GO, Liu P, Houk KN, Buchwald SL (2010) J Am Chem Soc 132:6205
31. Yu H-Z, Jiang Y-Y, Fu Y, Liu L (2010) J Am Chem Soc 132:18078
32. Gaussian 09, Revision A.2, Frisch MJ, Trucks GW, Schlegel HB, Scuseria GE, Robb MA, Cheeseman JR, Scalmani G, Barone V, Mennucci B, Petersson GA, Nakatsuji H, Caricato M, Li X, Hratchian HP, Izmaylov AF, Bloino J, Zheng G, Sonnenberg JL, Hada M, Ehara M, Toyota K, Fukuda R, Hasegawa J, Ishida M, Nakajima T, Honda Y, Kitao O, Nakai H, Vreven T, Montgomery JA Jr, Peralta JE, Ogliaro F, Bearpark M, Heyd JJ, Brothers E, Kudin KN, Staroverov VN, Kobayashi R, Normand J, Raghavachari K, Rendell A, Burant JC, Iyengar SS, Tomasi J, Cossi M, Rega N, Millam NJ, Klene M, Knox JE, Cross JB, Bakken V, Adamo C, Jaramillo J, Gomperts R, Stratmann RE, Yazyev O, Austin AJ, Cammi R, Pomelli C, Ochterski JW, Martin RL, Morokuma K, Zakrzewski VG, Voth GA, Salvador P, Dannenberg JJ, Dapprich S, Daniels AD, Farkas Ö, Foresman JB, Ortiz JV, Cioslowski J, Fox DJ (2009) Gaussian, Inc., Wallingford
33. Zhao Y, Truhlar D (2008) Theor Chem Acc 120:215
34. Zhang X, Schwarz H (2011) Theor Chem Acc 129:389
35. Zhang X, Schwarz H (2010) Chem Eur J 16:5882
36. Weigend F, Ahlrichs R (2005) Phys Chem Chem Phys 7:3297

37. Schäfer A, Huber C, Ahlrichs R (1994) J Chem Phys 100:5829
38. Marenich AV, Cramer CJ, Truhlar DG (2009) J Phys Chem B 113:6378
39. Fukui K (1970) J Phys Chem 74:4161
40. Harvey JN, Aschi M, Schwarz H, Koch W (1998) Theor Chem Acc 99:95
41. Legault CY (2009) CYLView, 1.0b. Université de Sherbrooke, Canada. http://www.cylview.org
42. Gherman B, Heppner D, Tolman W, Cramer C (2006) J Biol Inorg Chem 11:197
43. Aboelella NW, Gherman BF, Hill LMR, York JT, Holm N, Young VG, Cramer CJ, Tolman WB (2006) J Am Chem Soc 128:3445
44. Gherman BF, Tolman WB, Cramer CJ (2006) J Comput Chem 27:1950
45. Kunishita A, Scanlon JD, Ishimaru H, Honda K, Ogura T, Suzuki M, Cramer CJ, Itoh S (2008) Inorg Chem 47:8222
46. Cramer CJ, Truhlar DG (2009) Phys Chem Chem Phys 11:10757
47. Lanci MP, Smirnov VV, Cramer CJ, Gauchenova EV, Sundermeyer J, Roth JP (2007) J Am Chem Soc 129:14697
48. Hong S, Huber SM, Gagliardi L, Cramer CC, Tolman WB (2007) J Am Chem Soc 129:14190
49. Bar-Nahum I, Gupta AK, Huber SM, Ertem MZ, Cramer CJ, Tolman WB (2009) J Am Chem Soc 131:2812
50. Cramer CJ, Gour JR, Kinal A, Wloch M, Piecuch P, Moughal Shahi AR, Gagliardi L (2008) J Phys Chem A 112:3754
51. Fukuzumi S, Kitano T (1991) J Chem Soc Perkin Trans 2:41
52. Wayner DDM, McPhee DJ, Griller D (1988) J Am Chem Soc 110:132
53. Fu Y, Liu L, Yu H-Z, Wang Y-M, Guo Q-X (2005) J Am Chem Soc 127:7227
54. Davis AP, Fry AJ (2010) J Phys Chem A 114:12299
55. Credendino R, Falivene L, Cavallo L (2012) J Am Chem Soc 134:8127
56. Baik M-H, Friesner RA (2002) J Phys Chem A 106:7407
57. Speelman AL, Gillmore JG (2008) J Phys Chem A 112:5684
58. Bartmess JE (1994) J Phys Chem 98:6420
59. Trasatti S (1986) Pure Appl Chem 58:955
60. Zhao Y, Truhlar DG (2008) Acc Chem Res 41:157
61. Popp BV, Wendlandt JE, Landis CR, Stahl SS (2007) Angew Chem Int Ed 46:601
62. Popp BV, Stahl SS (2007) J Am Chem Soc 129:4410
63. Ranjit S, Lee R, Heryadi D, Shen C, Wu JE, Zhang P, Huang K-W, Liu X (2011) J Org Chem 76:8999
64. Randles JEB (1941) J Chem Soc 802
65. Matyjaszewski K, Tsarevsky NV, Braunecker WA, Dong H, Huang J, Jakubowski W, Kwak Y, Nicolay R, Tang W, Yoon JA (2007) Macromolecules 40:7795
66. Fenwick F (1926) J Am Chem Soc 48:860
67. Boess E, Schmitz C, Klussmann M (2012) J Am Chem Soc 134:5317
68. Smirnov VV, Roth JP (2006) J Am Chem Soc 128:16424
69. Roth JP (2007) Curr Opin Chem Biol 11:142
70. Santoro S, Liao R-Z, Himo F (2011) J Org Chem 76:9246
71. Cheng G-J, Song L-J, Yang Y-F, Zhang X, Wiest O, Wu Y-D (2013) ChemPlusChem 78:943